Chapter 1 Introduction

1.1 Carbon nanomaterials

Carbon is the most versatile element in the periodic table in terms of the type, strength, and number of bonds it can form with many different elements. The diversity of bonds and their corresponding geometries enable the existence of structural isomers, which are found in distinct, large, and complex structures, and an endless variety of molecular geometries. Carbon atoms form both sigma (σ) and pi (π) bonds in molecular structures, the final geometries of which depend on the levels of hybridization of the carbon atoms' orbitals. The number and nature of these bonds determine the geometries and properties of the carbon allotropes: graphite, diamond, and fullerenes (Figure 1.1 [1]; Table 1.1 [2]). Graphite comprises layered planar sheets of sp^2-hybridized carbon atoms bonded together in a hexagonal network. Each carbon atom in a graphite sheet is bonded to only three other atoms; the nonbonded electrons can move freely from one unhybridized p orbital to another, giving rise to graphite's characteristic soft, slippery, and electrically conductive properties. In contrast, diamond has a crystalline structure in which each sp^3-hybridized carbon atom is bonded to four others in a tetrahedral arrangement. This crystalline network gives diamond its properties of hardness and excellent heat conduction. Fullerenes comprise a family of spheroidal and cylindrical molecules in which all of the carbon atoms are sp^2 hybridized. The parallel and tubular forms of the fullerenes are discussed in the next Sections with a detailed description of their history and properties.

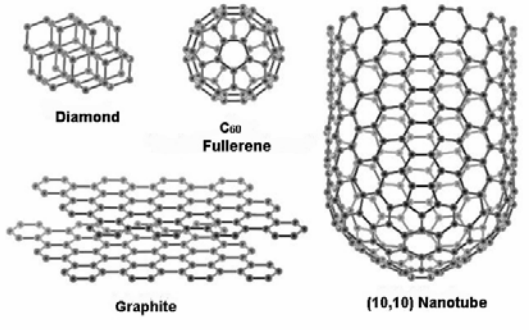

Figure 1.1 Examples of the three allotropes of carbon [1].

Table 1.1 Isomers of carbon [2]

Dimension	0-D	1-D	2-D	3-D
Isomer	C_{60} Fullerene	CNTs Carbyne	Graphite Fiber	Diamond Amorphous
Hybridization	sp^2	sp^2 (sp)	sp^2	sp^3
Density [g/cm^3]	1.72	1.2–2.0 2.68–3.13	2.26 ca. 2	3.515 2–3
Bond length [Å]	1.4 (C=C) 1.46 (C–C)	1.44 (C=C)	1.42 (C=C) 1.44 (C=C)	1.54 (C–C)
Electronic Properties	Semiconductor E_g = 1.9 eV	Metal or Semiconductor	Semimetal	Insulator E_g = 5.47 eV

1.1.1 Carbon nanotubes (CNTs)

In 1990, Rick Smalley proposed the existence of a tubular fullerene [3]. He envisioned a so-called “bucky tube” that could be prepared by elongating a molecule of C_{60}. Experimental evidence for the existence of CNTs came in 1991 when Iijima imaged multiwalled carbon nanotubes (MWCNTs) using transmission electron microscopy (TEM) [4]. Two years after

the first observation of MWCNTs, Iijima and coworkers observed single-walled carbon nanotubes (SWCNTs).

1.1.1.1 Structures and properties of CNTs

Iijima was the first to realize that CNTs were concentrically rolled graphene sheets featuring a large number of potential chiralities, rather than single graphene sheets rolled up like a scroll. He initially observed only MWCNTs with between 2 and 20 layers. Two years later, he confirmed the existence of SWCNTs and annotated their structures [5].

1.1.1.1.1 Structures of CNTs

In the ideal case, a CNT consists of either one cylindrical graphene sheet (i.e., an SWCNT) or several nested cylinders having an interlayer spacing of 0.34–0.36 nm, close to the typical spacing of turbostratic graphite (i.e., an MWCNT). There are many possible ways of forming a cylinder from a graphene sheet [6]; a few such configurations are presented in Figure 1.2. Figures 1.2(a)–(c) display SWCNTs having (a) zigzag, (b) armchair, and (c) chiral types of structures. Figure 1.2(d) represents an MWCNT formed by four tubes of increasing diameter with a layer spacing of 0.34 nm. The sheet can be rolled up along one of the symmetry axis, giving either a zigzag tube or an armchair tube. It is also possible to roll up the sheet in a direction other than a symmetry axis to obtain a chiral CNT. In addition to the chiral angle, the circumference of the cylinder can also be varied.

Figure 1.3 displays the cutting of a graphite sheet along the dotted lines that connect two crystalline graphite-equivalent sites on a 2-D surface [8]. Each carbon atom has three nearest neighbors; rolling the sheet of graphite into a cylinder forms the CNTs, the circumference of which can be expressed in terms of the chiral vector C_h and the chiral angle θ. The chiral vector is given by Eq. (1.1):

$$C_h = na_1 + ma_2 \equiv (n,m) \tag{1.1}$$

(*n* and *m* are integers; 0 ≦ |m| ≦ n)

where a_1 and a_2 are the primitive vector lengths, both of which are equal to $\sqrt{3}\ l_{C\text{–}C,}$ with $l_{C\text{–}C}$ is the length of C–C bond. The chiral angle determines the degree of twisting in the tube; it has two limiting values: 0 and 30°. The chiral angle is defined using Eq. (1.2):

$$\cos\theta = \frac{C_h \cdot a_1}{|C_h| \cdot |a_1|} = \frac{2n+m}{2\sqrt{nm+m^2+n^2}} \tag{1.2}$$

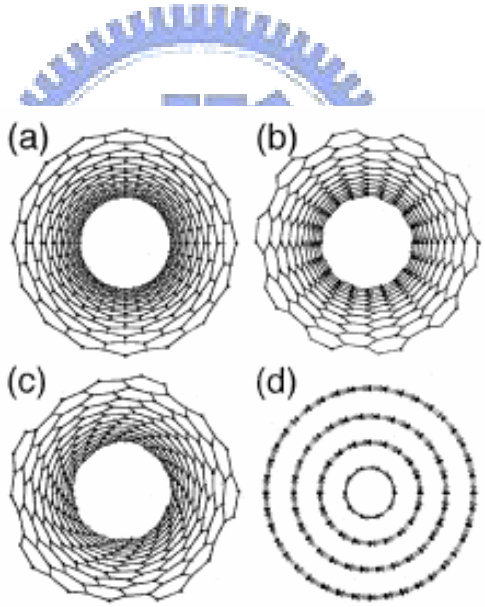

Figure 1.2. Molecular models of various CNT structures [7].

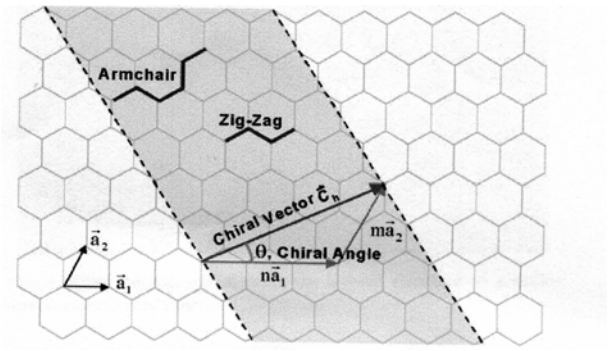

Figure 1.3 Schematic representation of how a hexagonal sheet of graphite can be rolled up to form a CNT [8].

The zigzag and armchair CNTs correspond to the cases where $m = 0$ and $n = m$, respectively. The chiral CNT corresponds to all other (n, m) chiral vectors. The zigzag CNT (n, 0) is generated from the hexagon with $\theta = 0°$; the armchair CNT (n, n) is formed from the hexagon with $\theta = 30°$; the chiral CNT is formed from the hexagon with $0° < \theta < 30°$.

Because the inter-atomic spacing of carbon atoms is known, the rolled up vector of a CNT can define the CNT diameter. The properties of CNTs depend on their atomic arrangement, diameter, length, and morphology [9].

A diversity of possible configurations is found in practice, with no particular type being formed preferentially. In most cases, the layers of MWCNTs are chiral [4, 10] and have different helicities [11]. The lengths of SWCNTs and MWCNTs are usually well over 1 μm; their diameters range from ca. 1 nm (for SWCNTs) to ca. 50 nm (for MWCNTs). Pristine SWCNTs are usually closed at both ends by fullerene-like half-spheres that contain both pentagons and hexagons [e.g., Figure 1.4(a)] [6]. An MWCNT where the shape of the cap is more polyhedral than spherical is presented in Figure 1.4(b). An open MWCNT, where the ends of the graphene layers and the internal cavity of the tube are exposed, is displayed in Figure 1.4(c). Defects in the hexagonal lattice are usually present in the form of pentagons and heptagons. Pentagons produce a positive curvature of the graphene layer and are mostly

found at the cap, as indicated in Figure 1.4(b) where each knick in the graphene layer points to the presence of a pentagon in the carbon network. Heptagons give rise to a negative curvature of the tube wall [12]. Defects consisting of several pentagons and/or heptagons have also been observed. A simple model confirms that the diameter and/or chirality of a tube are changed from one side of the defect to the other [13]. Such an arrangement that forms a link between two different tubes is, accordingly, called a "junction."

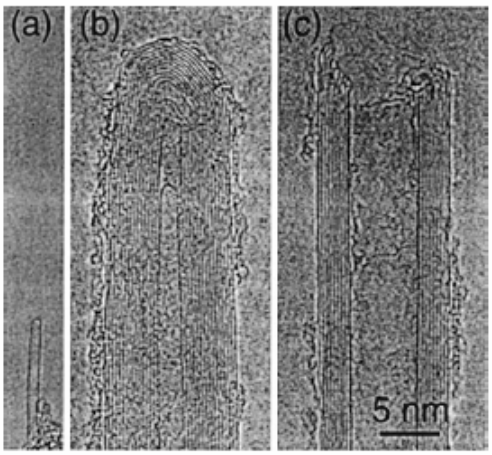

Figure 1.4 TEM images of the ends of (a) an SWCNT, (b) a closed MWCNT, and (c) an open MWCNT. Each black line corresponds to one graphene sheet viewed edge-on [7].

1.1.1.1.2 Electronic properties of CNTs

The electronic properties of SWCNTs have been investigated in a large number of theoretical studies [6, 14–17]. These models reveal that the electronic properties vary in a calculable way, from metallic to semiconducting, depending on the tube's chirality (n, m) [18]:

Metallic properties: $n - m = 0$ or $(n - m)/3 =$ integer

Semiconducting properties: $(n - m)/3 \neq$ integer

As a result, approximately one third of all SWCNTs are metallic, while the others are semiconducting with a band gap inversely proportional to the tube diameter. This behavior is due to the very unusual band structure of graphene; it is absent in systems that can be described with usual free electron theory. Graphene is a zero-gap semiconductor having energy bands of the p-electrons crossing the Fermi level at the edges of the Brillouin zone, leading to a Fermi surface comprising six points [19]. Graphene should exhibit metallic behavior at room temperature because its electrons readily cross from the valence band to the conduction band. It behaves, however, as a semi-metal because the electronic density at the Fermi level is quite low [18, 19]. Rolling up the graphene sheet into a cylinder imposes periodic boundary conditions along the circumference; only a limited number of wave vectors are allowed in the direction perpendicular to the tube axis. When such wave vectors cross the edge of the Brillouin zone—and, thus, the Fermi surface—the CNT is metallic, as is the case for all armchair tubes and for one third of the zigzag and chiral tubes. Otherwise, the band structure of the CNT exhibits a gap, leading to semiconducting behavior, with a band gap that scales approximately with the inverse of the tube's radius. Band gaps of 0.4–1 eV can be expected for SWCNTs (corresponding to diameters of 1.6–0.6 nm) [6, 14, 16]. This simple model does not take into account the curvature of the tube, which induces hybridization effects for very small tubes [15] and generates a small band gap for most metallic tubes [17]. The exceptions are armchair tubes, which remain metallic due to their high symmetry.

These theoretical predictions made in 1992 were confirmed experimentally in 1998 using scanning tunneling spectroscopy [20, 21]. Scanning tunneling microscopy (STM) has since then been used to image the atomic structures of SWCNTs [22, 23], the electron wave function [24], and to characterize the band structure [23, 25]. Many conductivity experiments on SWCNTs and MWCNTs have yielded additional information [26–37]. At low temperatures, SWCNTs behave as coherent quantum wires, where the conduction occurs through discrete electron states over large distances. Transport measurements revealed that

metallic SWCNTs possess extremely long coherence lengths [30, 37, 38]. MWCNTs also exhibit these effects, despite their larger diameters and multiple shells [39, 40].

1.1.1.1.3 Mechanical properties of CNTs

A growing body of experimental evidence confirms that MWCNTs and SWCNTs have extraordinary mechanical properties. Yakobson et al. [41, 42] inspected the instability of CNTs beyond their linear response. Their simulations revealed that CNTs are remarkably resilient, sustaining extreme strain with no signs of brittleness or plasticity. Some experimental measurements of the Young's moduli of CNTs have been reported. Treacy et al. [43] determined the relationship between the amplitude of the tip oscillations and the Young's modulus. Through TEM observations of some CNTs, they defined the amplitude of those oscillations and obtained an average value of 1.8 TPa for the Young's modulus. Another way to probe the mechanical properties of CNTs is to use the tip of an atomic force microscope to bend an anchored CNT. The Young's modulus can be extracted while simultaneously recording the force exerted by the tube as a function of the displacement from its equilibrium position. Using this approach, Wong et al. [44] reported a mean value of 1.28 ± 0.59 TPa for MWCNTs, with no dependence on the tube diameter. Walters et al. [45] investigated the elastic strain of CNT bundles using AFM. Assuming an experimental strain measurement and an elastic modulus of 1.25 TPa, they calculated a yield strength of 45 ± 7 GPa.

Yu et al. [46, 47] investigated the tensile properties of SWCNT and MWCNT ropes. For MWCNT ropes, the tensile strengths of the outermost layer ranged from 11 to 63 GPa and the elastic modulus ranged from 27 to 950 GPa. For SWCNT ropes, the tensile strengths were in the range 13–52 GPa and the average elastic modulus was 320–1470 GPa.

In term of their mechanical properties, CNTs are among the strongest and most elastic materials known to exist in Nature [48]. Table 1.2 compares the mechanical properties of CNTs with those of other materials. In general, MWCNTs exhibit superior mechanical

characteristics. The hollow structures and closed topologies of CNTs provide a distinct mechanical response relative to that of other graphitic structures.

Table 1.2 Mechanical properties of CNTs and other materials [48]

Material	Young's modulus (GPa)	Tensile strength (GPa)	Density (g/cm^3)
SWCNT	1054	ca. 150	
MWCNT	1200	ca. 150	2.6
(10,10) Nano-rope	563	ca. 75	1.3
Type I carbon fiber	350	2.5	2.6
Steel	208	0.4	7.8
Epoxy	3.5	0.05	1.25
Wood	16	0.08	0.6

1.1.2 Carbon nanowalls (CNWs)

The petal-like graphitic nanowalls were first reported by Ebbesen and Ajayan in 1992 as the byproduct of the synthesis of CNTs [49]. Several groups have since used graphitic nanowalls as field emitters [50, 51]. Graphitic nanowalls can also serve as catalyst supports or hydrogen absorption agents because of their large surface-to-volume ratios.

1.1.2.1 Structures and properties of CNWs

Self-assembled carbon nanostructures, such as CNTs [52, 53] and nanofibers [54], have attracted much attention for their use in several applications, such as gas storage, as membranes for electrochemical energy storage, and field emitters [55–58]. On the other hand, 2-D carbon nanostructures have also been grown. Ando et al. [59] found carbon nanoflakes were also formed when fabricating CNTs through arc discharge. Recently, Wu et al. [60] reported the fabrication, using microwave plasma-enhanced chemical vapor deposition

(MPCVD), of 2-D carbon nanostructures, i.e., CNWs, standing vertically on the catalyzed substrates. The large surface areas of carbon nanoflakes and CNWs may make them useful in various applications.

1.1.2.1.1 Structures of CNWs

Plasma-enhanced chemical vapor deposition is one of the most reliable techniques for synthesizing CNWs. Figure 1.5 provides a schematic representation of CNWs synthesized on a substrate. Carbon structures can be grown into well-aligned 2-D sheets on a substrate by manipulating the electrical conduction from the catalyst to the bias electrode in a MPCVD system. The existence of a strong lateral electric field between the catalyst islands is the key factor promoting the growth of nanowalls instead of CNTs. The localized field, which is induced by metallic particles via excitation of surface plasmons, significantly alters the growth of CNWs in terms of both the surface morphology and density. If the surface plasmon can be excited in a well-controlled manner, it may become a viable tool for growing very dense CNWs for potential industrial applications.

The thickness of the sheets varies from one to seven graphene layers, with termination edges of one–three graphene layers [62]. A schematic representation of an individual sheet is presented in Figure 1.6. The high energy plasma necessary to grow the ultrathin sheets is also likely to generate a significant defect density, as well as the adsorption or incorporation many hydrogen atoms.

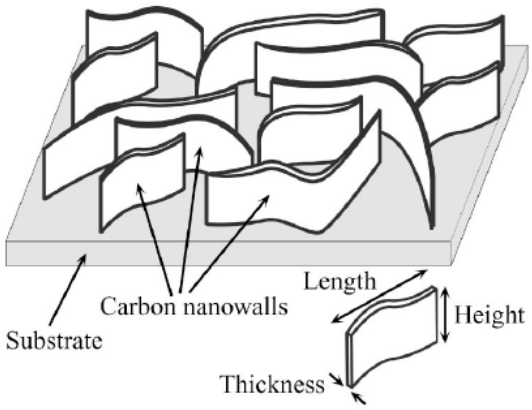

Figure 1.5 Schematic representation of CNWs synthesized vertically on a substrate [61].

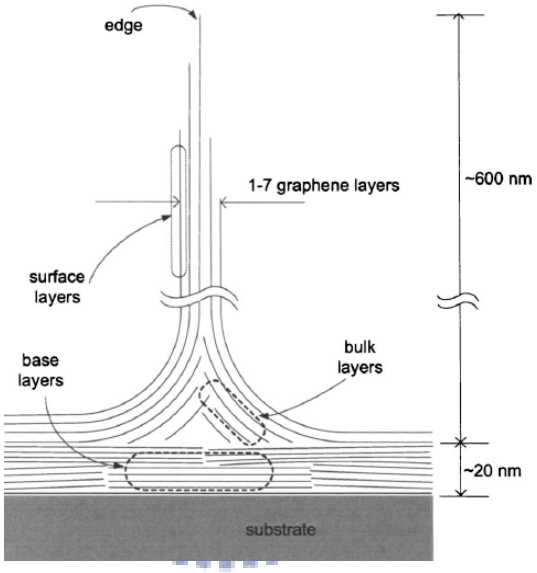

Figure 1.6 Schematic representation of a CNW [63].

1.1.2.1.2 Properties of CNWs

Because they are new carbon allotropes and nanoscaled materials, CNW films, which consist of petal-like graphite walls having a thickness of ca. 20 nm or less, are of much interest [64]. Wu et al. have described the formation mechanisms and classification of 2-D carbon nanomaterials [65]. CNWs and CNTs possess similar electronic characteristics because of their crystalline structures and identical spacing between graphene layers. Even though they always appear in a vertical manner, the large surface-to-volume ratio of CNWs gives rise to their remarkable field emission characteristics and their ability to function as

supports for catalysts in energy storage applications. The resistance of CNWs decreases upon decreasing the temperature and, in general, increases upon increasing the magnetic field [65]. Despite possessing graphitic structures analogous to those of CNTs, further studies of 2-D CNWs will be necessary to identify their other properties.

1.1.3 Application of carbon nanomaterials

1.1.3.1 Energy storage

Graphite carbonaceous materials and carbon fiber electrodes are commonly used in fuel cells, batteries, and other electrochemical applications. The potential advantages of CNTs and CNWs for energy storage are their small dimensions, smooth surface topologies, and perfect surface specificities. The efficiency of fuel cells is determined by the electron transfer rate at the carbon electrodes; it is fastest on graphene planes, which follow ideal Nernstian behavior [66].

1.1.3.2 Supercapacitors

Supercapacitors possess high capacitance and are potentially applicable in electronic devices. In electrochemical devices, they typically comprise two electrodes separated by an insulating material that is ionically conducting (electric double-layer capacitor). The capacity of a supercapacitor is inversely dependent on the separation between the charge on the electrode and the counter charge in the electrolyte. As a result, a large amount of charge adsorption may occur when only a small voltage is applied. This charge adsorption is used for energy storage in carbonaceous supercapacitors [67]. In general, most attempts have been made to prepare redox supercapacitors.

1.1.3.3 Hydrogen storage

The advantage of using H_2 as an energy source is that water is the only combustion product. Additionally, H_2 is readily regenerated. For this reason, a suitable H_2 storage system is necessary to satisfy both volume and weight limitations. Two common ways to store H_2 are gas phase and electrochemical adsorption. Because of their cylindrical and hollow geometries and nanometer-scale diameters, it has been predicted that CNTs can be used to store liquids or gases in their inner cores through capillary effects. The minimum threshold for economical storage of H_2 is 6.5% by weight for H_2 fuel cells. SWCNTs can meet—and sometimes exceed—this level when using gas phase adsorption (physisorption). Nevertheless, most experimental reports of high-storage capacities are rather controversial, making it difficult to assess their potential applicability. We lack a detailed understanding of the H_2 storage mechanism and the effect of material processing on this mechanism. Another possibility for H_2 storage is electrochemical storage. In this case, hydrogen atoms are adsorbed, rather than H_2 molecules—so-called "chemisorption."

1.1.3.4 Lithium intercalation

The basic principle of rechargeable Li batteries is the electrochemical intercalation and de-intercalation of Li in both electrodes. An ideal battery requires a high energy capacity, fast charging, and high durability. The capacity is determined by the Li saturation concentration of the electrode materials. For Li ions, this capacity is highest in CNTs if all of the interstitial sites (inner-shell van der Waals spaces, inter-tube channels, and inner cores) are accessible for Li intercalation. SWCNTs can possess both highly reversible and irreversible capacities. Because of a large voltage hysteresis, Li intercalation in CNTs remains unsuitable for battery applications. This behavior can potentially be reduced or eliminated through processing, i.e., cutting the CNTs into short segments.

1.1.3.5 Field emission devices

If a solid is subjected to a sufficiently high electric field, electrons near the Fermi level can be extracted from the solid by tunneling through the surface potential barrier. This emission current depends on the strength of the local electric field at the emission surface and its work function, i.e., the energy necessary to extract an electron from its highest bounded state into the volume level. The applied electric field must be very high in order to extract an electron. This condition is fulfilled for CNTs because their elongated shapes ensure very large field amplifications.

For technological applications, the emissive material should have a low threshold emission field and high stability at high current densities. Moreover, an ideal emitter must have a diameter on the nanometer scale, structural integrity, high electrical conductivity, a small energy spread, and high chemical stability. Although CNTs and CNWs possess all of these properties, a bottleneck hindering their application is the dependence of the conductivity and emission stability on the fabrication processes and synthesis conditions. Examples of potential applications of CNTs as field emitting devices are in flat panel displays, gas discharge tubes in telecom networks, electron guns for electron microscopes, AFM tips, and microwave amplifiers.

1.1.3.6 Composite materials [66]

Because of their stiffness, CNTs are ideal materials for structural applications. For example, they may be used as reinforcement composites of high strength, low weight, and high performance. Theoretically, SWCNTs have a Young's modulus of 1 TPa. MWCNTs are weaker because the individual cylinders slide with respect to one another. Ropes of SWCNTs are also less strong because individual tubes can be pulled out by shearing and, ultimately, the whole rope breaks—at stresses far below the tensile strength of an individual CNT. CNTs also sustain large strains in tension without fracture. In other directions, CNTs are highly

flexible. One of the most important applications of CNTs is the reinforcement of composite materials, but there have too few successful experiments to confirm their superior filler performance over traditional carbon fibers. The main problem is to create a good interface between the CNTs and the polymer matrix, because CNTs are too smooth and have diameters that are nearly identical to those of the polymer chains. Next, the mechanical properties of sets of CNTs are quite different from those of their individual CNTs because of their ready aggregation. Limiting factors for good load transfer are the sliding of cylinders in MWCNTs and the shearing of tubes in SWCNTs ropes. To solve these problems, the aggregates must be broken up and dispersed or cross-linked to prevent slippage. A main advantage of using CNTs in structural polymer composites is that CNT reinforcements increase the toughness of the composites by absorbing energy, due to their high elasticity. Other advantages of CNTs are their low density, increased electrical conduction, and high performance during compressive loading. Another non-structural application of CNTs is the filling of photoactive polymers. Poly-*p*-phenylenevinylene (PPV) polymers filled with MWCNTs and SWCNTs are composites that have been used in several experiments. These composites display large increases in conductivity with only small losses in their photoluminescence and electroluminescence yields. Another benefit is that the composites are more robust than the pure polymers. CNT/polymer composites might also find use in other areas—for example, as membranes for biomolecular separations or osteointegration (growth of bone cells)—but these areas are less explored. The most important thing we must understand about CNTs—if they are to be used as efficient reinforcing fibers—is how to manipulate their surfaces chemically to enhance the interfacial behavior between individual CNTs and the matrix.

1.1.3.7 **Transistors** [67, 68]

A field-effect transistor—a three-terminal switching device—can be constructed using only a single semiconducting SWCNT. By applying a voltage to a gate electrode, CNTs can

be switched from conducting to insulating states. Figure 1.7 presents a schematic representation of such a transistor. Series of CNT transistors can be put to work as logical switches, the basic components of computers [68].

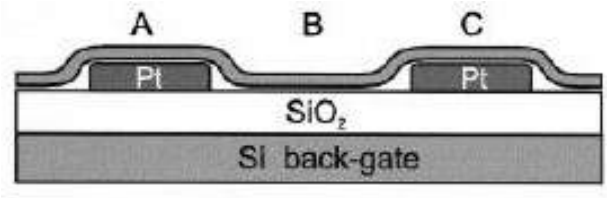

Figure 1.7 A field effect transistor formed from a single semiconducting CNT in contact with two electrodes. The Si substrate, which is covered by a 300-nm-thick layer of SiO_2, acts as a back-gate.

1.1.3.8 **Templates** [66]

Because of their small channels, strong capillary forces exist in CNTs. These forces are strong enough to hold gases and fluids within the CNTs and it is possible to fill the cavities in CNTs to build nanowires. The critical issue is the CNT's wetting characteristics. Because of their smaller pore sizes, filling SWCNTs is more difficult than filling MWCNTs. If it becomes possible to keep fluids within CNTs, it may also be possible to run chemical reactions within their cavities. Although some organic solvents can wet CNTs readily, making nanoreactors available in theory, the ends of most CNTs are normally closed. They can be opened, however, through a simple chemical reaction: oxidation. Because the pentagons in the end cap of CNTs are more reactive toward oxidation than are the hexagons of the sidewalls, the caps are readily removed while the sidewalls remain intact.

1.1.3.9 **Nanoprobes and sensors** [66, 67]

Because of their flexibility, CNTs can also be used in scanning probe instruments. The tips of MWCNTs are conducting; therefore, they can be used in STM and AFM instruments

(Figure 1.8). The advantages of using this approach are improved resolution (relative to conventional Si or metal tips) and tips that do not suffer from crashes with the surfaces because of their high elasticity. Nevertheless, CNT vibration, due to their length, will remain an important issue until shorter CNTs can be grown controllably.

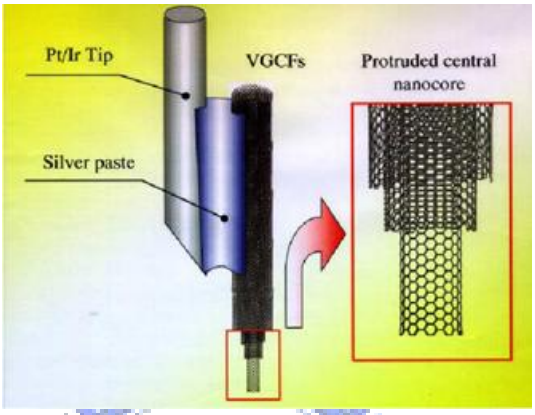

Figure 1.8 Using an MWCNT as an AFM tip. The MWNT at the center of the vapor-grown carbon fiber (VGCF) forms the tip.

CNT tips can be modified chemically through attachment of functional groups. As a result, CNTs can be used as molecular probes, with potential applications in many aspects of chemistry and biology. A pair of CNTs can be used as a pair of tweezers to move nanoscale structures on surfaces. Sheets of SWCNTs can be used as electromechanical actuators, mimicking the actuator mechanism present in natural muscles. SWCNTs may also be used as miniaturized chemical sensors because their electrical resistance changes on exposure to environments containing NO_2, NH_3, or O_2.

1.1.4 Carbon nanomaterial synthesis

Three major methods have been developed for the synthesis of CNTs: arc discharging, laser ablation, and catalytic chemical vapor deposition.

1.1.4.1 Arc discharging

Arc discharging was the first method developed for the production of MWCNTs [69] and SWCNTs [70, 71]. To this day, this classic method still produces the best quality MWCNT samples. Because arc discharging was in use for a many years for the production of carbon fibers, it is very possible that CNTs were observed, but not recognized, prior to Iijima's first synthesis of CNTs in 1991 [72, 73].

Figure 1.9 presents a schematic representation of an arc discharge system and a TEM micrograph of a grown CNT [2]. The arc discharge apparatus features graphite rods as the anode and cathode. These rods are brought together under a gas atmosphere (usually He, but H_2 [74] and Ar have also been used) and a voltage is applied until a stable arc is achieved. As the anode is consumed, the gap (ca. 1 mm) between the cathode and anode is maintained by adjusting the position of the anode. Carbon materials are deposited on the cathode to form CNTs and other carbon particles. MWCNTs produced by arc discharging are long and straight tubes that are closed at both ends with graphitic walls running parallel to the tube axis, as indicated in Figure 1.9.

Several factors are critical to producing good yields of high-quality CNTs. Harris [75] reported that perhaps the most important is the He pressure in the chamber, as demonstrated by Ebbesen and Ajayan [69]. The current in the arc discharge method is another important factor [76, 77]. Efficient cooling of the electrodes and the chambers is essential to producing good-quality CNT samples [76–78].

To synthesize SWCNTs, Iijima et al. [70] and Bethune et al. [71] reported in 1993 that an arc discharge system featuring a cathode containing metal catalysts (such as Co, Fe, or Ni) mixed with graphite powder results in a deposit containing SWCNTs. Since then, the yield has been increased significantly by optimizing the catalyst mixture [79] and the deposition conditions [80].

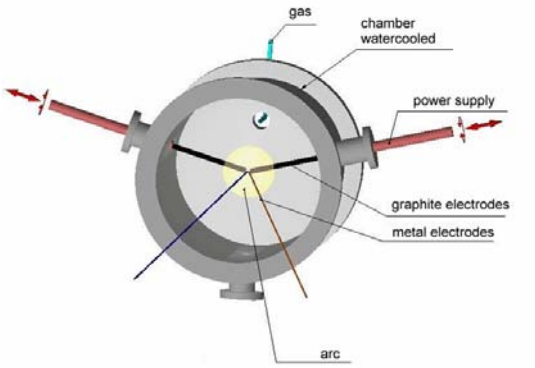

Figure 1.9 Schematic representation of an arc discharge system [7].

1.1.4.2 Laser ablation

Laser ablation was first used for the synthesis of C_{60} in 1985 by Kroto et al. [81]; in 1995, it was demonstrated for the growth of SWCNTs and MWCNTs by Smalley's group at Rice University [82]. Subsequent refinements to this method led to the production of SWCNTs with unusually uniform diameter [83]. The lengths of the MWCNTs grown using this method are, however, much shorter than those obtained through arc discharging [82].

Thess et al. [83] reported that the synthesis could be performed in a horizontal flow tube under a flow of inert gas at controlled pressure. In this setup, the flow tube is heated to ca. 1200 °C by a tube furnace, as displayed in Figure 1.10. Laser pulses enter the tube and strike a target consisting of a mixture of graphite and a metal catalyst (e.g., Co or Ni). SWCNTs condense from the laser vaporization plume and are deposited on a collector located outside the furnace zone [84]. The size of the carbon source limits the volume of sample produced and purification steps are necessary to separate the CNTs from undesired by-products. Nevertheless, this method remains an important technique for synthesizing SWCNTs in high yield.

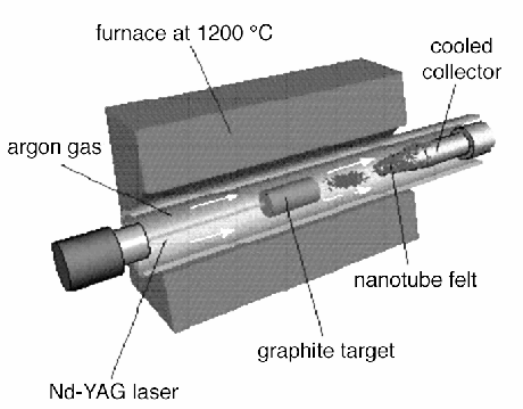

Figure 1.10 Schematic representation of the laser ablation apparatus [85].

1.1.4.3 Catalyst chemical vapor deposition

The catalytic growth of CNTs is an alternative to the arc discharge and laser ablation methods. It involves the decomposition of a hydrocarbon gas over a transition metal to grow CNTs through chemical vapor deposition (CVD). Since the 1960s [86], carbon filaments and fibers have been produced through the thermal decomposition of hydrocarbons. Usually, a catalyst is necessary to promote this growth [87]. A similar approach was used in 1993 to grow MWCNTs through the decomposition of acetylene over Fe particles [88]. Figure 1.11 displays a CNT produced through catalytic growth. In general, the diameters of CNTs grown through catalytic growth are larger than those obtained through arc discharging, but they are formed with imperfectly graphitized crystalline structures. To grow MWCNTs, acetylene is usually used as the carbon source at temperatures typically between 600 and 800 °C. To grow SWCNTs, the temperature must be significantly higher (900–1200 °C) because of their higher energy of formation. In this case CO or CH_4 must be used because they exhibit increased stability, relative to that of acetylene, at higher temperatures.

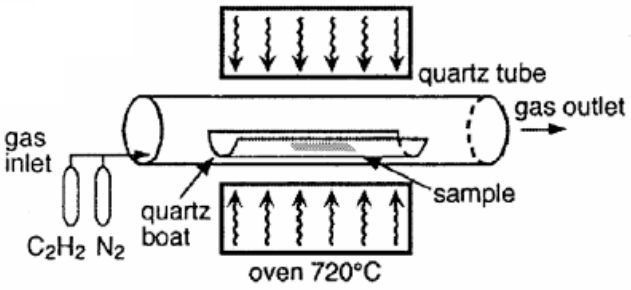

Figure 1.11 Schematic representation of the apparatus used for catalytic deposition [7].

Since its development, catalytic CVD has undergone many improvements. Cobalt catalysts supported on Si particles produce straight as well as coiled MWCNTs [89]; the yields of CNTs are increased significantly when using zeolites as catalyst supports [90, 91]. The continuous production of SWCNTs, where both the carbon atoms and the catalyst are supplied in the gas phase, has also been reported. The yield and average diameter of the SWCNTs can be varied by controlling the process parameters [92]. In addition, the nature of the catalyst support controls the formation of individual or bundled SWCNTs [93]. Transition metal particles (e.g., Fe, Co, Ni) are suitable catalysts for the synthesis of vapor-grown CNTs in which hydrocarbons are used as carbon atom sources. Metal catalysts are generally necessary to activate CNT growth. Many other catalysts, hydrocarbons, and catalyst supports have been used successfully to synthesize CNTs [94, 95]. Table 1.3 lists the various metal compounds that have been used as catalysts [96]

Catalytic CVD is also an ideal method for growing CNTs on planar substrates (e.g., silicon or glass). Dense MWCNT arrays have been deposited on mesoporous Si that had been prepared using a sol–gel process [97]; long, aligned CNTs have been obtained over several square millimeters by using large-area mesoporous Si substrates [98]. Aligned MWCNTs have been generated through pyrolysis of a triazine compound at 950 °C with nearly no by-products [99]. There are two main reasons why the development of catalytic techniques for growing CNTs on planar substrates is attractive. First, in many cases, purification steps are

unnecessary because there are no or very few by-products. Second, the substrates can be patterned directly with catalysts using lithographic techniques and then subjected to catalytic growth.

CNTs have also been deposited through the plasma-assisted CVD (PACVD) of CH_4 and H_2 at 950 °C [100]; the synthesis temperature was decreased to below 660 °C when using plasma-enhanced hot filament CVD [101]. Since these developments, several papers have described the synthesis of films of CNTs on Si substrates [102–105]. Moreover, MPCVD of CH_4 and H_2 has allowed the deposition temperature to be lowered further, to below 600 °C, on Ni-coated Si [106], Ni [107], steel, and Ni-coated glass [108] substrates. The synthesis of well-aligned CNTs on a variety of substrates can be accomplished through the use of PACVD when the plasma is excited by a DC source [109] or a microwave source [110–112]. These approaches have been used to grow straight CNTs over large areas with uniformity in length, diameter, density, and straightness [97].

The CVD technique uses a gas phase system in which CNTs are formed through the deposition of a carbon-containing gas [97]. Gas phase techniques are amenable to continuous processing because the carbon source is replaced continuously by the flowing gas. In addition, the final purity of these CNTs can be sufficiently high to minimize the number of purification steps. The advantage of the CVD technique is that CNTs can be synthesized continuously and, therefore, the growth of pure CNTs can be performed under optimal conditions. It is a very good way of synthesizing large quantities of CNTs under relatively controlled conditions. Therefore, CVD has its advantages for use in the scale-up and commercial production of CNTs.

Table 1.3 Metals and metal compounds used as catalysts for SWCNT synthesis [96]

Metal/compound	Experimental conditions[1]	Location of SWCNT[2]	Density of SWCNT[3]
Fe	Fullerence	Soot	High
		Extended deposition	High
	Tube	Soot	Low
Ni	Fullerence	Soot	High
		Extended deposition	High
	Tube	Soot	Low
Co	Fullerence	Soot	Low
	Tube	Soot	High
		Weblike	High
Fe/Ni	Fullerence	Soot	Very high
	Tube	Soot	Very high
		Weblike	Very high
Fe/Co	Fullerence	Soot	Low
	Tube	Soot	High
		Weblike	Very high
Ni/Co	Fullerence	Soot	Very high
	Tube	Soot	Very high
		Weblike	Very high
Ni/Cu	Tube	Soot	Low
Ni/Ti	Tube	Soot	Very low
Cu/Co	Tube	Soot	Low
Mg/Ni	Tube	Soot	Low
Y_2O_3/Co	Tube	Soot	Low, radial
YC_2	Tube	Soot	High, radial

[1] "Fullerence" for arc discharge at 100-torr He; "Tube" at 550 torr.

[2] "Soot" and "Extended deposit" protruding from the usual cathodic deposit, and "Weblike deposit."

[3] Categorized as "very high," "high," "low," and "very low."

1.1.4.4 Catalytic growth mechanisms of CNTs

Because of the huge number of compounds and the various bonding modes of carbon atoms, there are many methods available for growing carbon-related nanomaterials. Each method has its advantages, disadvantages, distinguishing feature, and range for suitable use. Most of them have been used successfully to synthesize CNTs.

The model used to describe the growth of nanomaterials remains an issue because of the difficulty in observing growth on such extremely small scales. Even though, several mechanisms have been developed to characterize the behavior for the growth processes. Here, we discuss some of the models that are considered to be the major mechanisms behind the growth of nanosize material.

The mechanisms of the various kinds of bottom-up growth of nanosize materials generally fall into three categories: the vapor–solid (VS) model, the vapor–liquid–solid (VLS) model, and, more recently, the solution–liquid–solid (SLS) model. Some modifications [113] have also been published, but they are not discussed here.

VS model

Figure 1.12 depicts an approximate growth model of the VS growth mechanism. The diagram takes the growth of GaN as an example. Epitaxial growth can be achieved without using a catalyst or a liquid phase. The sum of the thermodynamic surface energy and the heat of fusion is the driving force for VS growth. The growth rate in the VS model is dominated by the rates of diffusion and rearrangement of the atoms and molecules. The VS mechanism has a lower growth rate than the corresponding growth performed using a catalyst.

VLS model

The VLS mechanism [114] was first introduced in the 1960s to explain the growth of Si whiskers and tubular structures [115]. In this model, growth occurs through precipitation from

a supersaturated liquid/metal alloy droplet located at the top of a whisker, into which Si atoms are preferentially absorbed from the vapor phase. The similarity between the growth of CNTs and the VLS model has been noted by Saito et al. [116, 117] on the basis of their experimental findings for MWCNT growth in a purely carbon environment (Figure 1.13). Because solid carbon sublimates before it melts at ambient pressure, they suggested that some other disordered carbon form with high fluidity, possibly induced by ion irradiation, should be used to replace the liquid droplet.

SLS model

Figure 1.14 [118] depicts the SLS growth mechanism, taking Ⅲ-Ⅴ materials as an example. No catalyst is used for solution-phase synthesis. The materials are produced as polycrystalline fibers or near-single-crystal whiskers having widths of 10–150 nm and lengths of up to several micrometers [119]. The mechanism of this growth process is analogous to VLS growth at low temperatures; the requirement that the catalyst melts below the solvent boiling point is a potential limitation.

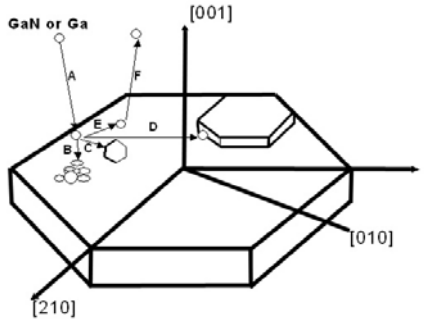

Figure 1.12 Schematic representation of the VS growth model.

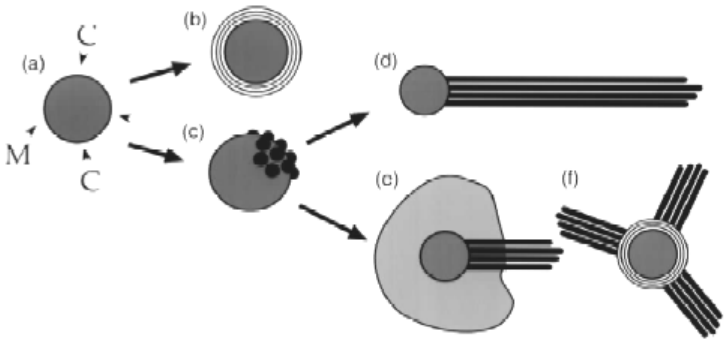

Figure 1.13 Schematic representation of the VLS growth mechanism for CNTs.

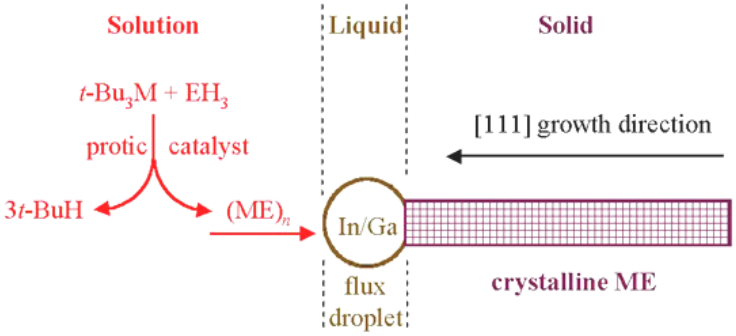

Figure 1.14 Schematic representation of the SLS growth mechanism.

1.2 Electrochemical capacitors [120]

Electrochemical capacitors (ECs), variously referred to by their manufacturers in promotional literature as “supercapacitors” or “ultracapacitors,” store electrical charge in an electric double layer at the interface between a high-surface-area carbon electrode and a liquid electrolyte [121, 122]. Consequently, they are also quite appropriately referred to as “electric double layer capacitors.”

A simple EC can be constructed by inserting two conductors in a beaker containing an electrolyte (Figure 1.15). Initially, there is no measurable voltage between the two rods, but when the switch is closed and a battery causes the current to flow from one rod to the other, charge separation is naturally created at each liquid–solid interface. This process effectively creates two capacitors that are series-connected by the electrolyte. Voltage persists after the switch is opened—energy has been stored. In this state, solvated ions in the electrolyte are attracted to the solid surface by an equal but opposite charge in the solid. These two parallel regions of charge are the source of the term “double layer.” Charge separation is measured in molecular dimensions (i.e., a few angstroms); the surface area is measured in thousands of square meters per gram of electrode material, creating 5-kF capacitors that can be hand-held. The very feature of an electrochemical capacitor that makes such high capacitances possible, namely the highly porous high-surface-area electrodes, is also the reason for the relatively slow response of these devices relative to conventional capacitors. To illustrate the reason why, Figure 1.16 presents an idealistic representation of a cross-section of a pore in a nano-porous carbon material, in which a cylinder is filled with electrolyte and an electric double layer covers the interior wall surface of the pore [123]. Electrical connections to the stored charge are made through the solid carbon surrounding the pore and through the electrolyte from the mouth of the pore—electrolyte conductivity being much lower than carbon conductivity. Charge stored near the pore’s mouth is accessible through a short path with small electrolyte resistance. In contrast, charge stored deeper within the pore must traverse a longer electrolyte path with a significantly

higher series resistance. Thus, the overall response can be represented by a multiple-time-constant equivalent circuit model [124–126]. Irrespective of this behavior, the response time of an electrochemical capacitor in both charge and discharge operation is extremely short (ca. 1 s) relative to that of batteries (minutes to tens of minutes; Table 1.4).

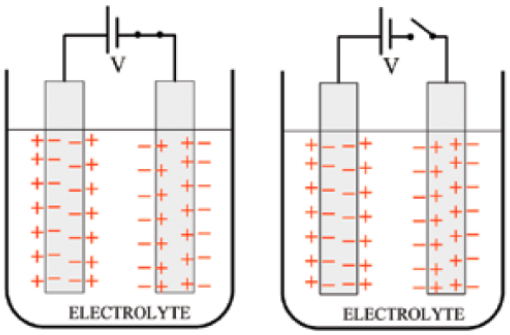

Figure1.15 Schematic representation of an electric double layer capacitor constructed by inserting two electrodes into a beaker and applying a voltage. The voltage persists after the switch is opened (right), creating two series-connected capacitors. Charges in the electric double layer are separated by only ca. 1 nm.

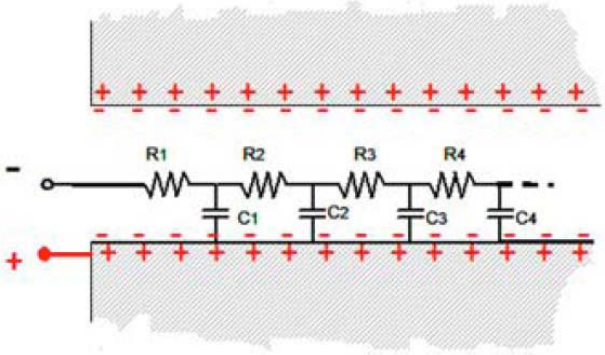

Figure 1.16 Schematic representation of an electrolyte-filled right-cylindrical nanopore in the carbon electrode of an electrochemical capacitor, displaying the distributed resistance from the electrolyte and distributed charge storage down the interior surface of the nanopore.

Table 1.4 Properties of secondary batteries and electrochemical capacitors.

Property	**Battery**	**Electrochemical capacitor**
Storage mechanism	Chemical	Physical/ Chemical
Power limitation	Active materials conductivity, electrochemical reaction kinetics, mass transport	Electrolyte conductivity in (porous) materials/ active materials conductivity, electrochemical reaction kinetics
Energy limitation	Bulk mass	Electrode surface area/ Bulk mass
Charge rate	Reaction kinetics, mass transport	High (same as discharge rate)
Cycle-life limitation	Chemical reversibility	Side reactions
Durability limitation	Thermodynamic stability	Side reactions

The utilization of this principle to store electrical energy for practical purposes, as in a cell or battery of cells, seems to have been first proposed and claimed as an original development in the patent granted to Becker in 1957 [127]. The patent described electrical energy storage by means of charge held in the interfacial double layer at a porous carbon material perfused with an aqueous electrolyte. The principle involved is the charging of the capacitance (C_{dl}) of the double layer, which arises at all solid–electrolyte interfaces (e.g., at metal, semiconductor, and colloid surfaces) and also at the phase boundary between two immiscible electrolyte solutions [128].

1.2.1 Faradaic and non-faradaic processes

The important differences in the charge storage processes are described below.

1.2.1.1 Non-faradaic process

In this process, charge storage is achieved electrostatically by positive and negative charges residing on two interfaces separated by a vacuum or a molecular dielectric (the double layer or, for example, a film of mica, a space of air, or an oxide film, as in electrolytic capacitors).

1.2.1.2 Faradaic process

In this process, charge storage is achieved through an electron transfer that produces chemical or oxidation state changes in the electroactive materials, according to Faraday's laws related to electrode potential. Pseudocapacitance can arise in some cases. The energy storage is indirect and is analogous to that in a battery. In a battery cell, every electron charge is faradaically neutralized through charge transfer, resulting in a change in oxidation stage of some redox-electroactive reagent.

In a capacitor, actual electron charges, either in excess or deficiency, are accumulated on the electrode plates with lateral repulsion and no involvement of redox chemical changes. In some cases of double-layer charging, however, some partial electron transfer occurs, giving rise to pseudocapacitance. The electrons involved in double-layer charging are the delocalized conduction band electrons of the metal or carbon electrode; in contrast, the electrons involved in faradaic battery-type processes are transferred to or from valance electron states (orbitals) of the redox cathode or anode reagent—although they may arrive in or depart from the conduction band states of the electronically conducting support material. In certain cases, the faradaically reactive battery material itself is metallically conducting (e.g., RuO_2); otherwise, it is a well-conducting semiconductor and a proton conductor (e.g., NiOOH).

1.2.2 Classification of electrochemical capacitors [121]

Table 1.5 summarizes the types of capacitors and their modes of energy storage as either electrostatic or faradaic—the latter in the case when pseudocapacitance arises. Types d and f are the principal kinds treated herein.

Normally, capacitors function as elements of electronic circuits or communications equipment, or as ballast for starting electric motors or electric discharge tubes (fluorescent lights). Devices exhibiting very large capacitance are now available for storing electric energy in various applications.

ECs have been an important development in recent years in the field of energy storage. They can be divided into three categories: traditional capacitors, electric double-layer capacitors, and pseudocapacitors.

1.2.2.1 Traditional capacitors

In a conventional capacitor, energy is stored by the removal of charge carriers, typically electrons, from one metal plate and depositing them on another. This charge separation creates a potential between the two plates, which can be harnessed in an external circuit. The total energy stored in this manner is proportional to both the number of charges stored and the potential between the plates. The former is essentially a function of size and the material properties of the plates; the latter is limited by the dielectric breakdown between the plates. Different materials sandwiched between the plates to separate them result in different voltages being stored. Optimizing the material leads to higher energy densities for any given size of capacitor.

1.2.2.2 Electric double-layer capacitor

Electric double-layer capacitors (Figure 1.17), also known as supercapacitors, electrochemical double layer capacitors (EDLCs), or ultracapacitors, are electrochemical

capacitors that have an unusually high energy density relative to those of conventional capacitors—typically on the order of thousands of times greater than that of a high-capacity electrolytic capacitor.

Table 1.5 Types of capacitors and their modes of energy storage

Type	Basis of charge or energy storage	Examples
(a) Vacuum	Electrostatic	—
(b) Dielectric	Electrostatic	Mica, paper
(c) Oxide electrolyte (thin film)	Electrostatic	Al_2O_3
(d) **Double-layer**	Electrostatic (charge separation at double-layer at electrode interface)	Carbon preparations, powders, fibers
(e) Colloidal electrolyte	Electrostatic (special double-layer system)	—
(f) **Redox oxide film**	Faradaic charge transfer (pseudocapacitance)	RuO_2, MnO_2, NiO
(g) Redox polymer film	Faradaic charge transfer (pseudocapacitance)	Polyaniline, polythiophenes
(h) Soluble redox system	Faradaic charge transfer (pseudocapacitance)	$Fe(CN)_6^{4-}$, $Fe(CN)_6^{3-}$

In contrast to traditional capacitors, electric double-layer capacitors do not possess a conventional dielectric. Rather than two separate plates separated by an intervening substance, these capacitors use “plates” that are in fact two layers of the same substrate; their electrical properties, the so-called “electrical double layer,” result in the effective separation of charge despite the vanishingly thin (on the order of nanometers) physical separation of the layers. The lack of a bulky layer of dielectric permits the packing of “plates” having a much larger surface area into a given size, resulting in their extraordinarily high capacitances in practical sized packages.

In an electrical double layer, each layer by itself is quite conductive, but the physics at the interface where the layers are effectively in contact means that no significant current can flow between the layers. The double layer can, however, only withstand a low voltage, which means that electric double-layer capacitors rated for higher voltages must be made of matched series-connected individual electric double-layer capacitors, much like series-connected cells in higher-voltage batteries.

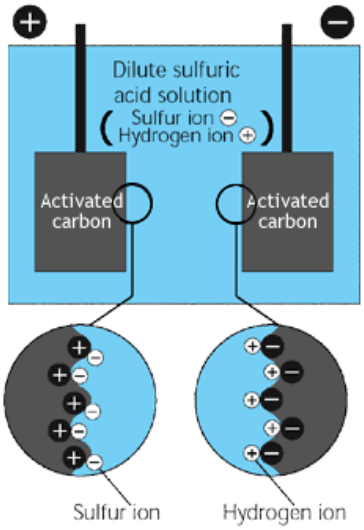

Figure 1.17 Schematic representation of an electric double-layer capacitor in an aqueous electrolyte.

1.2.2.3 Pseudocapacitor

A different kind of capacitance can arise at electrodes of certain kinds (e.g., RuO_2) when the extent of faradaically admitted charge depends linearly, or approximately linearly, on the applied voltage. For such a situation, the electrode behavior is equivalent to, and measurable as, a capacitance. This capacitance can be large, but it is faradaic and not electrostatic (i.e., non-faradaic) in origin—an important difference from the nature of double-layer capacitance—and, therefore, it is called "pseudocapacitance." This kind of pseudocapacitance can originate when an electrochemical charge-transfer process occurs to an extent limited by a finite quantity of reagent or of available surface. Several examples of pseudocapacitance can arise, but the capacitance function is usually not constant; in fact, it is usually appreciably dependent on the potential or state of charge.

When the process is surface-limited, however, and proceeds in several one-electron stages, a broad range of significant capacitance values arise—as is found with RuO_2 electrodes, where the pseudocapacitance is almost constant (within 5%) over the full operating voltage range. Some other metal oxides behave similarly, but only over smaller operating voltage ranges. The RuO_2 pseudocapacitance is one of the best examples of electrochemical (pseudo) capacitance because, in addition to the almost-constant capacitance over a wide voltage range, its reversibility is excellent, with a cycle life over several hundred thousand cycles. Furthermore, the pseudocapacitance can increase the capacitance of an electrochemical capacitor by as much as an order of magnitude over that of the double-layer capacitance. Its cost, however, prevents its large-scale use; therefore, such systems are employed mainly in military applications.

1.2.2.4 Conducting polymer capacitor

Another type of material exhibiting highly reversible pseudocapacitive behavior is the family of conducting polymers, such as polyaniline and derivatives of polythiophene. These polymers are cheaper than RuO_2, but are less stable, giving only thousands of cycles (still quite attractive) over a wide voltage range. Although polymer-based capacitors do not possess great durability, they have attracted much attention recently because they exhibit high working potentials (up to 3.5 V); i.e., they have higher power density.

1.3 Motivation for this Thesis

Carbon is an element almost uniquely suited to the fabrication of electrochemical capacitors of the double-layer type. It exists in several, well-know allotropic forms—diamond, fullerenes, and graphite—with the latter and glassy carbon capable of being generated in the form of high-area fibers and felts, which are particularly convenient materials for the formation of electrode structures having good mechanical integrity. From an electrochemical point of view, carbon is relatively unreactive and, thus, it has a potential voltage range of almost ideal polarizability, approaching 1.0 V in aqueous solution and possibly up to 3.5 V in nonaqueous media. The use of high-area carbon systems may lead to the commercial production of practical high-capacitance electrochemical capacitors. Therefore, we attempted to modify carbon nanomaterials and utilize them as electrode materials to facilitate the performance of electrochemical capacitors. In particular, we sought a way to transform normal 2-D CNWs into 3-D configurations.

Chapter 2 Literature Review

2.1 Purification of CNTs

Many synthetic techniques have been developed to activate CNT growth; metal catalysts are generally necessary. CNTs may find limited use for some applications because they contain small fractions of metal catalysts in their tubes and tend to have defects along the graphene tube wall. Defects within MWCNTs weaken their electrical and structural properties. Many methods have been investigated recently to remove impurities from carbon soot [129–134].

2.1.1 ····· Thermal oxidation

One of the most efficient purification methods, reported by Tsang et al. [135], is oxidation in air at 750 °C. Because of the small difference in reactivity between MWCNTs and carbon nanoparticles, pure MWCNTs are obtained after prolonged oxidation. Subsequently, many researchers [136–138] have adopted thermal annealing or similar thermal oxidation methods to purify CNTs, but with low yield.

2.1.2 ····· Microfiltration and ultrasonically assisted filtration

In addition to thermal oxidation, Shelimov and co-workers [139] proposed a method to purify SWCNTs using ultrasonically assisted filtration. In this method, sample sonication during filtration prevents filter contamination and provides a fine CNT/nanoparticle suspension. Amorphous and crystalline carbon impurities and metal particles are removed from the SWCNT samples through ultrasonically assisted microfiltration. The process generates SWCNT materials having purities of greater than 90% and in yields of 30–70%. Although this method can be used to separate coexisting carbon nanospheres, metal

nanoparticles, polyaromatic carbons, and fullerenes from the CNT fraction, metal catalysts embedded in the tip and wall structures cannot be eliminated. One advantage of the microwave digestion method is that the embedded metal catalyst can be eliminated to improve the purity of the CNTs.

2.1.3 ····· Acid treatment

A two-step process—thermal annealing in air and acid treatment—was proposed by Moon et al. [140] to purify SWCNTs. In particular, this purification process involved acid treatment with HCl for 24 h to etch away the catalytic metals, providing SWCNTs having metal contents of less than 1%. When optimized, this reproducible purification process provided total yield of ca. 25–30 wt%, with transition metal contents of less than 1%.

Zhang et al. [141] used thermogravimetric analyses to investigate the effect of PMMA and MCB on the purification and cutting of SWCNTs. Chattopadhyay et al. [142] proposed a method for the complete elimination of metal catalysts from SWCNTs. Chen and coworkers [143] developed a three-step purification of MWCNTs through which the raw material could be purified completely without damage. In general, acids (e.g., HF, H_2SO_4, HNO_3, HCl) are used to remove the metal catalysts. These processes involve repeated filtering and ultrasonication in acidic solution—e.g., stirring in 3 M HNO_3 and then heating under reflux for 24 h at 60 °C, and then filtering and re-suspending under reflux in 5 M HCl for 6 h at 120 °C. After acid treatment, the samples are calcined in static air at 510 °C for a reaction time of ca. 60 min. The total acid treatment processing time is generally greater than 30 h. Although the metals are successfully dissolved into solution, the CNTs might be cut into small lengths and, in some cases, destroyed. Indeed, the walls of CNTs are always damaged by strong acids. Kajiura et al. [144] reported a three-step purification process consisting of soft oxidation with 2.8 N HNO_3 for 6–24 h, air oxidation for 10 min at 550 °C, and high-temperature vacuum treatment for 3 h at 1600 °C. After the final step, ca. 20% of the weight of the initial raw soot

remained; the final product contained a metal content of less than 1%. Bandow et al. [145] developed a microfiltration-based purification method to separate carbon nanospheres, metal nanoparticles, polyaromatic carbons, and fullerenes from SWCNTs. Ando et al. [146] reported a procedure in which the MWCNTs were ground and boiled with 20% H_2O_2 under reflux for 45 h and then the residual material was heated under reflux for 24 h in a mixture of H_2SO_4 (96%) and HNO_3 (61%) at a ratio of 3:1.

2.1.4 Thermal oxidation combined with acid treatment

Another purification method to eliminate metal catalyst was proposed by Chiang et al. [147]. This method involves oxidizing the Fe catalyst and then dissolving the oxide. The raw material is heated in static air at 200 °C for 24 h and then sonicated in conc. HCl in a water bath at 80 °C for 15 min. Although the acid treatment time was only 15 min, the total purification time was greater than 24 h. We have found that microwave digestion, with a total acid treatment time of less than 2 h, can effectively eliminate catalyst particles from CNTs without introducing structural defects.

2.2 Fundamentals and structures of ECs

ECs have been known for many years; the first patents date back to 1957, when a capacitor based on high-surface-area carbon was described by Becker [127]. Later, in 1969, the first attempts to market such devices were undertaken by SOHIO [148]. It took until the 1990s for ECs to become famous in the context of their use in hybrid electric vehicles. A DOE ultracapacitor development program was initiated in 1989, with short- and long-term goals being defined for 1998–2003 and after 2003, respectively [149]. The ECs boost the battery or the fuel cell in the hybrid electric vehicle to provide the necessary power for acceleration, and additionally allow for recuperation of brake energy. Today, several companies, including Maxwell Technologies, Siemens Matsushita (now EPCOS), NEC, Panasonic, ELNA, and

TOKIN, are invested in the development of ECs. The applications envisioned for ECs are principally as boost components supporting batteries or replacing batteries in electric vehicles. In addition, alternative applications of ECs—not competing with batteries but with conventional capacitors—are arising and have considerable market potential. Such applications are discussed in detail in the second part of this Chapter. The reason why ECs have been able to raise considerable attention is depicted schematically in Figure 2.1, where typical energy storage and conversion devices are presented in the so called "Ragone plot" in terms of their specific energy and specific power. ECs fill the gap between batteries and conventional capacitors, such as electrolytic capacitors or metallized film capacitors. In terms of specific energy and specific power, this gap covers several orders of magnitude. Batteries and low temperature fuel cells are typical low power devices, whereas conventional capacitors may have a power density of greater than 10^6 W/dm^3 at a very low energy density. Thus, ECs may improve battery performance in terms of power density or may improve capacitor performance in terms of energy density when combined with the respective devices. In addition, ECs are expected to have much longer cycle lives than batteries because no (or negligibly small) chemical charge transfer reactions are involved. A monograph volume on ECs was recently published by Conway [121].

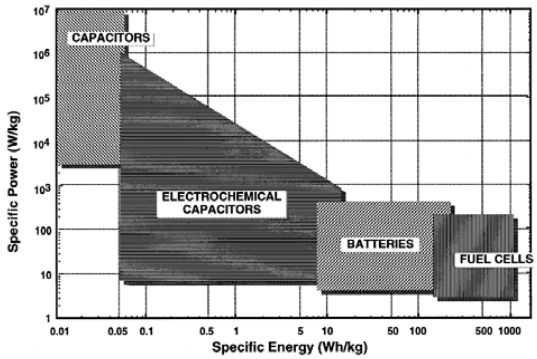

Figure 2.1 Ragone plot for various energy storage and conversion devices.

2.2.1 Principle of energy storage

ECs store electrical energy in an electrochemical double layer (Helmholtz layer) formed at a solid–electrolyte interface (Figure 2.2). Positive and negative ionic charges within the electrolyte accumulate at the surface of the solid electrode and compensate for the electronic charge at the electrode surface. The thickness of the double layer depends on the concentration of the electrolyte and on the size of the ions; it is on the order of 5–10 Å for concentrated electrolytes. The double layer capacitance is ca. 10–20 mF/cm^2 for a smooth electrode in a concentrated electrolyte solution; it can be estimated according to the equation

$$\mathbf{C / A = \varepsilon_0 \varepsilon_r / d} \qquad (2.1)$$

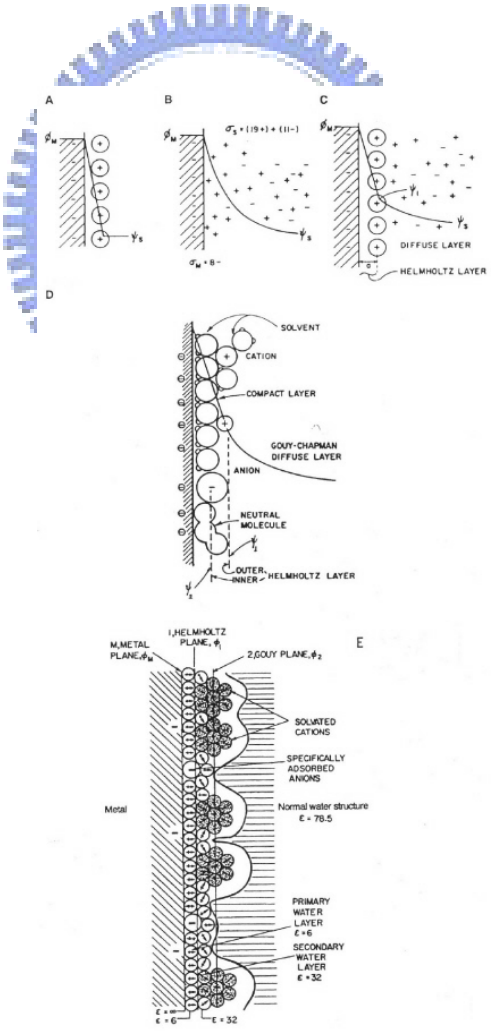

Figure 2.2 Schematic representation of a double-layer structure.

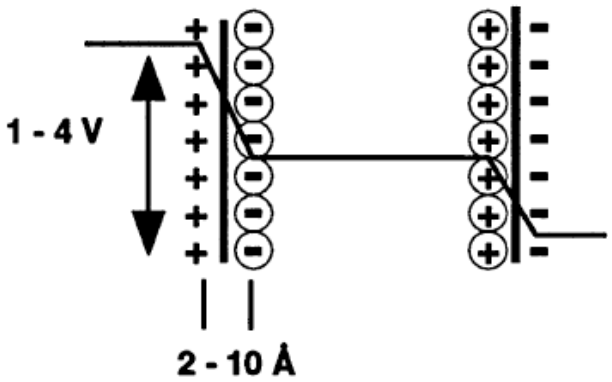

Figure 2.3 Schematic representation of the potential drop at the electrode–electrolyte interface.

assuming a relative dielectric constant of 10 for water in the double layer, with *d* being the thickness of the double layer having a surface area *A*. The corresponding electric field in the electrochemical double layer is very high, assuming a value of up to 10^6 V/cm quite easily. Relative to conventional capacitors, where a total capacitance on the pico- or millifaraday level is typical, the capacitance of and the energy density stored in the electrochemical double layer is rather high; therefore, the idea to build a capacitor based on this effect is tempting.

To achieve a higher capacitance, the electrode surface area is additionally increased by using porous electrodes having an extremely large internal effective surface. The combination of two such electrodes gives an EC having a rather high capacitance. Figure 2.3 presents a schematic representation of an electrochemical double-layer capacitor consisting of a single cell featuring a high-surface-area electrode material, which is loaded with an electrolyte. The electrodes are separated by a porous separator containing the same electrolyte as the active material. The potential drop across the cell is also indicated. The capacitance of a single electrode can be estimated by assuming a high surface area for carbon of 1000 m^2/g and a double-layer capacitance of 10 mF/cm^2, leading to a specific capacitance of 100 F/g for one electrode. For a capacitor, two electrodes are needed with doubled weight and half the total capacitance ($1/C = 1/C_1 + 1/C_2$), resulting in a value of 25 F/g for the active capacitor mass in this example. The difference between the single electrode values and the specifications given

for the complete capacitor is of significant importance. Whenever the specifications of an EC are given, one should indicate whether the values correspond to a single electrode measurement or are calculated for a complete capacitor. These values differ by a factor of four—not an insignificant amount. The maximum energy stored in such a capacitor is given by

$$W = 1/2\ C\ U_0^2 \qquad (2.2)$$

With a cell voltage U_0 of 1 V (aqueous electrolyte), one obtains a specific energy of ca. 3.5 Wh/kg of active mass. For an organic electrolyte having a typical cell voltage of 2.3 V, the active mass is ca. 18 Wh/kg. These values are considerably lower than those obtained for available batteries, but are much higher than those of conventional capacitors. Note that these values depend on the double layer capacitance, the specific surface area of the respective electrode materials, the wetting behavior of the pores, and the nominal cell voltage.

2.2.2 Electrode material

There are three main categories of electrode materials: carbon-based, metal oxide, and polymeric materials. A comprehensive review of possible electrode materials suitable for ECs has been given by Sarangapani [150].

2.2.2.1 Carbonaceous material

Carbon, in its various modifications, is the electrode material used most frequently for the electrodes of electrochemical capacitors. Reasons for using carbon are manifold: (i) low cost, (ii) high surface area, (iii) availability, and (iv) established electrode production technologies. Carbonaceous materials are available as powders, woven cloths, felts, and fibers with specific surface areas of up to 2500 m^2/g.

Charge storage on carbon electrodes is predominantly capacitive in the electrochemical double layer. Carbon-based electrochemical capacitors come close to what one would call an electrochemical double layer capacitor. There are, however, contributions from surface functional groups, which are generally present on activated carbons; they can be charged and uncharged, giving rise to pseudocapacitance.

Typical cyclic voltammograms for an activated glassy carbon electrode are reproduced in Figure 2.4 for electrochemically activated glassy carbon in both aqueous and non-aqueous electrolytes [151, 152]. The rectangular shape expected for an ideal capacitor is best approached in an organic electrolyte; the redox peak at ca. 0.4 Ωsce in the aqueous electrolyte is a contribution from surface functional groups. This corresponding pseudocapacitance is significantly reduced in organic electrolytes because protons are not available. Nakamura et al. [153] investigated the effects of surface functional groups containing oxygen atoms on the stability of carbon electrodes in ECs using organic electrolyte. They found that when the activated carbon was used for the anode, its stability increased upon increasing the oxygen content; in contrast, it decreased when used for the cathode. In general, both the stability and conductivity of the activated high-surface-area carbon decrease upon increasing the surface area [154].

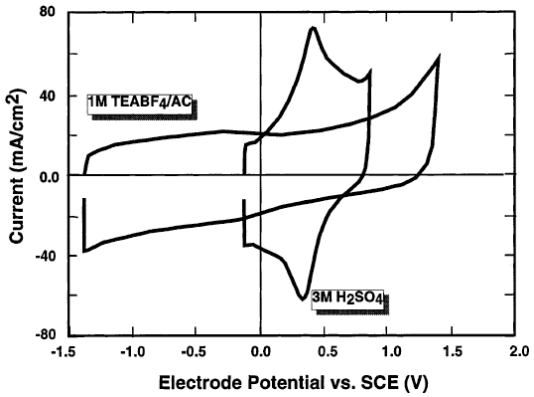

Figure 2.4 Cyclic voltammograms of activated glassy carbon electrodes at 100 mV/s in 3 M H_2SO_4 (aq.) and in 1 M $TEABF_4$ in acetonitrile. Both electrodes received the same electrochemical activation.

2.2.2.2 Metal oxides

The cyclic voltammograms of RuO_2 (and IrO_2) electrodes have an almost rectangular shape and exhibit good capacitor behavior [155, 156]. The shape of the cyclic voltammogram is, however, not a consequence of pure double layer charging, but of a sequence of redox reactions occurring in the metallic oxide. The valence state of Ru may change from III to VI within a potential window of slightly greater than 1 V. The ratio of surface charging to bulk processes was determined carefully by Trasatti [155].

In aqueous acidic electrolytes, the fundamental charge storage process is proton insertion into the bulk material. Very high specific capacitances (up to 750 F/g) were reported for RuO_2 electrodes prepared at relatively low temperatures [157]. Conducting metal oxides, such as RuO_2 and IrO_2, were the favored electrode materials used in the early ECs prepared for space or military applications [158]. The high specific capacitance in combination with low resistance resulted in very high specific powers. These capacitors, however, turned out to be too expensive. A rough calculation of the capacitor cost revealed that 90% of the cost resided in the electrode material. In addition, these capacitor materials are suitable only for aqueous electrolytes, thereby limiting the nominal cell voltage to 1 V.

Several attempts have been undertaken to reduce the cost of such metal oxides while maintaining their advantageous material properties. Guther et al. [159] investigated the effect of dilution of the costly noble metal by forming perovskites. Other forms of metal compounds, such as nitrides, were investigated by Liu et al. [160]. Nevertheless, these materials are far from being commercially used in ECs.

2.2.2.3 Polymers

Several authors [161–163] have suggested using polymeric materials, such as *p*- and *n*-dopable poly(3-arylthiophene), *p*-doped polypyrrole, poly(3-methylthiophene), and poly(1,5-diaminoanthraquinone), as electrodes for electrochemical capacitors. The typical

cyclic voltammogram of a polymer does not, however, have the rectangular shape expected for a typical capacitor; instead, it exhibits a current peak at the respective redox potential of the polymer. Polymers that undergo cathodic and anodic redox processes have been utilized recently in an attempt to use one and the same electrode material on both capacitor electrodes [163].

Using a polymeric material for the electrochemical capacitor electrodes gives rise to a debate as to whether such devices should still be called capacitors or whether they are better described as batteries. In terms of the voltage transient during the charge and discharge processes, and with respect to the cyclic voltammograms, they are batteries. Relative to metallic oxides, however, the term capacitor is justified. The difference being only that the metallic oxides exhibit a series of redox potentials, giving rise to an almost rectangular cyclic voltammogram, whereas the polymer typically exhibits only one redox peak.

Rather high energy densities and power densities have been reported for such capacitors [163]. The long-term stability during cycling, however, may be a problem. The swelling and shrinking of electroactive polymers are well-known phenomena that may lead to degradation during cycling.

2.2.3 Electrolyte

Another criterion with which to classify electrochemical capacitors is the electrolyte used. Most presently available capacitors use organic electrolytes.

2.2.3.1 Non-aqueous electrolytes

The advantage to using an organic electrolyte is a higher achievable voltage. According to Eq. (2), the square of the unit cell voltage determines the maximum stored energy. Organic electrolytes allow for a unit cell voltage of greater than 2 V. Typically, the cell float voltage is 2.3 V with the possibility to increase the voltage for a short time to 2.7 V. The cell voltage is

most probably limited by the water content of the electrolyte. To achieve higher voltages, some companies plan to go up to a float voltage of 3.2 V; in such systems, extreme purification procedures of the special electrolyte must be applied and corrosion of the carbon electrodes must be reduced using special protective coatings [164]. Because similar problems concerning the potential window of the organic electrolyte are known from Li ion battery production, it is clear that they can be overcome.

On the other hand, organic electrolytes have a significantly higher specific resistance. Relative to a concentrated aqueous electrolyte, the resistance of an organic electrolyte is increased by a factor of at least 20—typically by a factor of 50. The higher electrolyte resistance also affects the equivalent distributed resistance of the porous layer and, consequently, reduces the maximum usable power, which is calculated according to

$$P = U^2/4R \tag{2.3}$$

where *R* represents the total effective series resistance (ESR). Part of the reduction in power is, however, compensated for by the higher cell voltage achievable with an organic electrolyte. A list of potential organic electrolytes for electrochemical capacitors has been reviewed [165].

2.2.3.2 Aqueous electrolytes

Aqueous electrolytes limit the unit cell voltage of the EC to typically 1 V, thereby reducing the available energy significantly relative to organic electrolytes. The advantages of using an aqueous electrolyte are a higher conductance (0.8 S/cm for H_2SO_4) and the fact that purification and drying processes during production are less stringent. In addition, the cost of aqueous electrolytes is usually much lower than that for suitable organic electrolytes. Capacitors built by NEC [166] and ECOND use aqueous electrolytes. Aiming for a high power density, a glassy carbon-based capacitor developed in our laboratories also uses an aqueous

electrolyte [167]. Note that the capacitor must be developed for one or the other electrolyte, not only because of material aspects but also because the porous structure of the electrode must be tailored for the size and properties of the respective electrolyte. To avoid problems associated with electrolyte depletion during charging of the EC, the electrolyte concentration must be high.

If the electrolyte reservoir is too small relative to the huge surface area of the electrodes, the performance of the capacitor will be reduced. This problem is particularly important for organic electrolytes, where the solubility of the salts may be low. Zheng and Jow found, however, that concentrations higher than 0.2 M were sufficient [168].

2.3 Electrochemical characteristic of porous electrodes

Porous electrodes are often described by a truncated RC-transmission line, according to Figure 2.5. The equivalent circuit of the pore of a porous electrode is approximated by a line of R and C elements representing the elemental double layer capacitance and the respective electrolyte resistance at a particular depth of the pore. The resistance of the bulk material is assumed to be much smaller than the electrolyte resistance. At high frequencies, the capacitors behave like small impedance elements ($Z = 1/j\omega C$) and the current flows predominantly along $R1$ and $C1$ into the bulk material; almost no current flows deep down the pore. Consequently, the resistance and double layer capacitance are reduced at high frequencies [169]. De Levie [170] has provided a more complete description of the behavior of porous electrodes. Assuming straight cylindrical pores of radius r and length l, a double layer capacitance, and an electrolyte conductivity k, the impedance is calculated according to

$$Z(\omega) = (R_w/j\omega C)^{1/2} coth(j\, R_w \omega C)^{1/2} \qquad (2.4)$$

Low frequency: $Z(0) = 1/(j\omega C)$

High frequency: $Z(\omega \rightarrow \infty) = (R_w/j\omega C)^{1/2}$

where R_W represents the low frequency resistance spanning the 45° Warburg region (Figure 2.6) and C represents the low frequency capacitance, which is determined by the product of the double layer capacitance and the total pore surface area. The total impedance of a capacitor would also include the ionic resistance of the bulk electrolyte and separator, as well as any contact resistance in the system. The total impedance would then be equal to $R_{contacts} + R_{sol} + Z(\omega)$. For a porous, highly conducting layer with a liquid electrolyte filling the pores, the low frequency resistance R_W depends only on the porosity and on the apparent conductivity (κ) of the electrolyte. The value of κ may be somewhat smaller than the bulk electrolyte conductivity if the pores are tortuous instead of straight [171].

$$R_w = L/(3\pi r^2 nk) \tag{2.5}$$

where L is the active layer thickness (the length of the pores for straight, cylindrical pores), r is the pore radius, and n is the number of pores. The porosity, the volume fraction of pores, would be $\pi r^2 n/A$, where A is the geometric electrode area and n the number of pores per volume.

For a theoretical estimation of the contribution of the active porous layer to the series resistance, the DeLevie transmission line model of a porous electrode can be applied with the straight pores considered as cylindrical capillaries [170]. The electrolyte conductivity is 0.8 S/cm (3 M H_2SO_4) and the double layer capacitance at the walls of the pores is assumed to be 10 mF/cm^2. The pores have a diameter of 3 nm and are arranged in a rectangular close-packed manner. The resulting porosity of the layer is 78%, with a pore density of 10^{13}/cm^2. Such a layer has a volumetric capacitance of 10^5 F/cm^3 and a specific resistance of 0.53 Ωcm (1.9 S/cm).

Figures 2.7 and 2.8 display impedance plots and capacitance-versus-frequency plots, respectively, for such layers having three different thicknesses. The capacitance is calculated from the imaginary part of the complex impedance, according to

$$C = -1/[\omega Im(Z)] \tag{2.6}$$

The impedance plot is equivalent to that sketched in Figure 2.6; the typical 45° Warburg region is visible for each of the three thicknesses. In this high frequency domain, the porous character of the active layer dominates. In the capacitance-versus-frequency plot, the capacitance begins to decrease noticeably at high frequency. The cut-off frequency is roughly related to the *RC* time constant of the single-electrode capacitor. At lower frequencies, the impedance plot (Figure 2.7) approaches a vertical line. A constant phase element (CPE) of 0.98 was assumed for the calculation. In the corresponding capacitance-versus-frequency plot, the capacitance levels off at lower frequencies.

Assuming the use of an organic electrolyte having a specific conductance of 0.04 S/cm, the very same electrode has a specific resistance of 10.6 Ωcm (0.09 S/cm).

The effect of the active layer thickness is demonstrated in Figures 2.7 and 2.8, where capacitance-versus-frequency plots are presented for electrodes having active layer thicknesses of 25, 50, and 100 mm. An increased film thickness leads to a higher capacitance at low frequencies—and, of course, to an increased distributed resistance of the film. These two factors cause a higher time constant *RC*, which is reflected by the lower cut-off frequency for thicker electrodes. The effects of the pore number and pore diameter are readily understood in the simple porous layer model. The equivalent resistance of the porous layer is directly proportional to the porosity of the layer—i.e., to the volume of electrolyte within the porous structure. Thus, an increase of the number of pores at a constant radius or an increase in the pore diameter at a constant number of pores results in increased capacitance and reduced resistance. An example is given for an increase in the pore diameter from 2 to 20 nm at a constant number of pores of $2.5 \times 10^{11}/cm^2$. The resulting porosity increases from 0.8 to 78%. The capacitance-versus-frequency plot in Figure 2.9 reveals both the increased capacitance and the increased cut-off frequency.

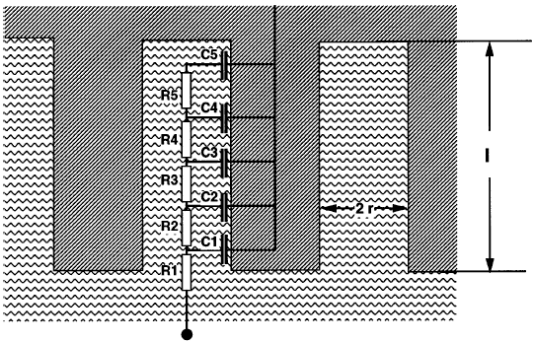

Figure 2.5 Equivalent circuit representation of the distributed resistance and capacitance within a pore. Five-element transmission line.

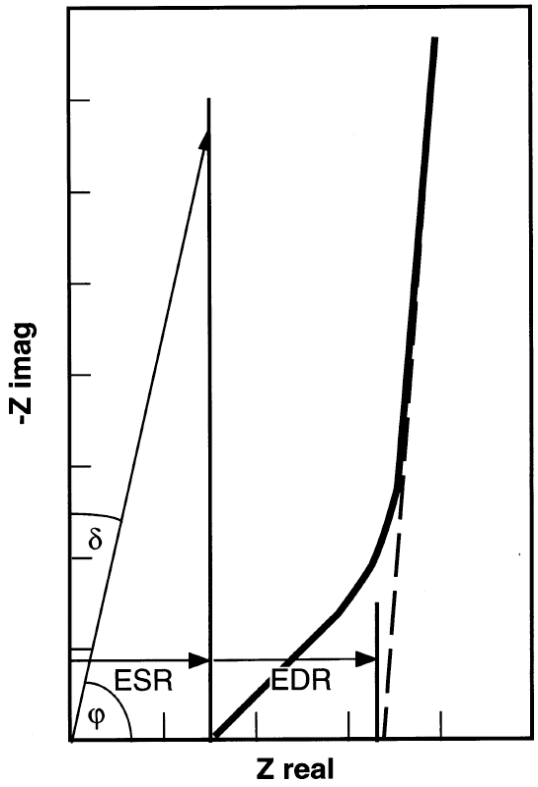

Figure 2.6 Nyquist impedance plots of an ideal capacitor (vertical thin line) and an electrochemical capacitor featuring porous electrodes (thick line).

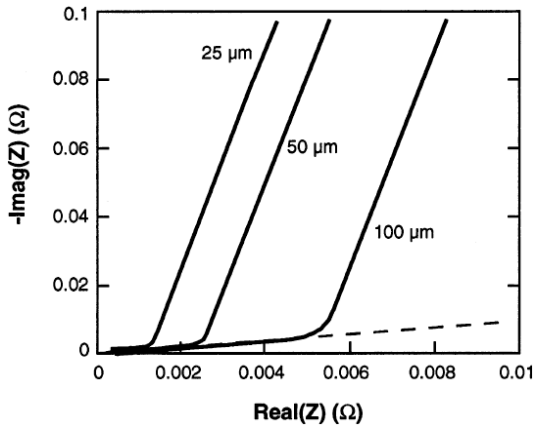

Figure 2.7 Calculated impedance plots for porous electrodes of various thicknesses. Assumptions: Double layer capacitance, 10 μF/cm^2; pore diameter, 3 nm; electrolyte conductivity, 0.8 S/cm; rectangular closed packed arrangement of pores, 10^{13}/cm^2; constant phase element exponent, 0.98.

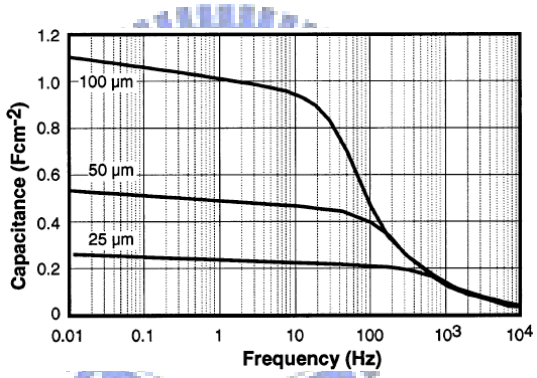

Figure 2.8 Capacitance-versus-frequency plots for the electrodes in Figure 2.7.

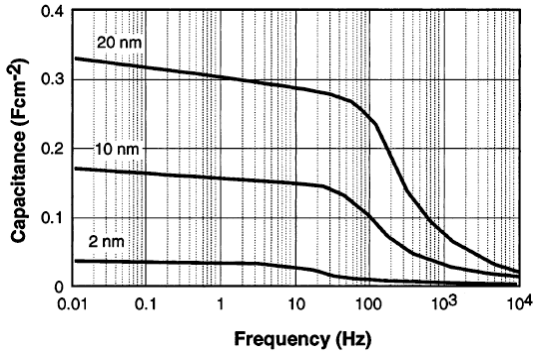

Figure 2.9 Effect of pore diameter on the capacitance-versus-frequency performance of a single porous electrode. Thickness of porous layer: 100 μm; CPE: 0.98; double layer capacitance: 20 μF; number of pores: 2.5×10^{11}/cm^2.

Chapter 3 Experimental Details

3.1 Experimental flow chart for the growth and characterization of carbon nanomaterials

Figure 3.1 presents an experimental flow chart for the growth and the electrochemical measurements of the carbon nanomaterials. In this study, SEM, TEM, Raman spectroscopy, X-ray diffraction, and cyclic voltammetry were used to characterize the carbon nanomaterials.

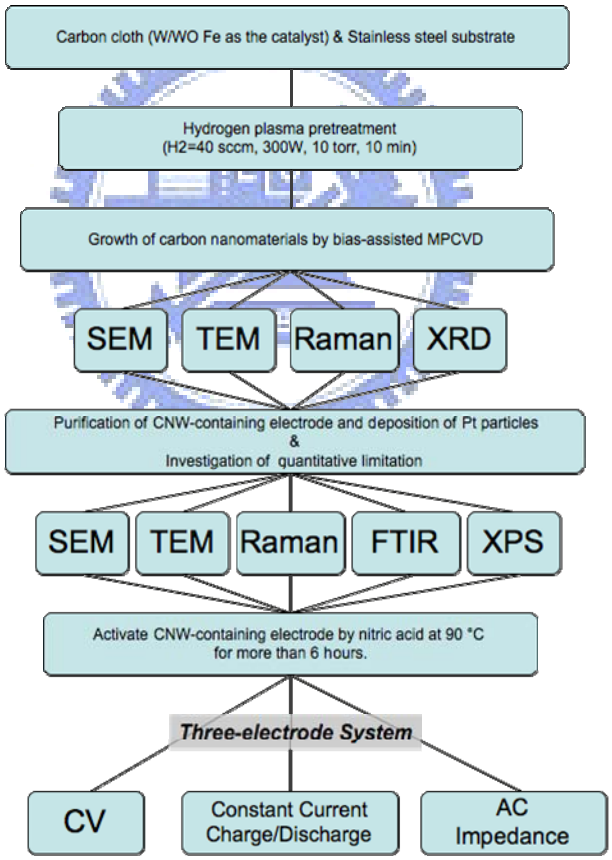

Figure 3.1 Experimental flow chart for the growth and characterization of carbon nanomaterials

3.2 Deposition system: Bias-assisted MPCVD

Figure 3.2 provides a schematic representation of the layout of the MPECVD system. A quartz tube was vertically attached to the rectangular waveguide used as the deposition chamber. The microwaves from a magnetron source (model IMG 2502-S, IDX Tokyo, Japan) were supplied to the quartz tube through an isolator and a power meter. The microwave power was then coupled to the quartz tube through an aluminum waveguide having a hole drilled through it from the top to bottom face. Aluminum tubes extend out from both holes; the tube extensions were water-cooled as well. A sliding short circuit was then attached at the end of the waveguide. The lower position of the quartz tube was connected a stainless-steel multi-port chamber equipped with a rotary pump.

The substrates were positioned in the middle of the quartz tube waveguide intersection and were held vertically by a substrate holder, which had a diameter of 20 mm and was made of molybdenum. A tantalum wire was attached under the holder; it was connected to the bias system and used as the lower electrode in the bias treatment stage. A quartz protector was placed under the holder to protect the plasma; it was not attracted to the tantalum wire attached to the molybdenum. The upper electrode, a molybdenum plate having a diameter of 20 mm, was placed 35 mm above the substrate and was also attached to a tantalum wire. Mass flow controllers (model 647B, MKS Instrument, Inc., USA) were used to control the amounts of the source gases introduced into the chamber from the upper end of the quartz tube. A small window was cut in the waveguide at the center of the plasma cavity, allowing direct observation of the plasma.

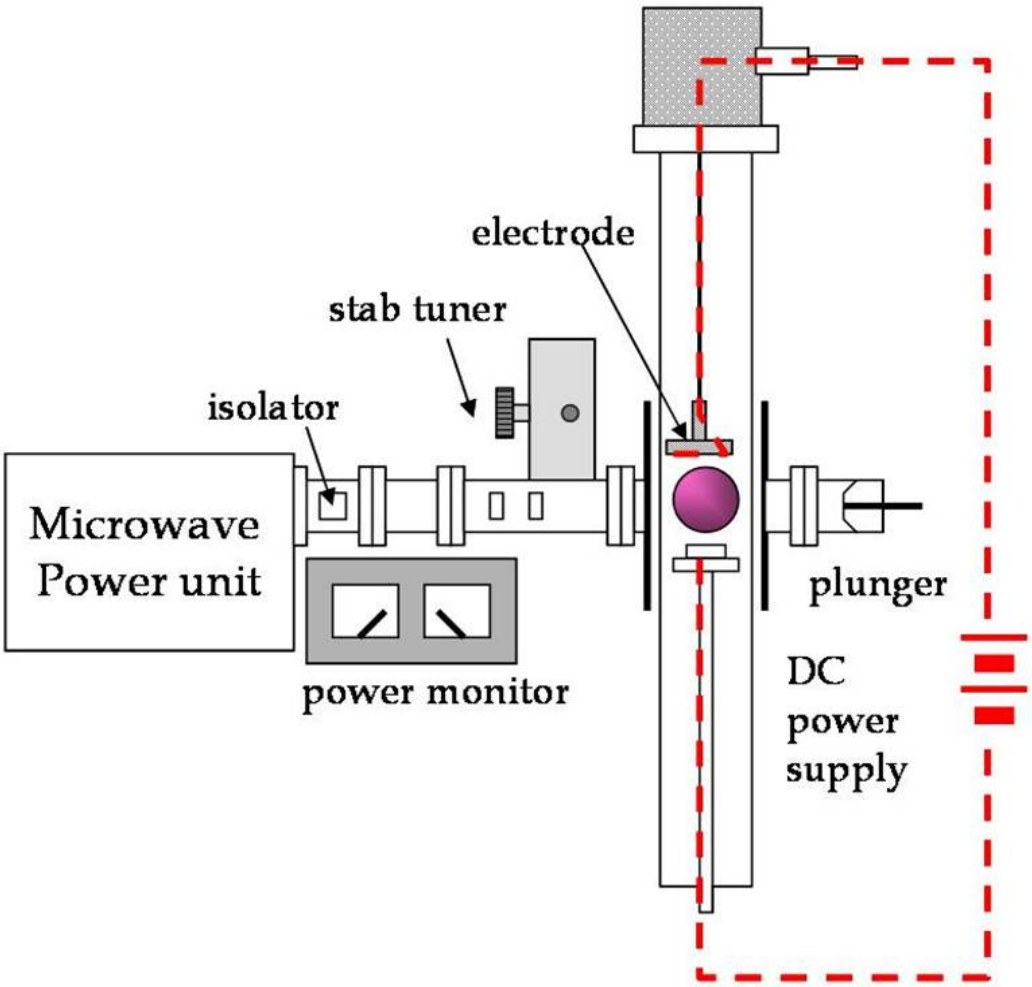

Figure 3.2 Schematic representation of the bias-assisted MPCVD system.

3.3 Analytical instruments

3.3.1 XPS

X-ray photoelectron spectroscopy (XPS) is a quantitative spectroscopic technique for measuring the elemental composition, empirical formula, and chemical and electronic states of elements within a material. XPS spectra are obtained by irradiating a material with a beam of aluminum or magnesium X-rays while simultaneously measuring the kinetic energy (KE) and number of electrons that escape from the top 1–10 nm of the material being analyzed. XPS requires ultra-high vacuum (UHV) conditions.

Because the energy of a particular X-ray wavelength is a known quantity, the electron binding energy (BE) can be determined for each of the emitted electrons, using an equation based on the work of Ernest Rutherford (1914):

$$E_{binding} = E_{photon} - E_{kinetic} - \Phi \quad (3.1)$$

where $E_{binding}$ is the energy of the electron emitted from one electron configuration within the atom, E_{photon} is the energy of the X-ray photons being used, $E_{kinetic}$ is the kinetic energy of the emitted electron as measured by the instrument, and Φ is the work function of the spectrometer (not the material).

3.3.2 Energy dispersive X-ray (EDX) analysis

EDX analysis is a microanalytical technique that uses the characteristic spectrum of X-rays emitted by a specimen after excitation with high-energy electrons to obtain information about its elemental composition. The ranges of elements detectable by EDX and electron energy loss spectroscopy (EELS) are somewhat complementary; EDX spectroscopy is generally better suited to detecting elements of high atomic number (Z), whereas EELS can readily detect low-Z elements. Unlike EELS, EDX spectroscopic analysis does not provide

chemical information (except through quantitative analysis in some cases). Relative to EELS, EDX is a relatively simple technique that provides rapid qualitative microanalysis of the specimen. The spatial resolution is determined by the probe size, beam broadening within the specimen, and the effect of backscattered electrons on the specimen around the point of analysis.

3.3.3 SEM

SEM can be used to observe the surface morphologies of a wide range of objects. It has the advantage of rather easy sample preparation, high image resolution, a large depth of field, and high magnification. A common scanning electron microscope (Figure 3.3) contains an electron gun to generate the electron beams, which are accelerated under voltages of 0.4–40 kV. By deflecting the incident beams with the focusing coils, a 2-D image can be obtained by detecting the reflected secondary electrons and the backscatter electrons. The model use here was a Hitachi S-4000 instrument equipped with a field emission electron source and operated at an accelerating voltage of 25 kV.

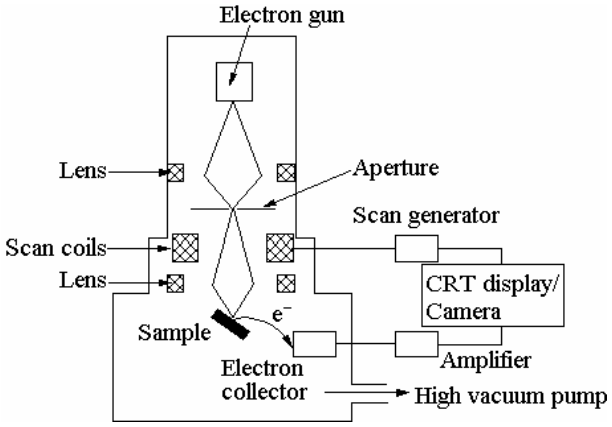

Figure 3.3 Schematic representation of a scanning electron microscope.

3.3.4 TEM

TEM is by far the most important technique for studying defects in great detail. Much of what was stated above regarding defects would be speculative theory, or would never have been conceived, if not for the development of TEM. In a typical TEM analysis, a static beam of electrons at an accelerating voltage of 100–400 kV illuminate a region of an electron-transparent specimen, which is immersed in the objective lens of the microscope. The transmitted and diffracted electrons are recombined by the objective lens to form a diffraction pattern in the back focal plane of that lens and a magnified image of the sample in its image plane. A number of intermediate lenses are used to project either the image or the diffraction pattern onto a fluorescent screen for observation. The screen is usually lifted and the image formed on photographic film for recording purposes. Figure 3.4 presents a schematic representation of a typical TEM instrument.

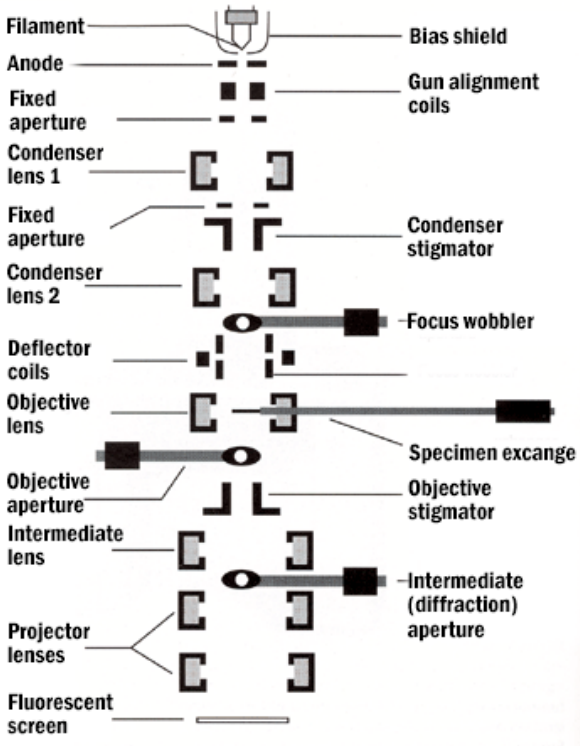

Figure 3.4 Schematic representation of a TEM instrument.

3.3.5 Raman spectroscopy

Raman spectroscopy is a powerful and nondestructive method for determining CNT structures; it is used widely to study the vibrational modes of carbon-based graphitic nanostructures. While photons illuminate a molecule or crystal, they react with the atoms with an accompanying momentum change or energy exchange. By collecting the scattered photons, a sequence of spectra can be obtained, including Raman scattering (inelastic scattering) and Rayleigh scattering (elastic scattering). The photons arising from Raman scattering can be classified into two groups: the Stokes side, in which photons lose energy or the molecules gain energy, and the anti-Stokes side, in which photons gain energy or molecules lose energy. Generally, the Stokes side is used to characterize the material. Because Raman spectra provide information relating to both crystallinity and bonding, the technique has become the most direct and convenient method of identifying carbon-related materials. The instrument used in this study was a HORIBA Jobin Yvon, HR800 (Figure 3.5). The source was a He-Ne laser having a wavelength of 632.82 nm and power of 12 mW. The spectral slit width was 0.4 cm^{-1}.

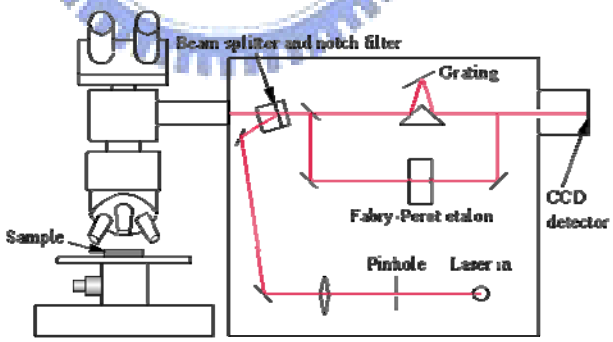

Figure 3.5 Schematic representation of a Raman spectroscope.

3.3.6 XRD

XRD (Figure 3.6) is a useful tool for analyzing the crystallinity of specimens and mean particle sizes. When X-ray radiation passes through matter, it interacts with the electrons in the atoms, resulting in scattering of the radiation. If the atoms are organized in planes and the

distances between the atoms are of the same magnitude as the wavelength of the X-rays, constructive and destructive interference will occur—resulting in diffraction, where X-rays are emitted at characteristic angles based on the spaces between the atoms organized in crystalline structures, called planes. Most crystals have many sets of planes passing through their atoms. Each set of planes has a specific interplanar distance and will give rise to a characteristic angle of diffracted X-rays. The relationship between the wavelength, atomic spacing (*d*), and angle is given by the Bragg equation: $n\lambda = 2d\sin\theta$. If the illuminating wavelength is known and the angle can be measured, then the interplanar distance can be calculated. A set of "*d*-spaces" obtained from a single compound will represent the set of planes that can be passed through the atoms; it can be compared with sets of d-spaces obtained from standard compounds.

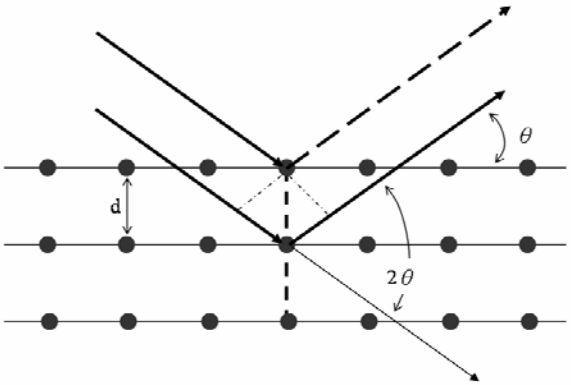

Figure 3.6 Schematic representation of Bragg's law.

3.3.7 Infrared (IR) spectroscopy

IR spectroscopy has been a workhorse technique for materials analysis in the laboratory for over 70 years. An IR spectrum represents a fingerprint of a sample, with absorption peaks that correspond to the frequencies of vibrations between the bonds of the atoms making up the material. Because each different material is a unique combination of atoms, no two compounds produce the exact same IR spectrum. Therefore, IR spectroscopy can result in a positive

identification (qualitative analysis) of different kinds of material. In addition, the sizes of the peaks in the spectrum provide a direct indication of the amount of material present. In conjunction with modern software algorithms, IR spectroscopy is an excellent tool for quantitative analysis, as illustrated schematically in Figure 3.7.

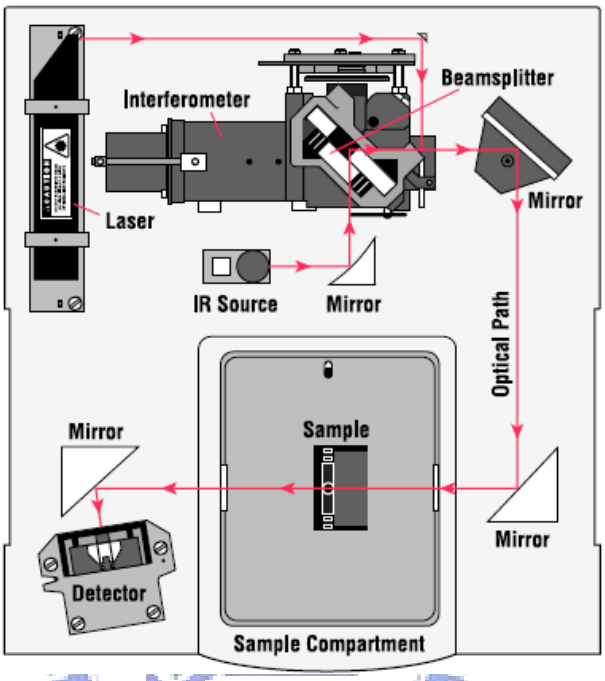

Figure 3.7 Schematic representation of a simple IR spectrometer layout [http://mmrc.caltech.edu/FTIR/].

3.3.8 Cyclic voltammetry (CV)

CV is the most widely used technique for acquiring qualitative information about electrochemical reactions. The power of CV results from its ability to rapidly provide considerable information on the thermodynamics of redox processes and the kinetics of heterogeneous electron-transfer reactions, and on coupled chemical reactions or adsorption processes. A simple potential waveform that is often used in electrochemical experiments is the linear waveform; i.e., the potential is continuously changed as a linear function of time. The rate of change of the potential with time is referred to as the scan rate (v). A more commonly used variation of the technique is CV, in which the direction of the potential is

reversed at the end of the first scan. Thus, the waveform usually has the form of an isosceles triangle. This approach has the advantage that the product of an electron transfer reaction that occurs in the forward scan can be probed again in the reverse scan. In addition, CV is a powerful tool for determining formal redox potentials, detecting chemical reactions that precede or follow the electrochemical reaction, and evaluating electron transfer kinetics. Figure 3.8 presents the experimental setup used herein for CV measurements. Cyclic voltammograms were recorded using a CH Instrument 6018B potentiostat and a three-electrode cell. A Pt wire served as the counter electrode; a saturated calomel electrode (SCE) was used as the reference electrode. The area of the working electrode was ca. 0.25 cm^2.

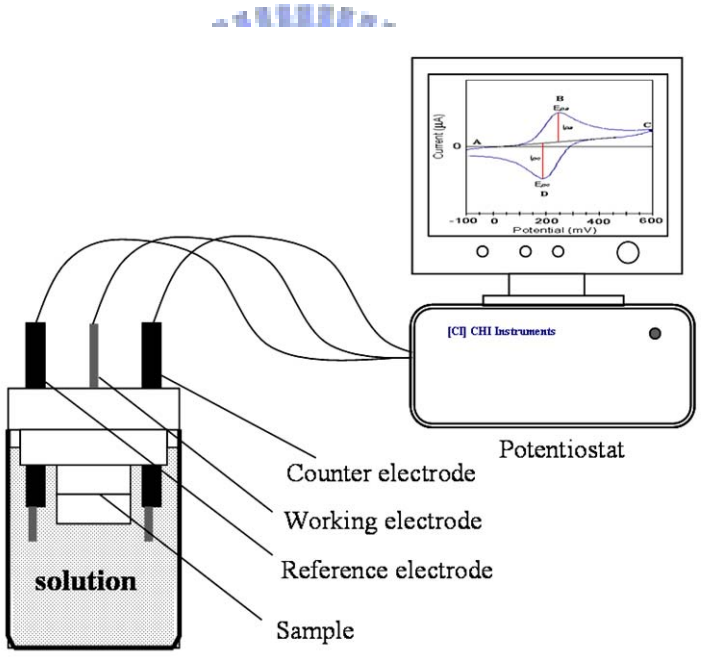

Figure 3.8 Schematic representation of a CV apparatus.

3.3.9 Brunauer–Emmit–Teller (BET) surface area

The BET method is applicable to the adsorption of multiple layers onto homogeneous surfaces and is a standard method for measuring surface area. The simplest BET isotherm is analyzed while taking several assumptions into consideration: (i) The gas adsorbs onto a flat,

homogeneous solid surface with a uniform heat of adsorption, due to van der Waals forces between the gas and the solid. (ii) No lateral interaction occurs between adsorbed molecules. (iii) After the surface has been partially covered by adsorbed gas molecules, additional gas can adsorb either on the remaining free surface or on top of the already adsorbed layer. (iv) The adsorption of the second and subsequent layers occurs with a heat of adsorption equal to the heat of liquefaction of the gas.

The pore size distributions and surface areas are determined from adsorption isotherms of a gas (usually N_2) at its boiling point being adsorbed on the solid sample. By measuring the volume of gas adsorbed at a particular partial pressure, the specific surface area of the material can be derived using the BET equation.

Chapter4 Synthesis of Carbon Nanomaterials by MPCVD system

4.1 Synthesis of MWCNTs on carbon cloth and stainless steel

4.1.1 Sample preparation and experimental procedures

Carbon cloth (CC) and stainless steel (SS) were used as the substrate. To synthesize carbon nanotubes on CC, catalyst was essential. Fe film was deposited on the substrate as the catalyst by magnetic sputtering. The deposition lasted for 30 min at the RF power of 40 W. The thickness of catalyst could be evaluated close to 20 nm. Afterwards, two kinds of substrates were treated for 10 minutes by hydrogen plasma, ignited by introducing hydrogen at a flow of 40 sccm at the pressure of 10 torr and the power of 300 W. Then, for synthesis, the gas was replaced by introducing a mixture of hydrogen and methane at the gas flow ratio of 3:1 at the same pressure and power and operated for 30 min.

Scanning electron microscope (SEM, JOEL JSM6700) and high-resolution transmission electron microscope (TEM, Philips Tecnai-20) were used to examine the morphology and structure of MWCNTs electrode. Finally, MWCNTs were characterized by Raman and XRD.

4.1.2 The effect of external bias on the formation of MWCNTs

Aligned MWCNTs arose on the carbon cloth as we can see in Figure 4.1 while an external negative bias of -150 V was applied on the lower electrode. On the contrary, without external bias in the MPCVD system, the MWCNTs became entangled on both electrodes as shown in Figure 4.2 and Figure 4.3. It should be noted that for SS substrate there have been no crystalline structures observed below the bias of -150 V.

The MWCNTs gathered densely on account of the interfacial Van der Waals force [172]. Actually, a self-potential occurs immediately on the surface of electrode when the plasma is

ignited [173, 50]. The intrinsic electric field was considered to be helpful on the alignment at the very early stage of deposition [52]. However, the electric field cannot afford the continual growth because of the existence of defects, like pentagon and heptagon [183]. In the case of applying an external bias strong enough, it would benefit the dissociation and dissolution of carbon nuclei and assure the anisotropic deposition of carbon atoms on the vapor-liquid-solid growth procedure [116, 117].

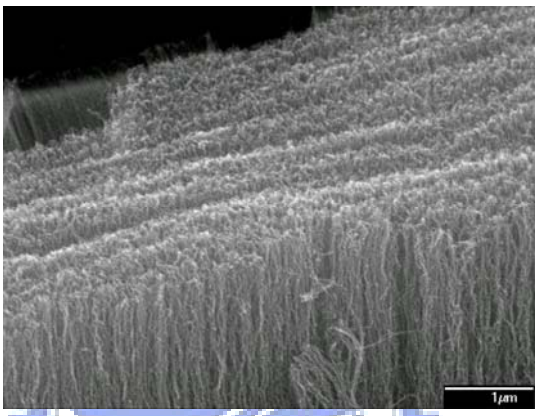

Figure 4.1 SEM image of the aligned MWCNTs synthesized on the Fe-coated carbon cloth substrate

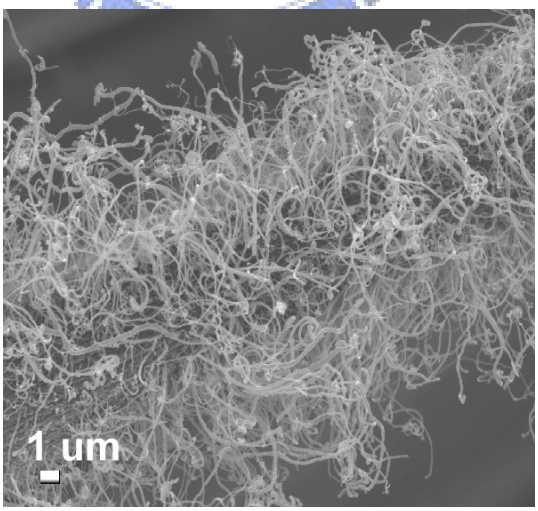

Figure 4.2 SEM image of the entangled MWCNTs synthesized on the Fe-coated carbon cloth substrate

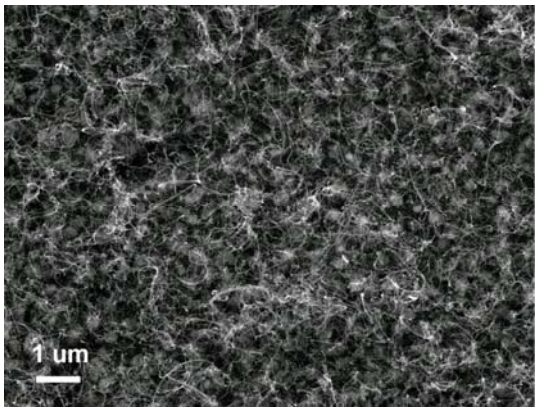

Figure 4.3 SEM image of the entangled MWCNTs synthesized on the stainless steel substrate

4.1.3 Characteristics of the aligned MWCNTs

Figure 4.4 shows the SEM image of aligned MWCNTs synthesized on the carbon cloth. The uniform length of MWCNTs was measured to be ca. 20 um. In the image, MWCNTs packed densely and grew up all over the substrate in the direction perpendicular to the substrate surface. Each of which was connected by the interaction of Van der Waals force shows a high degree of vertical with curved structure. The Van der Waals effect has been identified as the main factor in the aligned arrangement, especially for the growth mechanism of MWCNTs [172]. Figure 4.5 display the TEM images of the aligned MWCNT [4.5(a)] and interlaced MWCNTs on CC [4.5(b)] and SS [4-5(c)], respectively. It depicts that the growth could be classified as top-growth model with a catalytic particle encapsulated at the top end of MWCNT. The EDX measurement reveals that the catalyst for the growth of novel structure on SS substrate is consisted of only iron as depicted in Figure 4.5(d). In particular, it shows a bamboo-like structure with lots of extra structure within the nanotube separating the continuous tubular structure to several spaces in Figure 4.5(a). To characterize the MWCNTs, Raman and X-ray spectra are shown in Figure 4.6 and Figure 4.7. The Raman spectrum of the samples in the region 1200–1700 cm^{-1}depicts that the carbon material corresponds to the multi-wall carbon nanotube indeed with two charactering peaks at the wavenumber of 1350 cm^{-1} and 1580 cm^{-1}, denoted by D-band and G-band, respectively. We observe three distinct

peaks: a typical graphite vibration mode G-band at 1580 cm^{-1} and a disordered carbon mode D-band at 1348 cm^{-1}. The peak at 1580 cm^{-1} indicates that graphite structures were fabricated during growth; the peak at 1348 cm^{-1} resulted from defects in the curved graphite sheets, tube ends, and surviving impurities; The ratio of the D-band intensity to the G-band of the aligned CNTs was estimated to be 0.91. The other two were even larger than 1, representing the non-graphite is dominant. The diffraction result of the CC-related samples shows the characteristic of MWCNT with a specific plane of (002) at the diffraction angle of about 26° in two theta. In comparison, the diagram referring to the SS-related sample is not analogous to other studies with a sharp peak since presumably the intensity can also include the signal resulted from the amorphous carbon of substrate. The peak 2θ ~26° corresponds to the (002) plane of graphite. In addition to graphitic phase many small intensity peaks are also observed which corresponds to phase of Al, the holder.

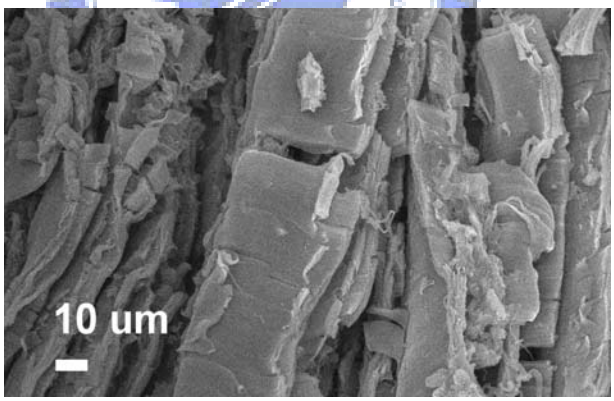

Figure 4.4 Low-magnified SEM image of the aligned CNTs electrode

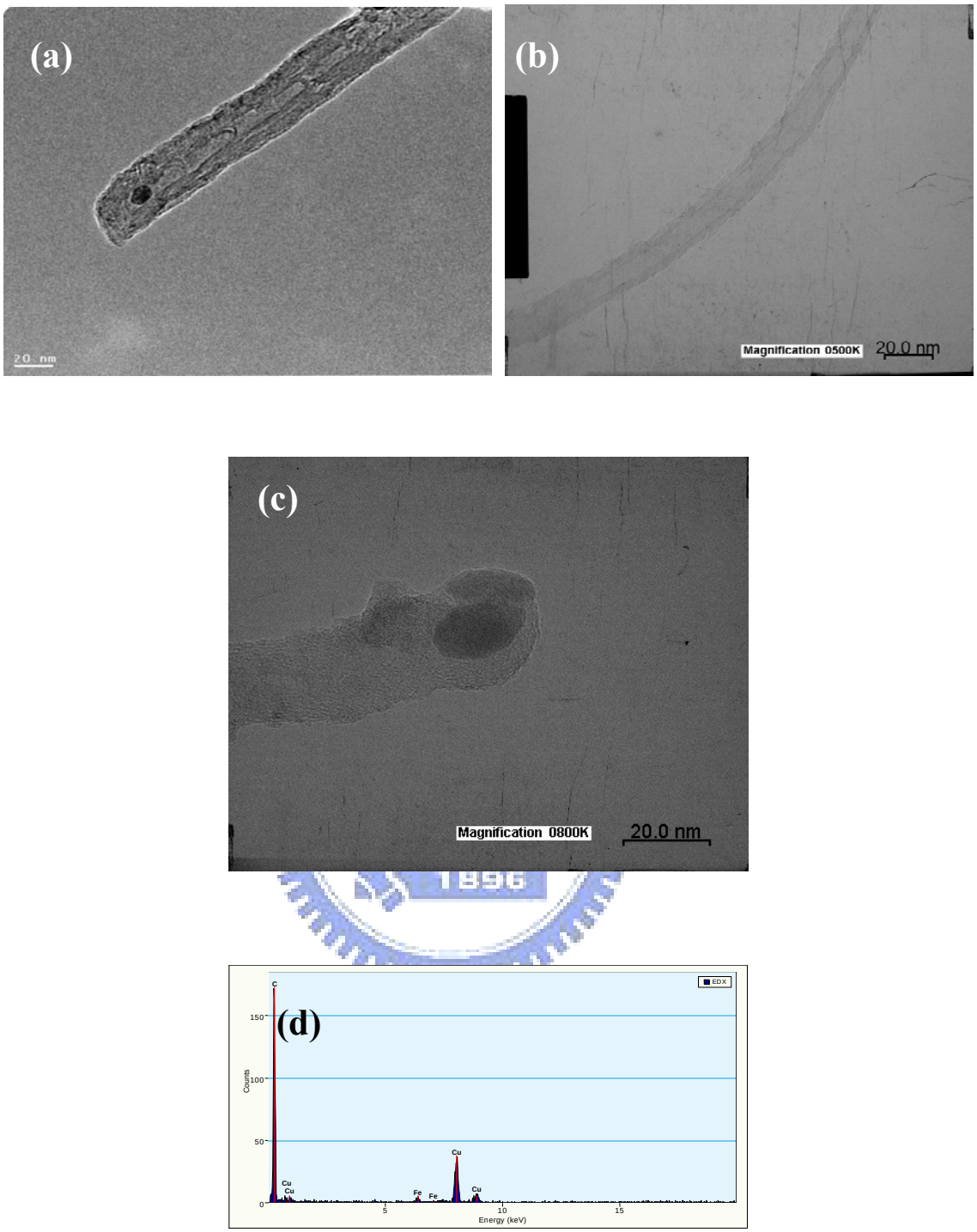

Figure 4.5 TEM images of (a) the aligned MWCNT (b) the entangled CNT synthesis on carbon cloth, (c) the entangled MWCNT on stainless steel plate, and (d) the EDX result of the catalyst encapsulated at the end of MWCNT of Figure 4.5(c).

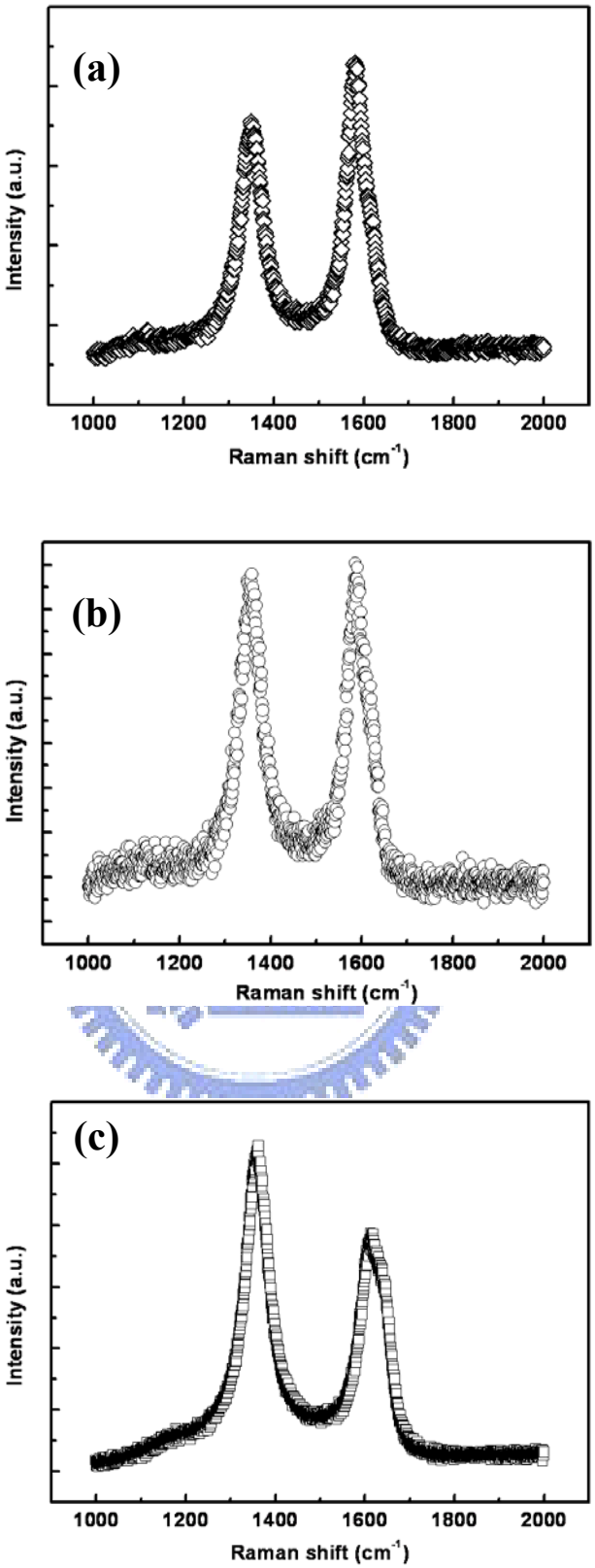

Figure 4.6 Raman shift spectra of (a) the aligned MWCNTs, (b) the entangled MWCNTs on carbon cloth, and (c) the MWCNTs on stainless steel plate.

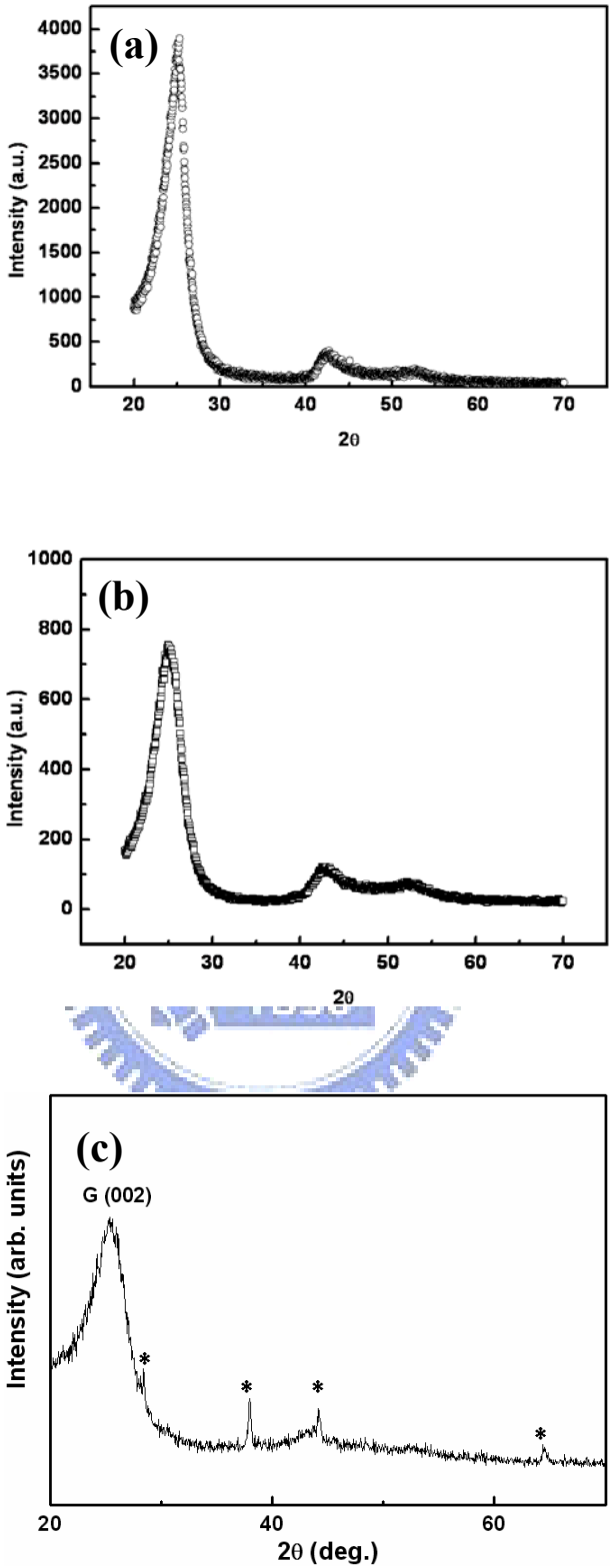

Figure 4.7 X-ray diffraction spectra of the electrodes containing (a) the aligned MWCNTs, (b) the entangled MWCNTs on carbon cloth, and (c) the MWCNTs on stainless steel plate (the peaks marked (*) refer to various phases of Al plate).

4.1.4 Summary

First, aligned multi-wall carbon nanotubes can be synthesized on the Fe-coated carbon cloth. Applying an external bias large enough is essential to achieve the vertical growth on the influence of anisotropic deposition of carbon. It is obvious that in comparison, interlaced MWCNTs appear without an external, negative bias applied on the electrode. Besides, the Van der Waals force between MWCNTs is helpful and necessary for the gathering of MWCNTs. The interfacial force is weak and benefits the dense arrangement. The growth mechanism follows the VLS mechanism. The Raman and X-ray measurements depict that the carbon nanomaterial is of crystalline property and corresponds to the common characteristics of MWCNTs.

Second, with the same gaseous system, entangled MWCNTs can also be achieved on the stainless steel plate. The results reveal that the mechanism belongs to tip-growth model. The only catalyst we can find at the top end of MWCNT is Fe rather than any types of alloys. In addition, the degree of crystallization is much lower than that of MWCNTs from Fe-coated carbon cloth according to the observation of X-ray diffraction and Raman measurements.

4.2 Synthesis of coral-like MWCNTs

We present here the formation of coral-like carbon nanotubes on different substrates, iron-coated carbon cloth and stainless steel plate. We are going to characterize the nanomaterials and illustrate the relation between morphology and externally applied bias. We also trying to figure out which carbon nanowalls attached to would be of difference in specific surface area and what the mechanism of formation for coral-like carbon nanotube is.

4.2.1 Sample preparation and experimental procedures

The substrate chosen to deposit carbon nanomaterials (CNMs) could be carbon cloth and stainless steel. First, we used a bias-assisted MPCVD system to fabricate carbon-based materials, namely coral-like carbon nanotubes, on iron-coated carbon cloth. First, Carbon cloths (CC, TCT Co., Ltd, 1 x 1 cm^2) coated with iron as the catalyst (20 nm thickness; prepared by e-bean evaporation) served as the substrate. Prior to synthesis, the iron-coated substrates were subjected to annealing under a N_2 atmosphere at 400 °C for 5 h. After H_2 plasma pretreatment, growth of the carbon-based materials was undertaken for 30 min at a H_2-to-CH_4 ratio of 3:1, a working pressure of 10 torr, and a microwave power of 400 W without external bias. It should be noted that the two-steps procedure for the fabrication of the CNTs-CNWs electrode has been described in detail previously [174, 175, 176].

Second, Stainless-steel plates (type 316A; thickness: 0.2 mm) having an area of 1 × 1 cm^2 served as the substrates for the support of the carbon nanomaterials (CNMs). The substrates were cleaned sequentially with acetone and methanol in an ultrasonication bath, rinsed with deionized water, and then dried with nitrogen gas. Prior to deposition, plasma pre-treatment was performed in the MPCVD system at a H_2 flow rate of 40 sccm, a gas pressure of 10 torr, and a power of 300 W. The reactant gas, a mixture of CH_4 and CO_2 (3:2), was then introduced into the reaction chamber and the main growth of the CNMs was performed for 30 min. The working pressure and power were maintained at 10 torr and 300 W,

respectively. The applied bias was 0, –100, or –150 V. The substrate temperature was measured using an optical pyrometer and thermocouple placed in direct contact with the substrate holder.

The morphologies and structures of the carbon-based electrodes were investigated using a JEOL JSM 6700 scanning electron microscope (SEM) and a JEOL JEM 4000 high-resolution transmission electron microscope (HRTEM).

4.2.2 Characteristics of the coral-like MWCNTs

First, the structure obtained in the absence of an external applied bias shows a CNT decorated with CNWs on the CC substrate [Figure 4.8(a)]. It should be noted here that applying an external bias could lead to the formation of aligned CNTs, like the structure illustrated previously in section 4.1. The magnified image in Figure 4.8(b) reveals that entangling of CNTs connected with carbon nanowalls occurred throughout the substrate. The carbon nanowalls were distributed fractionally on each CNT, with an average diameter of 60 nm. Figure 4.9(a) and (b) display the early and late stages, respectively, of the growth of the CNWs; at the late stage, the CNWs increased in size and an uninterrupted tubular structure was formed clearly without the intrinsic defects visible in Figure 4.9(b). We suspect that the different structure of the CNTs-CNWs relative to that of the aligned CNTs resulted from the presence of pentagons and heptagons during the nanotube formation process; such defects tend to present dangling carbon atoms for subsequent accumulation of other carbon atoms during the growth process. Moreover, because hydrogen atoms are incorporated in situ through single bonds, they are usually present as terminating units on the front site [177]. As a result, the repulsive force between the hydrogen atoms benefits the formation of nanowall-like residues as active sites for accumulation.

Second, in general, catalyst particles are essential for the successful synthesis of structural carbon materials, especially when using CVD systems. Thus, we pretreated our

stainless-steel substrates with H_2 plasma for 10 min to provide metallic particles to act as catalysts for the growth of CNMs; from Figure 4-10 we estimate that their sizes ranged from 100 to 150 nm.

Under the plasma deposition conditions, we obtained three different kinds of CNM structures when applying three different negative bias to the substrate. Figures 4.11(a) and (b) display magnified images of the pure carbon nanowall film (CNWF) obtained at a bias of 0 V. Each CNW had a width of ca. 1 μm and a thickness of ca. 5 nm. The substrate temperature, as measured by a thermocouple placed on the back side of the substrate, was low (ca. 380 °C). The formation of a film of CNWs aligned perpendicular to the substrate surface occurs as a result of the intrinsic self-potential around surface [52].

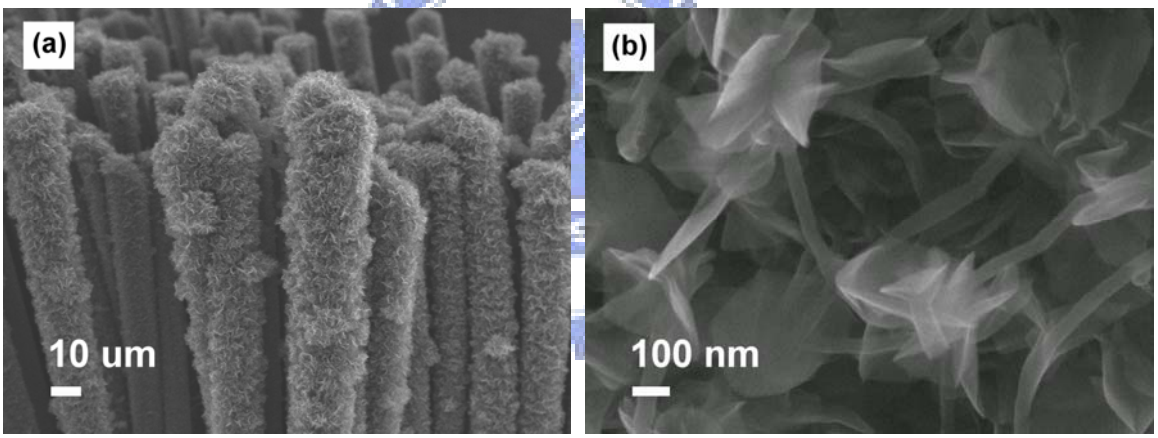

Figure 4.8 SEM images of carbon materials prepared through MPCVD for 30 min. (a) CNTs-CNFs prepared in the absence of an applied external bias; (b) magnified image of the CNTs-CNFs electrode.

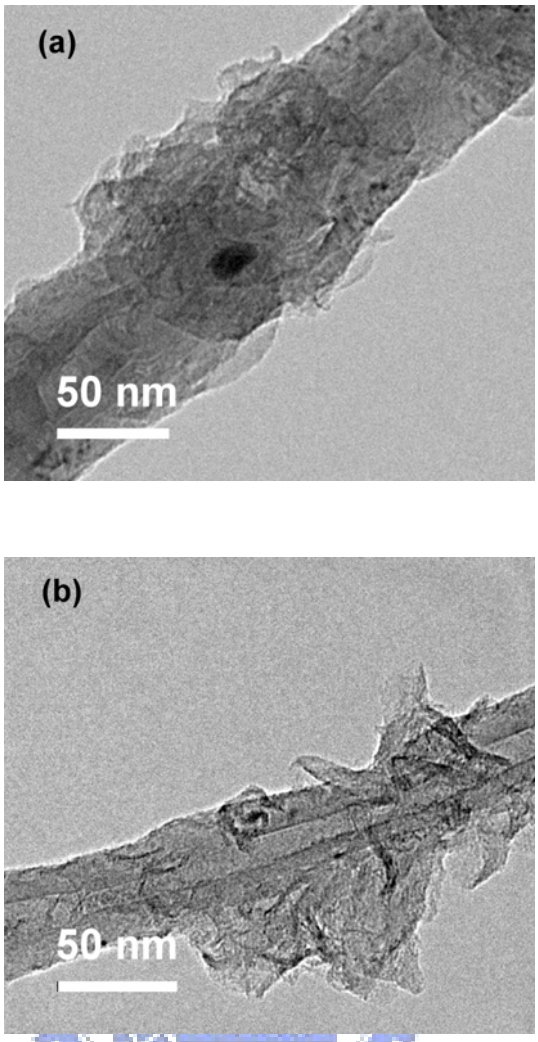

Figure 4.9 TEM images of the (b) early and (c) late stages of development of CNFs attached to a CNT.

When we applied a bias of –100 V to the substrate, carbon nanowall spheres (CNWSs) having diameters of ca. 2 μm formed on the substrate [Figure 4.11(c) and (d)]. We suspect that they arose primarily through a process of damaging, but not breaking, the surfaces of the catalyst particles (i.e., forming many defects, such as cracks) and then precipitating carbon at those sites. The mechanism follows the carbon dissociation, diffusion, and precipitation model, which describes the growth and structures of carbon materials [178, 179], providing a sphere covered radially with walls. In this model, the hydrocarbon adsorbs dissociatively to supply carbon atoms to the particle surface; the surface carbon undergoes dissociation,

diffuses through the particle along interstitial lattice planes, and precipitates from corresponding sites at opposite facets. The diffusion is driven by a concentration gradient. If the size of the metallic particle acting as the catalyst exceeds the carbon diffusion length, the process leads preferentially to the formation of CNWs to CNTs [180, 181]. Based on considerations of the surface energy, it has been suggested that anisotropic deposition occurs during the growth of pure CNWs; the self-potential established on the substrate surface causes vertical growth because the field lines are invariably terminated normal to the surface [173, 50].

When we increased external bias to –150 V, we obtained a quite different morphology: a novel structure comprising CNTs decorated by CNWs (CNTs/CNWs) [Figure 4.11(e) and (f)]. The substrate temperature was ca. 450 °C. The diameters of the CNTs decorated by nanowalls ranged from ca. 100 nm to slightly less than 1 μm. We suspect that the breaking of catalysts, caused by the bias of –150 V, was beneficial to the formation of CNTs with smaller iron particles captured inside them. By comparison to H_2/CH_4 system, introducing CO_2 dramatically reduces the growth temperature because of its effect on the ionization energy. Oxygen-containing species, such as O-H [182, 183], can effectively remove amorphous carbon and even graphitic structures from the surfaces of CNTs, especially with the assistance provided by an applied bias. We suspect that the nanotubes were attacked by the accelerated oxygen-containing ions; the resulting damaged CNT surface would exhibit many tiny substructural features presenting free carbon atoms (dangling bonds) while the CNTs remained growing. The damaged, rough surfaces of the CNTs contain many active sites for the aggregation of carbon atoms. Collisions between these aggregated carbon atoms would lead to the formation of horn-like structures that would later turn into walls of nanowalls, as predicted by molecular dynamics simulations [184]. Of course, the resulting CNWs would also be attacked during this process to leave numerous active sites for the further formation and attachment of additional CNWs. Figure 4.11(f) reveals many spots distributed on the

CNTs and CNWs. We suspect that the spots are active sites at which future CNWs would grow. Finally, the substrate is covered with interlaced CNTs presenting a nanowall morphology.

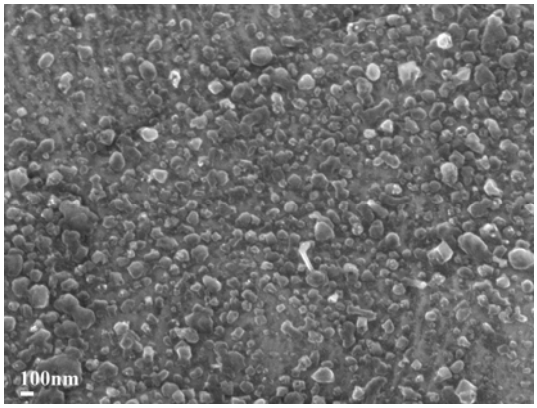

Figure 4.10 The morphology of the SS substrate pretreated by hydrogen plasma at H_2 flow of 10 sccm, power of 300 W, and pressure of 10 torr.

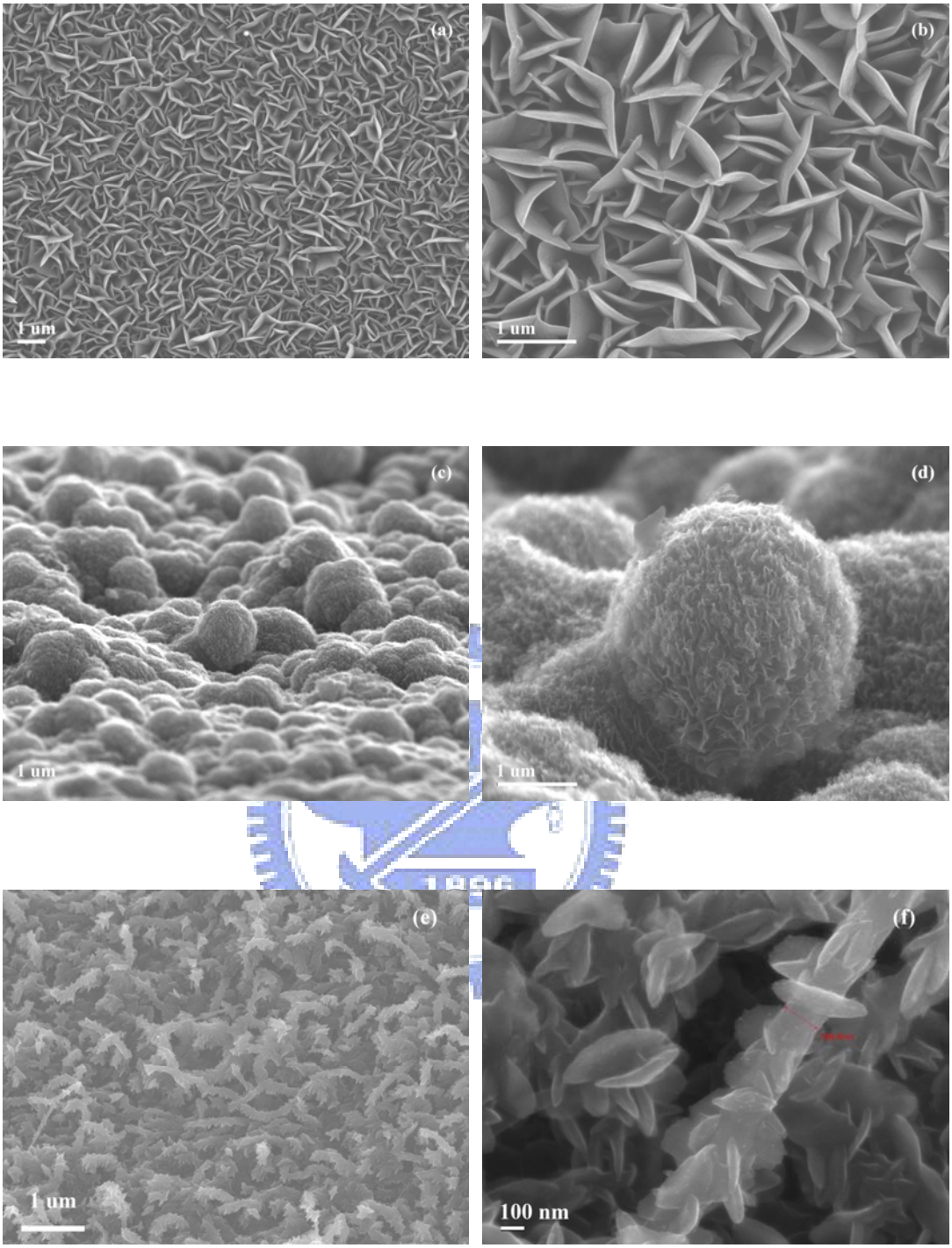

Figure 4.11 Carbon nanomaterials prepared after performing bias-assisted MPCVD for 30 min: (a, b) pure CNFFs formed in the absence of an applied external bias; (c, d) CNFSs formed at an external applied bias of –100 V; (e, f) CNTs/CNFs formed at an external applied bias of –150 V.

Figure 4.12 presents TEM images of related CNW/CNT structures. Figure 4-12(a) displays the tubular structure of a multiwall CNT that is decorated in places by nanowalls; Figure 4.12(b) provides a magnified image of the CNT wall, revealing the high degrees of graphitization on both sides. We estimate the distance between the two graphite layers to be ca. 0.35 nm, very close to the theoretical value (0.34 nm). Figure 4.12(c) displays the structure of a CNT covered entirely by CNWs, which are also attached to other nanowalls. This morphology is consistent with that determined from SEM images. Figures 4.12(d) and (e) present the top and side views, respectively, of a CNW/CNT; the both reveal graphitic structures having a thicknesses ranging from 5 to 20 nm. The enormous number of CNWs that are stacked onto the CNT in Figure 4.12(c) suggests that further continuous growth of CNWs can arise through a process of carbon deposition and collision. It is noted here that the growth mechanism belongs to the top-growth, and catalyst encapsulated at the top end of coral-like MWCNTs was detected to be of iron only as presented in Figure 4.12(f). The result between the MWCNTs synthesized in the CH_4-CO_2 and CH_4-H_2 (section 4.1.3) systems is alike.

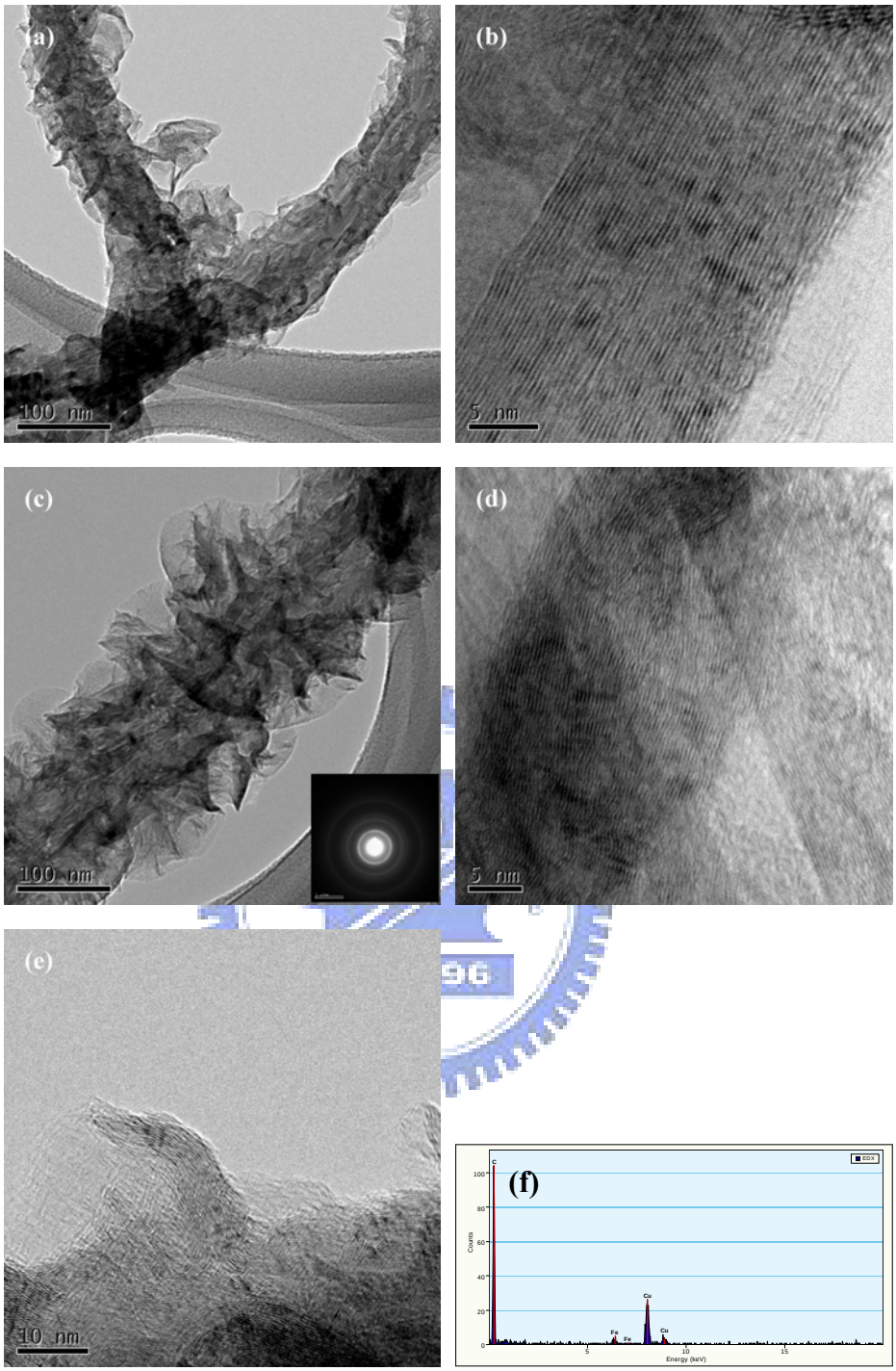

Figure 4.12 TEM images of (a) a CNT decorated with some CNFs, (b) a magnified CNT wall, (c) a CNT covered entirely by CNFs, and (d) top, (e) side views of a CNF/CNT structure and (f) the EDX measurement of the catalyst encapsulated at the end top of coral-like MWCNT.

Figures 4.13(a) and (b) display the early and late stages, respectively, of the growth of a CNW. Figure 4.13(a) reveals that the structure of the CNW was very disordered and small in size at the onset of CNW growth. This disordered CNW continues to grow through collisions of carbon atoms to form graphitic, ordered layers [Figure 4.13(b)]. Furthermore, these images suggest that the CNWs arise directly from the CNTs because of the similarity between the graphitic layer distance in the CNTs and the CNWs. Using an electron energy loss spectroscopy system mounted on the TEM equipment, we detected no elements other than carbon atoms at the CNW–CNT interface, suggesting that the attachment of CNWs to CNTs is a catalyst-free process.

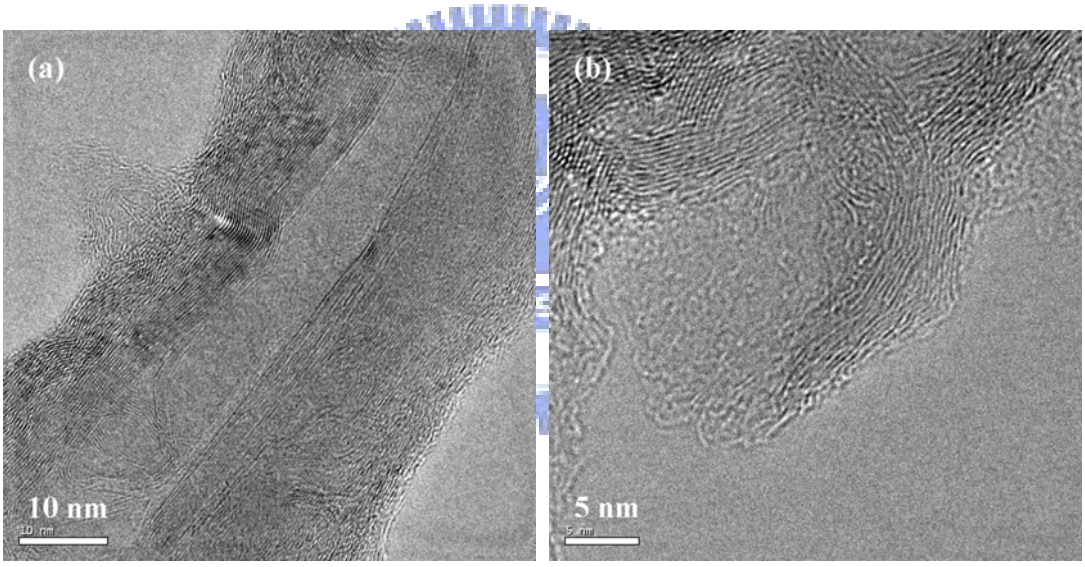

Figure 4.13 TEM images of a CNF attached to a CNT at the (a) beginning and (b) end of the formation process.

Figure 4.14 shows the Raman spectra of the coral-like CNTs synthesized on the CC and SS substrates. In all Raman spectra of the coral-like CNTs, two main bands are observed at ~1580 and ~1350 cm^{-1}, respectively. The former band corresponds to G band (after graphite), indicating E_{2g} mode of graphite [185, 186]. The later band corresponds to D band (after defect), activated by the disorder due to the finite crystallite size [185-188]. In addition, a

weak band is observed at ~1620 cm^{-1}. This band corresponds to D' band, that emerges with D band indicating the disorder [189]. The D' band appears in the graphite-like carbons with relatively low disorder such as microcrystalline graphite and glassy carbon, while it can not be observed in significantly disordered carbons such as carbon black [190].

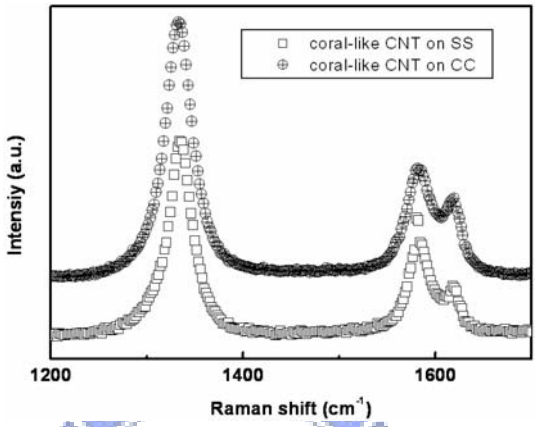

Figure 4.14 Raman shift spectra of the coral-like CNTs synthesized on the Fe-coated carbon cloth (annealing at 400 °C) and stainless steel substrates.

4.2.3 Formation mechanisms of coral-like MWCNTs

We suspect that in the plasma systems, the hydrogen atoms are usually present as terminating units on the front site. The repulsive force between two lined hydrogen atoms termination will peel the graphitic structure. The resulting damaged CNT surface, resulting from repulsive force would exhibit many tiny substructural features presenting free carbon atoms (dangling bonds). The only difference between H_2-CH_4 and CO_2-CH_4 systems is the matter of –OH, which is more beneficial for the damage of CNT surface and, of course, the CNWs. This is the reason why the distribution of CNWs in the H_2-CH_4 system is not throughout the CNTs. The damaged, rough surfaces of the CNTs contain many active sites for the aggregation of carbon atoms. We believe that the mechanism of synthesis of the CNWs can be divided into three broad parts. Initially, aggregation of carbon atoms occurs at the activated sites. Next, lateral growth of the CNWs then proceeds in preference to vertical

growth under the experimental conditions; it results from the fact that dangling bonds of a free carbon atom can be considered asymmetric, with three in-plane sp^2 bonds and a P_Z orbital that is perpendicular to this plane. This asymmetry is also an important factor for the catalytic synthesis of tubular structures. Finally, the carbon atoms are subjected to collisions to form walls, as predicted by molecular dynamics simulations [184] [Figure 4.15(a)]. As illustrated in Figure 4.15(b), the CH stretching signals depicts that the MWCNTs are indeed attached by H atoms.

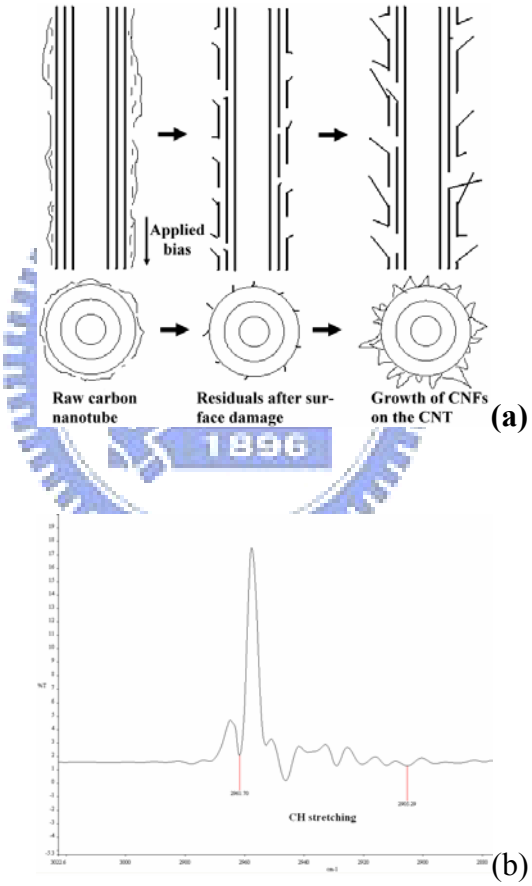

Figure 4.15 Schematic diagrams of the MWCNTs (a) decorated by CNWs through a peeling process by hydrogen termination and (b) The FTIR measurement.

4.2.4 Summary

We have used bias-assisted MPCVD to synthesize CNTs presenting graphitic nanowalls on carbon cloth and stainless steel substrates. We fabricated CNTs presenting a graphitic petal-like carbon material in one step after introducing H_2-CH_4 and CO_2-CH_4 as reactant gases. The annealing catalyst and the external bias both had significant effects on the formation of coral-like CNTs presenting nanowalls. In our studies, the influence of external bias on the formation of coral-like CNTs was different and depended on the cases. In particular, the CNTs formed in the CO_2-CH_4 could be covered throughout with CNWs owing to the assistance of oxygen-containing items. In addition, the oxygen-containing items also leads the CNWs to be fabricated on the initial CNWs attached to the CNTs. Therefore, it was suggested that the CO_2-CH_4 plasma system is beneficial for the synthesis of carbon nanowalls in a catalyst-free process of synthesis.

4.3 Synthesis of graphitic CNWs on carbon cloth

We presented here a catalyst-free fabrication of carbon nanowalls on carbon cloth in the CO_2-CH_4 plasma system. The influence of applied power on the difference of CNWs in morphology will be discussed. We are also trying to come up with the way normal two-dimensional CNWs sheet could turn to three-dimensional one. Finally, we will propose a formation mechanism of the so-called flower-like aggregation for three-dimensional carbon nanowalls electrode.

4.3.1 Catalyst-free fabrication of 2-D and quasi-3-D CNWs electrode on carbon cloth

Carbon cloth (E-tech.) having an area of 1×1 cm^2 served as the substrate for the growth of 2-dimensional CNWs during MPECVD. The substrate was first activated with hydrogen plasma at a H_2 flow rate of 40 sccm at 300 W and 10 torr for 10 min; a CO_2/CH_4 plasma was then applied at a power of 200, 300, or 400 W. The CO_2-to-CH_4 flow ratio was maintained at 2:3 and the growth process was performed at 10 torr for 30 min. For comparison, other samples were subjected to the same deposition process, but without hydrogen plasma pretreatment. The color of the material deposited at 400 W was black; the other two products were gray.

To fabricate so-called 3-dimensional CNWs, we made the as-received 2-D CNWs sheet to be oxidized by a simple way using 2M HNO_3 aqueous to activate it at 95°C for 6 hours. Afterwards, the chemically oxidized 2-D substrate underwent further growth of CNWs at the same operating parameters of synthesis.

The substrate temperature was measured using an IR thermometer (Minolta TR-630) and a thermocouple in direct contact with the substrate holder. A JEOL JSM 6700 scanning electron microscope (SEM), a JEOL JEM 4000 high-resolution transmission electron microscope (HRTEM), and a micro-Raman scattering system (Jobin Yvon Lab-RAM HR;

He-Ne laser; wavelength: 632.8 nm) were used to examine the structure of the product carbon materials. BET measurements were performed for sample in a liquid nitrogen bath at 77 K using a NOVA 1000e surface area and pore size analyzer.

4.3.2 The effect of supplied power on the formation and properties of CNWs

Figure 4.16 displays SEM images of the CNWs synthesized on the carbon cloth under various microwave powers after hydrogen plasma pretreatment. Figures 4.16(a)–(c) present images of the CNWs formed at 200 W and a relatively low substrate temperature (ca. 380 °C) for 5, 10, and 15 min, respectively. After 5 min, many tiny carbon islands were distributed uniformly on the substrate; on average, these islands were ca. 100 nm long and ca. 5 nm wide. After 10 min, the substrate was covered with structural carbon materials that evolved from the tiny islands; the CNWs were interlaced to form a carbon nest-like film. After 15 min, the CNWs all had a similar length of several micrometers and a height of ca. 1 μm. Even when operated for a longer length of time, the thickness of the film remained at 1 μm on account of lateral growth [50]. When we operated the system at 300 W for 15 min at substrate temperatures of up to 420 °C [Figure 4.16(d)], the morphology of the product was similar to that obtained at 200 W, except that it contained more stretching branches attached to the surface of the major nanowalls, such that a fraction of smaller pores existed. This phenomenon might have arisen from the presence of activated sites during the etching process in the CO_2/CH_4 plasma system. Oxygen-containing species (e.g., OH) play an important role in removing amorphous carbon and, thus, facilitate the formation of graphite structures [182]. The etching process might also have resulted in significant damage to the CNWs' surfaces to create dangling bonds of free carbon atoms as active sites for nucleation. We conclude that applying more power induces more tiny pores to form, i.e., a much smaller porous structure results. We obtained a totally different morphology [Figure 4.16(e)], however, when we applied an even greater microwave power (400 W) and relatively high substrate temperatures

(up to 480 °C) to the system. Figure 4.16(f) displays a quasi-3-D construction comprising aggregates of extremely small walls.

After 1 or 10 min of operation at 400 W, tiny CNWs aggregates were deposited uniformly [Figure 4.17(a) and 4.17(b), respectively]. The diameter of each fiber, originally 8 μm, varied from 10 to 20 μm, corresponding to Figure 4.17(a) and 4.17(b), respectively. The initial formation of the morphology at 400 W was different from initial structures formed at lower power. The growth rate was ca. 1 μm min^{-1}. Spherical aggregates formed when we operated the system for a sufficiently long time—in our case, for 30 min [Figure 4.17(c)]. Even so, magnified image of the structure depicts the same aggregation, displayed in Figure 4.17(d). A critical microwave power is required for effective ion bombardment, sputtering, and etching during plasma processing [173], such that a disordered carbon structure can be formed. Even at a high deposition rate of carbon, the reaction time might not be sufficiently high for inner, disordered carbon atoms to form continuous walls through collision, leading to restricted graphitization. Our findings suggested that, at 400 W, an enormous number of amorphous carbon atoms deposited initially, impregnated with oxygen-containing groups as active sites, which then gradually transformed into CNW structures through aggregation and interior collision processes. The CNWs that we prepared in this study (20–30 nm long and 3–5 nm wide) are much smaller than those which have been limited as a 2-D material [191, 181]. Most interestingly, the quasi-3-D clusters prepared at 400 W had an average pore size of 10.7 nm and an appreciably greater surface area (728.6 m^2/g) than those prepared at 300 W (363.6 m^2/g) or 200 W (331.3 m^2/g). With respect to the structure formed at 200 W, the slightly increased surface area formed at 300 W resulted from the presence of stretching branches, consistent with our SEM observations. For comparison, the surface area of the unmodified carbon cloth was 119.5 m^2/g.

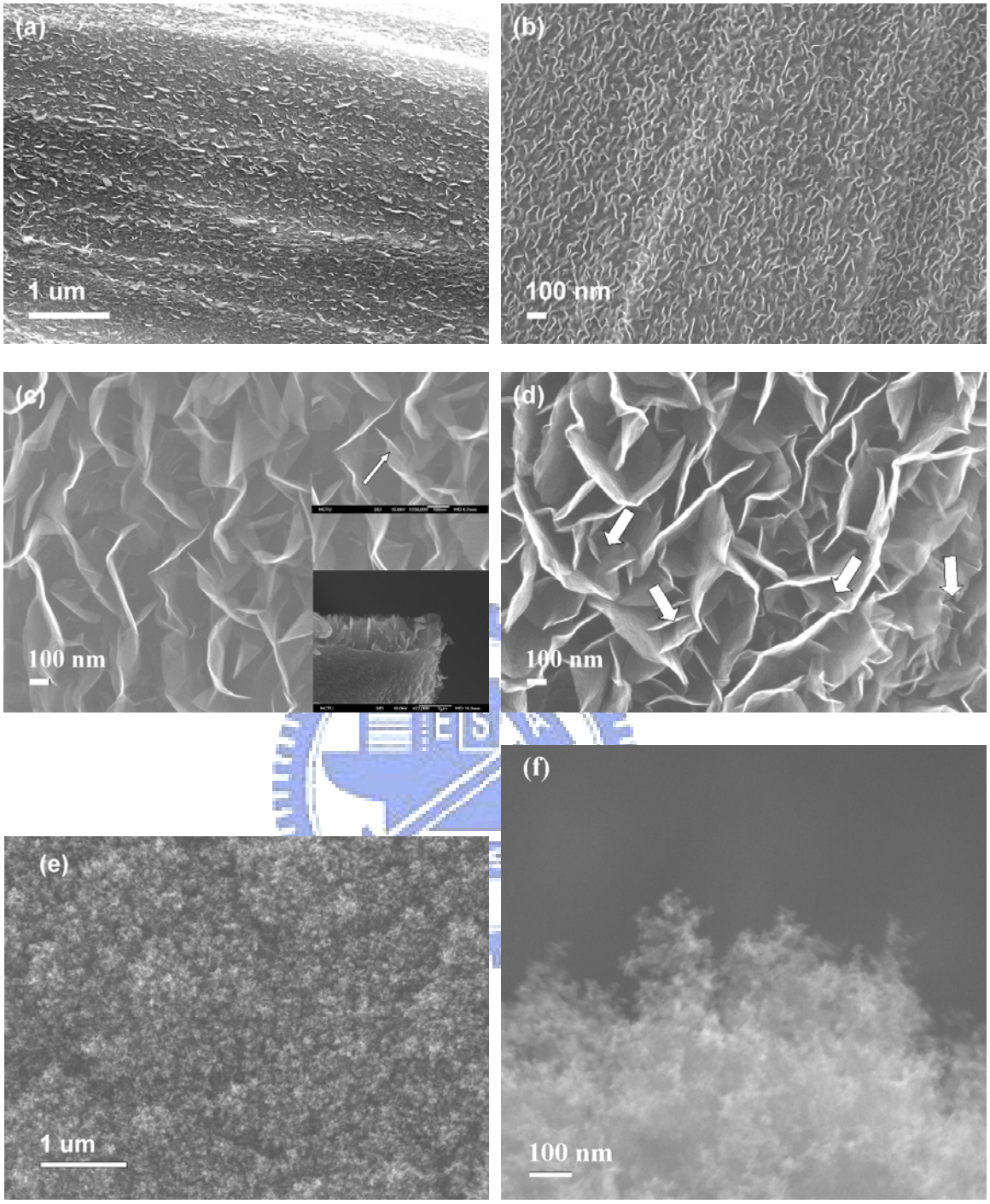

Figure 4.16 SEM images of (a) the flake-like carbon seeds synthesized on the carbon cloth for 5 min, and (b) deposition for 10 min and (c) for 15 min at 200 W; (d) at 300 W for 15 min; (e) at 400 W for 15 min and the inset of high-magnification image of tiny CNWs aggregation; (f) the quasi-3-D configuration of 400 W, with the H_2 plasma pretreatment.

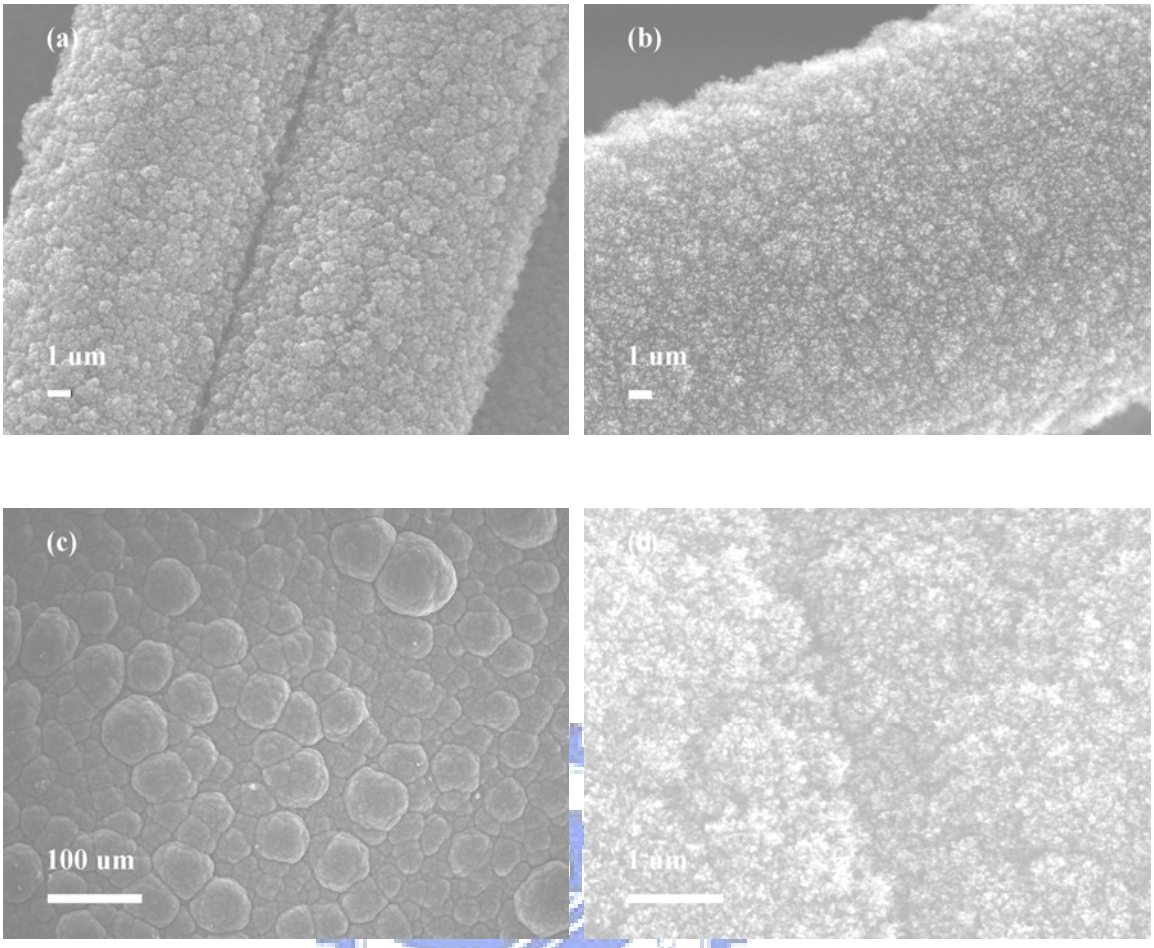

Figure 4.17 SEM images of the deposition at 400 W (a) for 1 minute, (b) for 10 minutes, (c) for 30 minutes, and (d) the magnified image of the gathered structure in Figure 2(c).

Figure 4.18 displays TEM images corresponding to the SEM images in Figure 4.16. The thickness of each nanowall was less than 5 nm. In contrast to the sample obtained at 400 W [Figure 4.18(c)], which contained a greater amount of amorphous carbon, Figures 4.18(a) and 4.18(b) reveal that continuous and ordered graphite layer structures formed at 200 and 300 W, respectively. In addition, a great curvature was present in the sample prepared at 200 W, as is evident in the inset to Figure 4.18(a). The distance between pairs of graphitic planes in the nanowalls was ca. 0.34 nm, which is consistent with that reported by Lin et al. [192]. When we applied a much higher microwave power of 500 W, we obtained an amorphous carbon film as a result of the intense impact of the bombarding and etching processes.

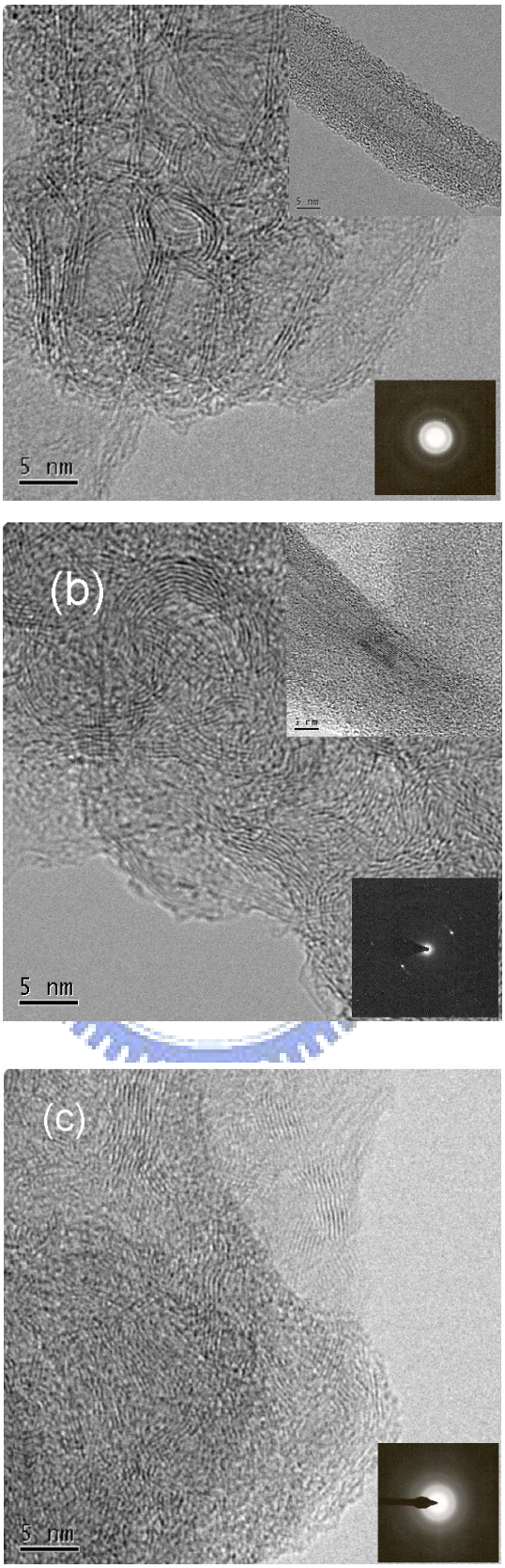

Figure 4.18 TEM images of (a) the carbon nanoflakes for 200 W, (b) for 300 W, and (c) for 400 W, with the H_2 plasma pretreatment

For the samples prepared without hydrogen pretreatment, Figure 4.19 reveals that their structures were similar to those in Figure 4.16. The major difference between these morphologies appeared at the beginning of the deposition process. Hydrogen pretreatment was more beneficial for forming uniformly active sites, leading to facile nucleation of carbon atoms for further synthesizing CNWs. There was a tendency to form non-crystalline structures in the absence of hydrogen pretreatment. A distinguishable difference between the images in Figures 4.16(d) and 4.19(d) is that the morphology of the sample prepared at 300 W in the absence of hydrogen pretreatment exhibits features similar to those of the sample formed at 400 W after hydrogen pretreatment. This finding suggests that the initial stage at which the carbon atoms nucleate as seeds is crucial to the resulting morphologies and structures. We recorded micro-Raman spectra to investigate this phenomenon.

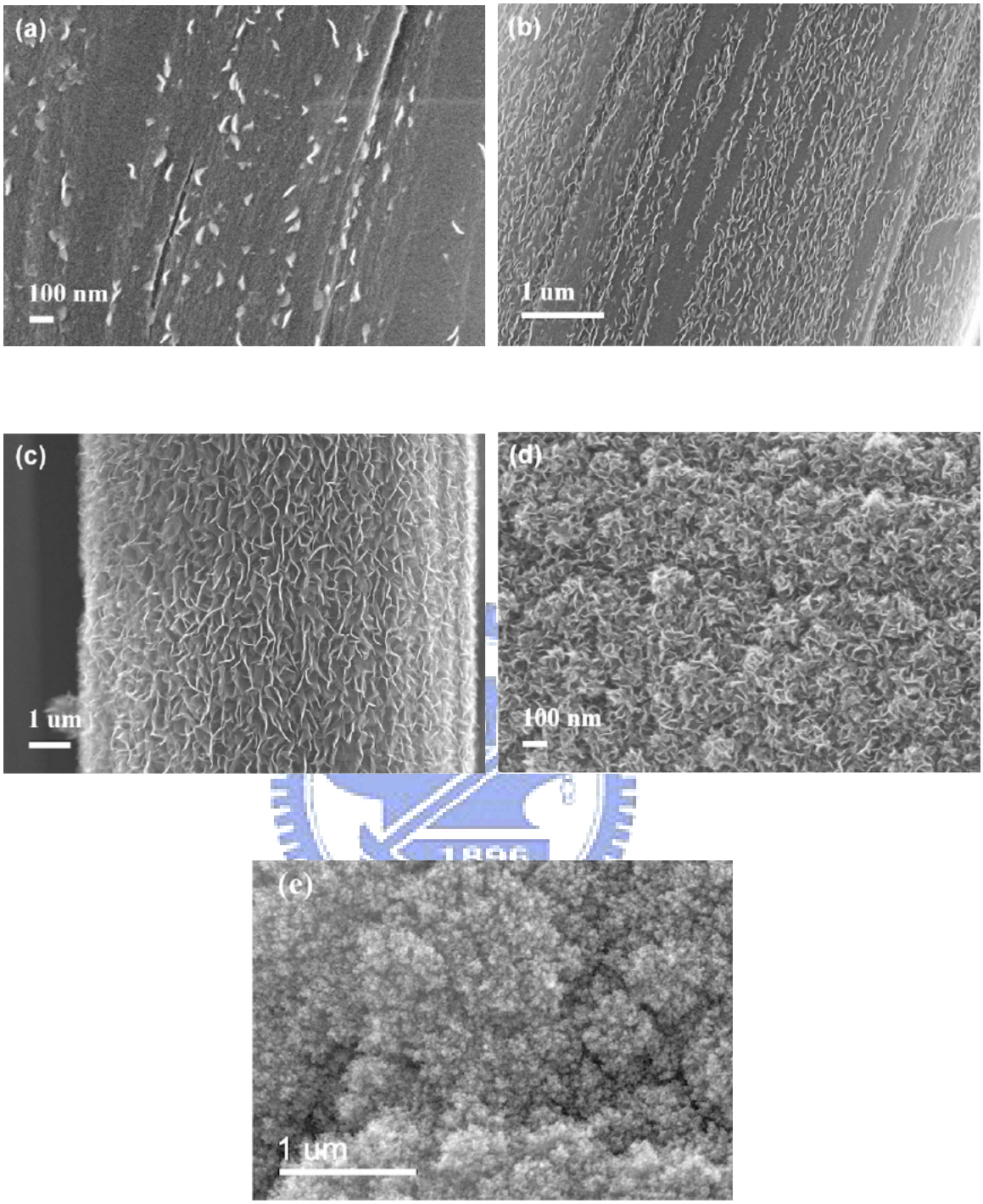

Figure 4.19 SEM images of (a) the flake-like carbon seeds synthesized on the carbon cloth for 5 min, and (b) deposition for 10 min and (c) for 15 min at 200 W; (d) for 15 min at 300 W; (e) for 15 min at 400 W, without the H_2 plasma pretreatment.

Figure 4.20 displays Raman spectra of the samples in the region 1200–1700 cm^{-1}. The results of samples with and without H-plasma pretreatment were displayed in Figure 4.20(a) and (b), respectively. We observe three distinct peaks: a typical graphite vibration mode G-band at 1580 cm^{-1}, a disordered carbon mode D-band at 1348 cm^{-1}, and a D′ line at 1620 cm^{-1}. The peak at 1580 cm^{-1} indicates that graphite structures were fabricated during growth; the peak at 1348 cm^{-1} resulted from defects in the curved graphite sheets, tube ends, and surviving impurities; the weak peak at 1620 cm^{-1} corresponds to a maximum in the density of states of the mid-zone phonon and also reveals a disorder-induced behavior similar to that of the signal at 1348 cm^{-1}. We suggest that the D and D′ lines resulted from disorder-induced features caused by lattice distortion [193].

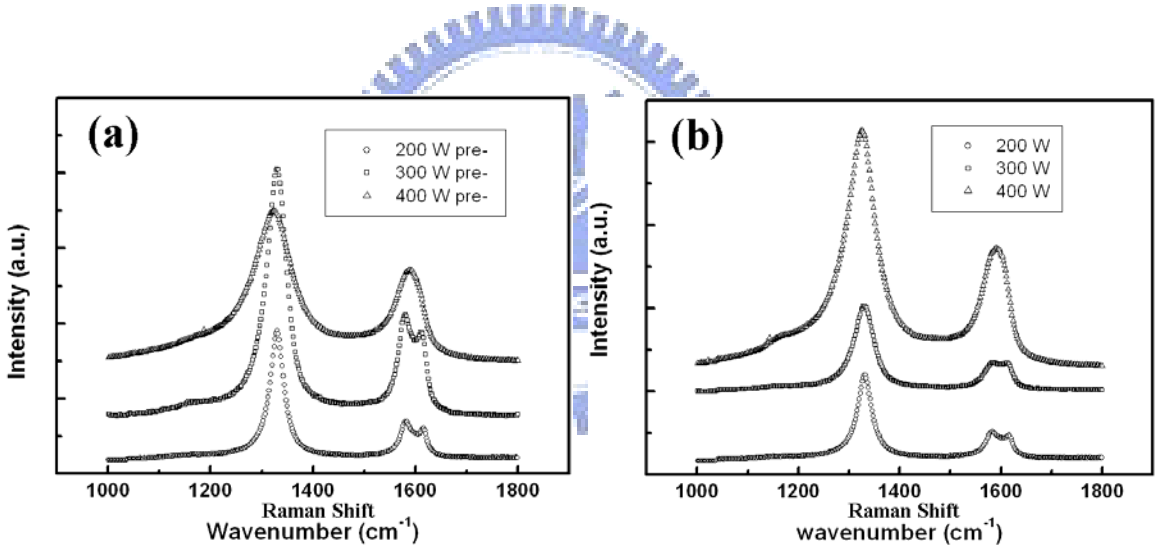

Figure 4.20 The Raman measurement of (a) the carbon nanoflakes deposited at 200 W, 300 W, and 400 W with the H_2 plasma pretreatment, and (b) without the H_2 plasma pretreatment.

Figure 4.21 presents the ratio of the D band integrating intensity (I_D) to the G band integrating intensity (I_G) plotted with respect to the applied microwave power. The value of I_D/I_G was always greater than 2.0 because of the presence of defects (e.g., distortion, vacancies, and strain) in the graphite networks and to the more nanocrystalline structure,

especially for the growth process performed without catalyst. A recent Raman study revealed that higher values of I_D/I_G correspond to smaller grains [61]; this behavior is consistent with our TEM observation. We found that the value of I_D/I_G increased upon increasing the microwave power. This result is consistent with crystalline structures forming more readily at lower microwave powers. In addition, the values of I_D/I_G for the samples prepared after hydrogen plasma pretreatment were all less than those of the corresponding samples prepared without pretreatment. This behavior is consistent with the differences observed in the SEM images in Figures 4.16(d) and 4.19(d). We suggest that a higher value of I_D/I_G is associated with the absence of carbon seeds at the onset of the fabrication process. Based on the influence of its functional groups, the carbon cloth tends to be covered initially with amorphous carbon and then active sites containing functional groups such as C-OH and C=O are incorporated onto the surface [194]. These groups help to gather carbon atoms to form so-called carbon seeds for the aggregation of carbon atoms. Therefore, the measured crystallinity would decrease as a result of the contribution from the amorphous carbon.

The dependence of surface area (S_{area}) on pore size was discussed and listed in Table 4.1. The surface area was increased with the increasing of power supply and highly correlated with the performance of pore size. The quasi- 3-D construction with smaller pore size refers to a tremendous increasing of surface area. In other words, the transformation of 2-D to quasi-3-D is more suitable for applications being eager for high surface area. In particular, the surface area would be enormously going to increase while the pore size approaches to ca. 3.7 nm, which fills in the theoretical range of mesoporous ranging from 3 nm to 5 nm. The average of the pore size is more suitable for the penetration of ions, leading to the diminishing of interior resistance, and get a high degree of ion adsorption. Such details will be discussed in section 4.3.3.

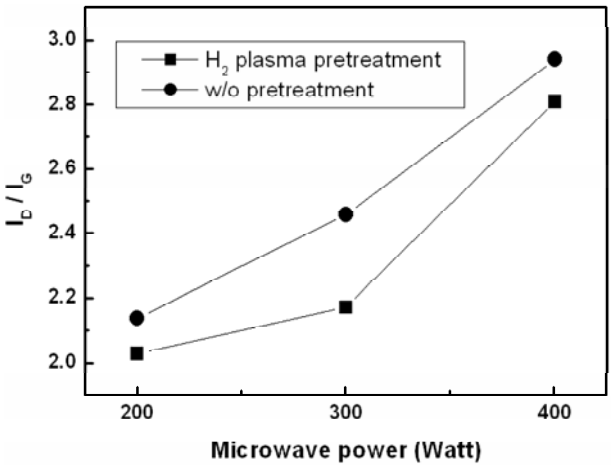

Figure 4.21 The plots of the fraction I_D/I_D versus the applied power. ■ refers to the results with the H_2 plasma pretreatment, and ▲ without the H_2 plasma pretreatment.

Table 4.1 The quantitative properties of the CNWs electrodes synthesize at different power.

H_2 plasma pretreatment			
Electrode	**S_{area} (m^2/g)**	**Pore size (nm)**	**I_D/I_G**
200W	**331.3**	**12.2**	**2.02**
300W	**363.6**	**11.7**	**2.13**
400W	**728.6**	**~10**	**2.82**
Stacking 3-D	**1577.8**	**~3.7**	**2.76**

4.3.3 Fabrication and characteristics of stacking 3-D CNWs

In the past, CNWs structures were broadly studied and mostly dedicated on a two-dimensional arrangement, which is highly restricted by fabricating system. Except for field emission, it shows restrictions on other use. Alfred et al. tried first to realize a three-dimensional (3-D) structure of CNWs, which is achievable by utilizing microwave plasma CVD (MPCVD) as the growth system [195]. However, the 3-D structures grew up only on certain edges of the electrode. Here, we report for the first time catalyst-free

fabrication of double-layered CNWs introducing CH_4 and CO_2 gases as the precursors by MPCVD.

Figure 4.22(a) shows the SEM image of as-grown carbon nanowalls sheet, named the first layer CNW. This growth belongs to a catalyst-free process, operated at power of 300 W, gas flow ratio of CH_4/CO_2= 3/2, and pressure of 10 Torr for 30 minutes on the hydrogen-pretreatment carbon cloth (E-tech, 1 X 1 cm^2) at power 300 W, H_2 gas flow of 40 seem, and the same pressure lasting for 10 minutes. With reference to the H_2-pretreatment, it could generate activated sites containing dangling bonds as the initial sites for further aggregation of carbon atoms. These carbon atoms then rearranged through collision effect to form a structural construction [184]. In addition, it has been evident that the vertical growth is highly consistent with the self-potential generated intrinsically near the substrate surface in the plasma system [173]. According to the limitation of intrinsic electric field strength across the sheath region, thickness of the first layer of CNWs was limited to be around several micrometers, generally less than 3μm. In this study, it was estimated to be up to 2 μm. We examined N_2 adsorption at 77K to determine the pore structure of the as-received CNWs [Figure 4.22(a)]. The N_2 adsorption/desorption isotherm is defined as type II and shows that the specific surface area is 331.3 m^2/g, accompanying the contribution of carbon cloth, with a pore volume size of about 12.2 nm. The value of the surface area did not exhibit fairly superior position in comparison with common experiments utilizing CNTs as electrode materials. These restrictions mentioned above apparently hindered other applications on green energies such as fuel cells, supercapacitors, and so on, despite such structure was considered as a good support of catalyst in fuel cells on account of it porous structure [174, 196]. Therefore, a simple way was come up with to efficiently improve the surface area and the weakness of restricted 2-D construction. We made the as-received 2-D CNWs sheet to be oxidized by a simple way using 2M HNO_3 aqueous to activate it at 95°C for 6 hours. As it was known that in a catalyst-free process the plasma-produced CNWs contained many

defects-disordered and nanocrystalline structures, displayed in a corrugated way, the corrugation implied high stress accommodated in interior regions, especially at the top end of CNWs with just 1~3 graphite layers. So, the areas with high stress were easily damaged through the activation method to left activated sites conjugated by functional groups, like $-O^-$ or $-COO^-$. Afterwards, the chemically oxidized substrate underwent further growth of CNWs at the same operating parameters of synthesis. The functional groups benefits the accumulation of carbon atoms so that the deposition was rapidly performed on the treated substrate, as shown in Figure 4.22(b), which was measured to be around 2 minutes of thickness. Specifically carbon aggregations preferred showing on the flimsy top edges to the sidewalls of CNWs because of the existence of functional groups. This is highly consistent with the thinking of the stress correlating with degrees of damage. However, investigation of construction of these carbon aggregations at the early stage is still not understood. It was found that the deposition carried out for 30 minutes depicted a totally different morphology in comparison with Figure 4.22(a). It showed a full coverage on the as-received electrode in Figure 4.22(c), presenting an average diameter of about 46 μm. The diameter of single carbon cloth fiber is about 6 μm, so that the growth rate of second layer CNFs was calculated to be about 0.6 μm per minute. The BET measurement carried out at 77K showed a remarkable surface area of 1577.8 m^2/g, contributed additionally by the carbon cloth and as-grown first layer CNWs, which is comparable to most activated carbons [197], and the average pore size was examined to be about 3.7 nm. The result was directly reflected on the observation of high-magnification microscopy as shown in Figure 4.22(d). Analysis of the pore size distribution revealed (Figure 4.22(e)) that the major pore size (ca. 45% content) was 3 nm. Note that in this Figure, pore sizes larger than 6 nm, which comprised only a small amount of the population, have been combined into the column labeled “6 nm”; we suspect that these pores are actually interstitial spaces between the tiny flower-like flakes, which we believe are the smallest ever to have been reported. The lateral size (width) was less than 50 nm, and

most of them were about 10-30 nm; the sickness of CNWs was evaluated to be less than 5 nm on average, comprising 7~10 graphitic layers. The physical characteristics of second layer CNWs was fairly close to that of oxidized SWNHs [198]. This reveals that the unique structure might also have the potential on the energy storage applications. For further investigation of the flower-like nanowalls aggregations, TEM images showed the irregular arrangement and short-range graphite structure in Figure 4.23(a) and 4.23(b), respectively.

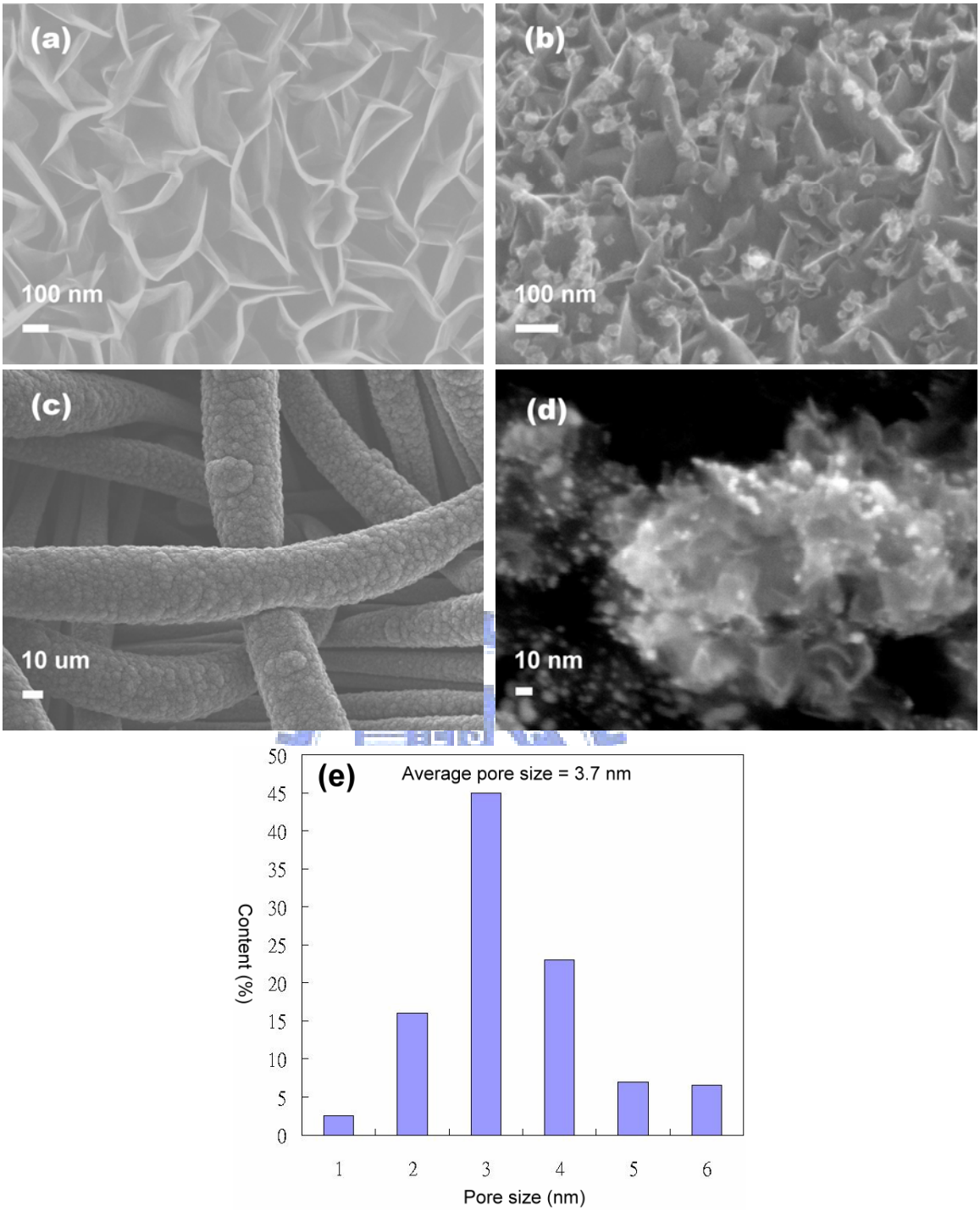

Figure 4.22 (a, b) SEM images of (a) the monolayer CNW film and (b) the double-layer CNWs at an early stage of deposition. (c) Low and (d) high magnification SEM images of the double-layer CNWs covering the as-grown CNW film, which was itself synthesized through MPCVD on carbon cloth (power: 300 W). (e) Pore size distribution of the double-layer electrode.

The mechanism of the synthesis of the CNWs from carbon cloth can be divided broadly into three parts. First, aggregation of the carbon atoms occurs at the activated sites. Lateral growth of the CNWs then proceeds—in preference to vertical growth—under the reaction conditions; this phenomenon results from the fact that the dangling bonds of a free carbon atom can be considered as asymmetric, with three in-plane sp^2 bonds and a P_Z orbital aligned perpendicular to this plane (this asymmetry is also an important factor for the catalytic synthesis of tubular structures). Finally, the carbon atoms are subjected to collisions to form walls, as predicted by molecular dynamics simulations [184]. In addition, defects such as pentagons and heptagons may have led not only to the curved structures but also to the nanoflake branches because they could also serve as initiation sites for damage of the surface—a process that occurs commonly during the fabrication of CNTs. The only difference we can tell between the first- and second-layer CNWs is their arrangement, implying a slight difference in their respective growth mechanisms. The arrangement of the first-layer CNWs clearly correlated with the existence of a self-potential on the substrate surface, as we have illustrated previously. When treated with HNO_3, however, the functional groups attached to the edges of the CNWs are subjected to repulsive forces, thereby forming individual active sites for the subsequent deposition of amorphous carbon—a process that is no longer affected by the self-potential, which exists only on the substrate's surface. The resulting formation of CNWs is, therefore, dependent on the high-rate deposition of amorphous carbon and on the etching caused by oxygen-containing species, which produce additional active sites. The presence of CO_2 aided the decomposition of CH_4 and was beneficial for the creation of oxygen-containing species. In addition, we suspect that the deposition rate of amorphous carbon was so high that the aggregated carbon atoms had insufficient time to form large CNWs. Therefore, a combination of three processes—collision, deposition of a large amount of amorphous carbon, and etching—presumably led to the construction of the 3D CNWs with short-range crystalline structure.

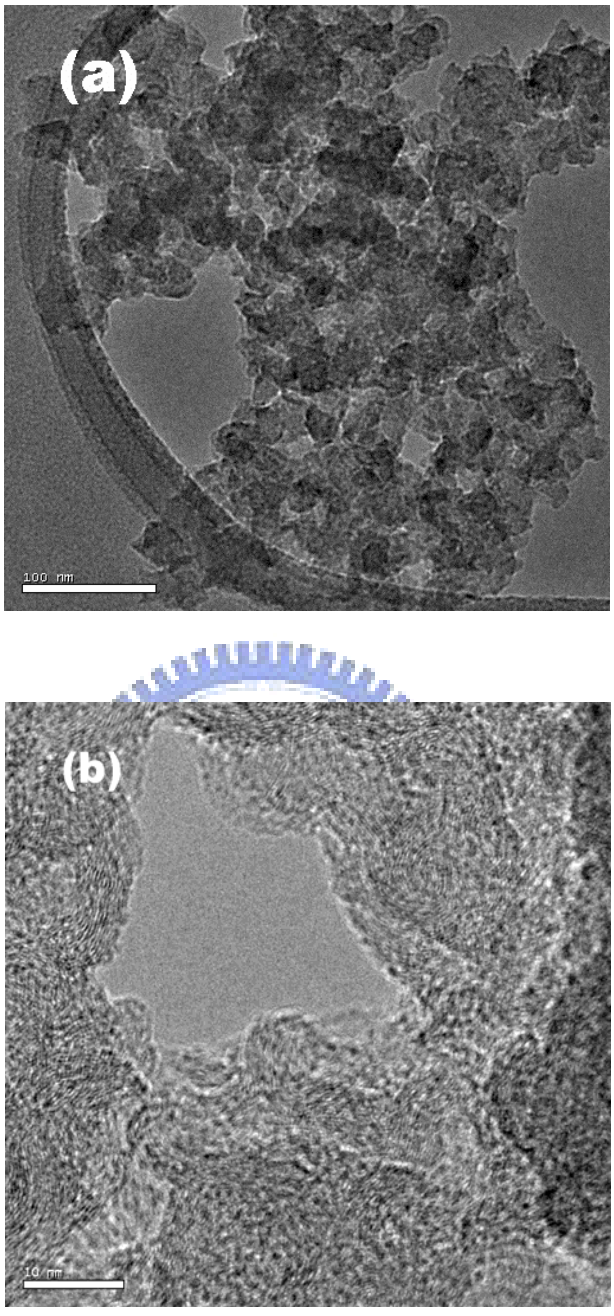

Figure 4.23 TEM images of the flower-like CNWs: (a) low magnification of flower-like CNWs, and (b) graphite structure of the smallest CNWs.

4.3.4 Formation mechanism of the stacking 3-D CNWs

The formation of flower-like aggregation of CNWs was achieved in the competition of etching and precipitation (collision) processes. The high depositions rate is due to the C_2 radical, known as the species to facilitate the formation of amorphous or graphite carbon [199], and the etching process is mainly caused by the OH radical or atomic oxygen obtained in the specific ratio of CH_4-CO_2 gas mixture plasma [184]. Based on these considerations, more activated sites owing to the etching would perform isotropically during the formation of nanowalls, and then the CNWs flowers would show up continuously. We suspect that the separation of flower-like aggregations or interior CNWs might result from the repulsive effect, caused by the hydrogenation at end sites of carbon atoms. The process of forming CNWs flowers was schematically performed in Figure 4.24.

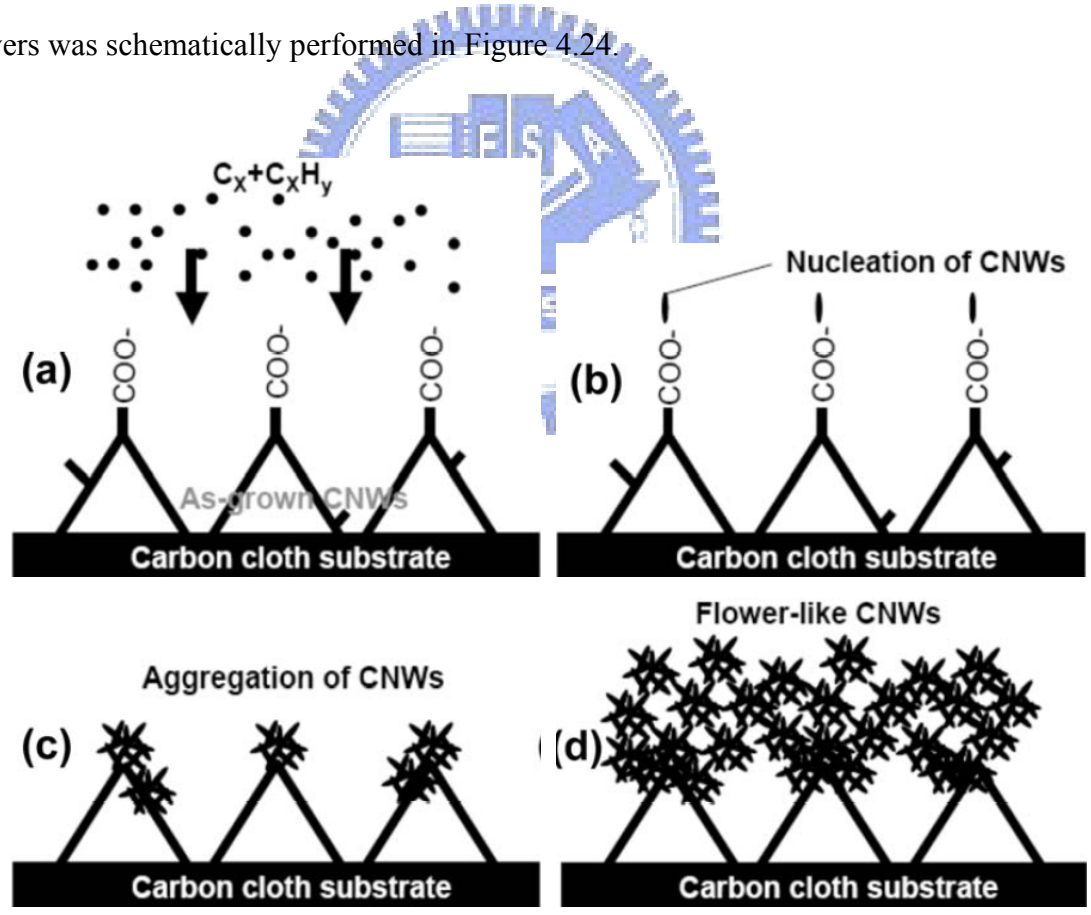

Figure 4.24 Schematic diagrams of the formation of double-layer CNWs structure: (a) Deposition of carbon atoms on the first 2D-CNWs layer; (b) nucleation; (c) aggregation of tiny CNWs; (d) formation of flower-like CNWs.

4.3.5 Summary

We have used MPECVD at a low substrate temperature in a CO_2/CH_4 plasma system to fabricate 2-D and 3-D CNF structures. Because our fabrication technique is a catalyst-free process, the resulting materials do not require a purification prior to use. The applied microwave power had crucial influence on the degree of crystallization of the products. Microscopy and micro-Raman spectroscopic measurements revealed that highly ordered graphite structures were readily obtained at low power (200–300 W). The specific surface area of the 3-D structure was almost double that of the 2-D structures because the 3-D structure comprised an aggregate of many flower-like nanowalls and, thereby, possessed a microporous structure. We suspect that our 3-D CNF aggregate—prepared through a catalyst-free, low-temperature, highly efficient fabrication process—might have commercial applicability for use in energy storage systems because of its high surface area and porous structure.

In addition, we think that the transformation of monolayer to double-layer construction, attributed to the assistance of oxygen functions, open the window of CNW materials to energy storage systems. We also expect that the construction can be designed by controlling the surface modification to possessing multi-layer stacking type for other applications in the future.

Chapter5 Electrochemical properties of carbon nanomaterials

5.1 Chemical treatment on carbon nanomaterials

5.1.1 Experimental procedures for acid treatment

In order to enhance the performance of CNMs, several methods were proposed, such as: (1) chemical activation with KOH, H2SO4, or HNO3 to increase the micropores of CNMs [200, 201]; (2) oxidation in air [202]; (3) formation of CNM-conducting polymers composites [203-205]; (4) introduction of transition metal oxides into CNMs [206- 208]; (5) electrochemical oxidation of CNMs [209]. In this study, we chose aligned MWCNTs as the electrode material and nitric acid as the oxidant to modify the surface of CNMs to be hydrophilic and functionalized. Afterwards, we were going to identify the quantity of active sites on the CNMs surface. Following the way of being applied to fuel cells was considered. The loading quantity of Pt particles could be seemed as to be equal to the amount of active sites. We are going to figure out what parameters of the chemical treatment would greatly enhance the density of surface functional groups for pseudocapacitance.

For electrochemically oxidization, carbon nanomaterial (CNM) electrodes were treated with 2M and 14M HNO_3 at 90℃ for different periods of time (0~48 hr). Then it was flushed with deionized water repeatedly and purged with N_2 for 10 minutes.

For the deposition of Pt, the prepared electrodes were immersed in a mixture solution, which comprise H_2PtCl_6·6H2O, PVP-4000 and ethylene glycol, diluted with acetone. PVP is a protection substituted to limit the particle growth-spacing. $H_2PtCl_6 \cdot 6H_2O$ was used as the precursor of Pt deposition. It was operated at 160^0C for 3hr, followed by filtration with acetone and sintered at 250^0C for 1 hr. The functional groups on the surface of oxidized MWNTs can be determined by FTIR on PROTEGE 460 series

5.1.2 Characteristics

The TEM image of Figure 5.1(a) shows the hollow structure of the MWCNT with amorphous carbon on the outer surface and with crystalline layers of the sidewall.

After the modification with HNO_3 solution, MWNTs-electrode became higher in porosity and severely damaged by the residue of amorphous carbon [209], as shown in Figure 5.1(b). It shows the opening at the end of the MWNTs-electrode. Such an observation is useful in illustrating the existence of functional groups and larger available surface area [209].

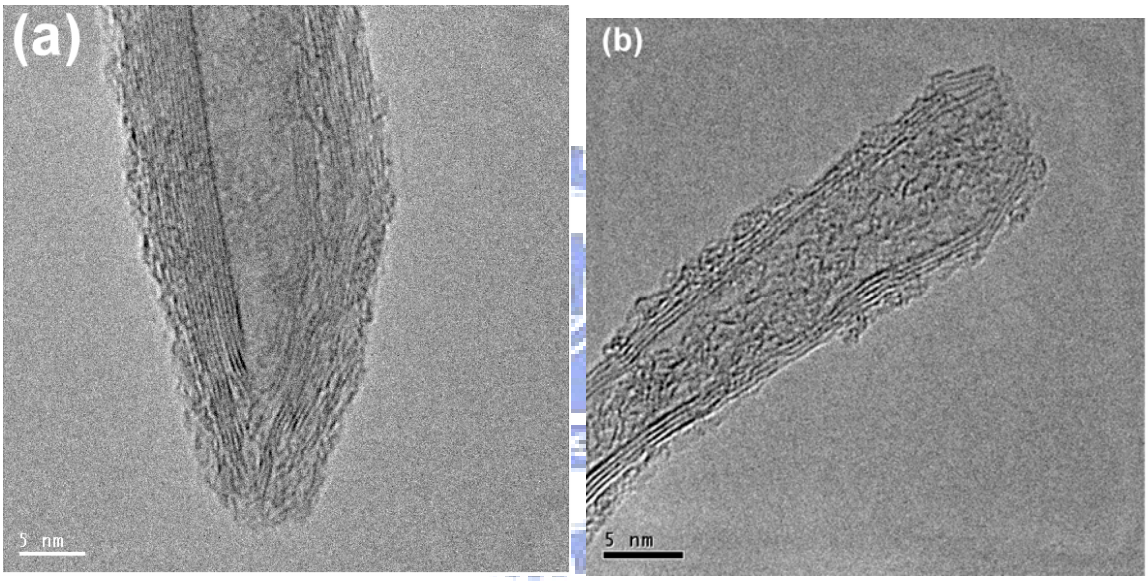

Figure 5.1 TEM images of the MWNTs, synthesized by MPECVD, showed (a) before and (b) after the chemical oxidation (HNO_3, 14M).

5.1.2.1 FTIR and XPS measurements

The surface features can be demonstrated by FTIR (Figure 5.2) and XPS (Figure 5.3) measurements. As shown in Figure 5.2(a) and 2(b), broad intensive bands are assigned to the tertiary (-OH) or the carboxylic acids (-COOH) at 1375 cm^{-1} and to the carboxylic acids (-COOH) at 1574 cm^{-1} [210]. The carboxyl groups can also be detected by XPS shown in Figure 5.3. The C 1s spectrum is composed of C=C (~284.6 eV), C-C (~285.85 eV), CO (287.46 eV), COO-(289.24 eV) and OCOO- (~291.5 eV) functional groups [211]. The

observed shift following the chemical treatment is about 1 eV. Thus, the results mentioned above revealed that MWNTs merely forms tertiary alcohol (-OH) and the carboxylic acids (-COOH) by HNO_3-treatment at 90^0C.

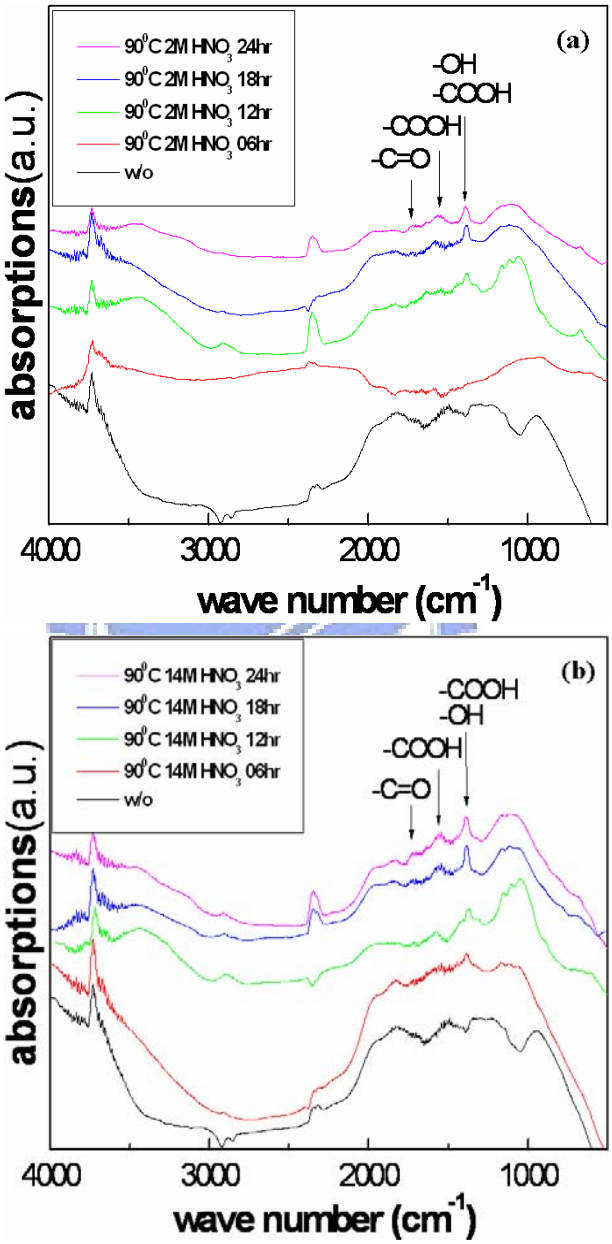

Figure 5.2 Infrared spectra of the electrodes treated in various periods of time (0 hr. ~ 24 hr.) by (a) 2M and (b) 14M HNO_3.

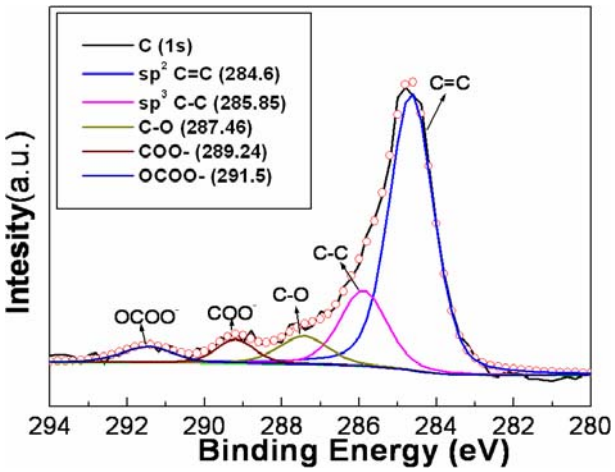

Figure 5.3 C 1s spectrum of the HNO_3-MWNTs oxidized chemically at 90℃ for 6hr (14M).

5.1.2.2 Deposition of Pt on the MWCNTs

The procedure of PVP-protected Pt nanoparticles synthesized in ethylene glycol was presented so that the H_2PtCl_6 can be completely reduced at the temperature of 160^0C, explained by the equations (5.1) and (5.2).

$$Pt^{4+}_{(aq)} + 6Cl^{-}_{(aq)} + 2H^{+}_{(aq)} \; <=> \; H_2PtCl_{6\,(aq)} \qquad (5.1)$$

$$H_2PtCl_{6(aq)} + CH_2OHCH_2OH_{(aq)} \; <=> \; Pt^0 + 6HCl_{(aq)} + 2HCHO_{(aq)} \qquad (5.2)$$

The Pt^{4+} ion reduced to Pt^0 atoms [212] can be identified by the observation of strong Pt_{4f} peak of the XPS measurement as shown in Figure 5.4.

Figure 5.5(a) shows that the aggregation of Pt nanoparticles is larger in size than that of Figure 5.5(b) corresponding to the HNO_3-MWNTs electrode. Furthermore, the particle size corresponding to the HNO_3-MWNTs is in a smaller distribution. In addition, both electrodes depict that the Pt nanoparticles could arise uniformly on the integrated MWNTs electrode. It concludes that the nanoparticle size of Pt on the HNO_3-MWNTs has no distinct difference

with regards to the increase of Pt wt%. We suggested that these findings arise as a result of the exclusion of adjacent functional groups.

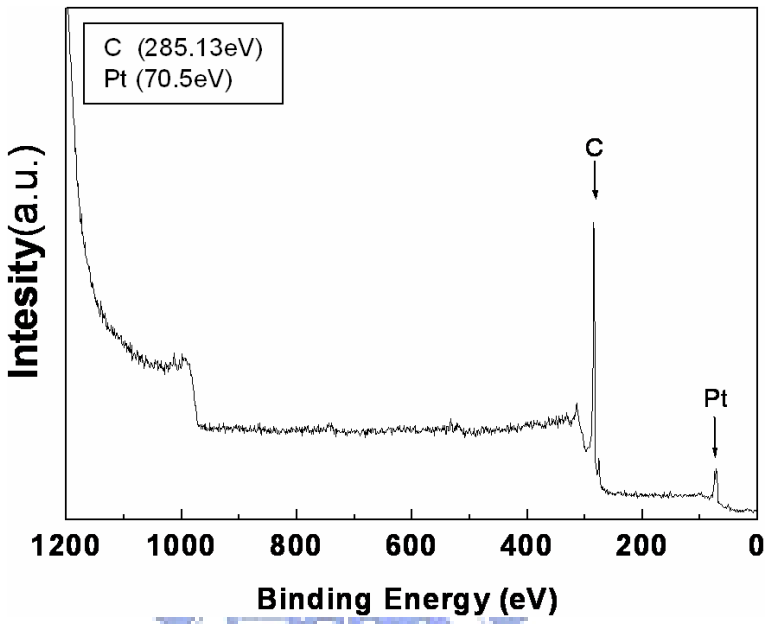

Figure 5.4 The observation of strong Pt_{4f} peak of the XPS measurement.

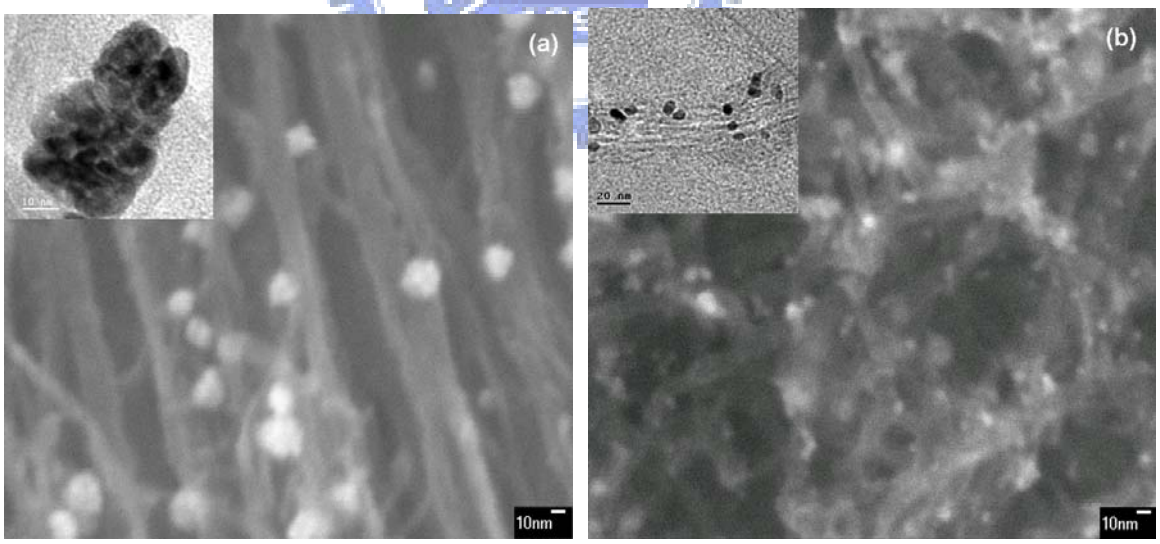

Figure 5.5 SEM images; (a) Pt nanoparticles on raw-MWNTs are agglomerated to be a larger nanoparticle and (b) Pt nanoparticles disperse uniformly on HNO_3-MWNTs.

5.1.2.3 Quantitative limitation of active sites on carbon material

Figure 5.6 shows the function of Pt quantity as periods of chemical oxidation. The loading of Pt on MWNTs with reference to carbon can be estimated to be 14.37 / 16.72 / 24.38 / 28.21 / 26.99 wt% and 5.38 / 26.52 / 27.94 / 25.79 / 25.95 wt%, corresponding to the chemical modification of 2M and 14M HNO_3, respectively. A trend appears and shows that the quantity of Pt increases and reaches the stabilization. It reveals that relatively large quantity of Pt could be obtained after 12 hr and 6hr for 2M HNO_3-MWNTs and 14M HNO_3-MWNTs, respectively, as shown in Figure 5.6(a) and (b). It also shows the results of Pt active surface area of these two electrodes. This demonstrates that the treatment can be adopted to effectively express the quantitative limitation of active site It could be concluded that due to the repulsive force between functional groups, the quantity of active site reaches the maximum after a specific period of time, depending on the cases. In theory, the fraction of occupation by functional groups could approach a maximum value of ½ due to the simple expression of Eq. (5.3) as follows:

$$y/(1-y) = K \exp(VF/RT) \quad (5.3)$$

The quantity y can be an extent of fractional coverage θ of an electrode surface (generated by the charge required for deposition of adatoms), an extent of fractional absorption, X, into some intercalation host (e.g., TiS_2 or CoO_2 accommodating Li), or third, some extent of conservation of an oxidized species to a reduced species (or vice versa) in a redox system in solution or one in a hydrous oxide, e.g., RuO_2, IrO_2, Co_3O_4.

We think that other method, such as the microwave digestion system [213], could also possess the same result. It should be noticed that even though the estimation of Pt quantity by EDX mapping mounted on the SEM equipment is not precisely accurate, the measurement is still reliable on the calculation.

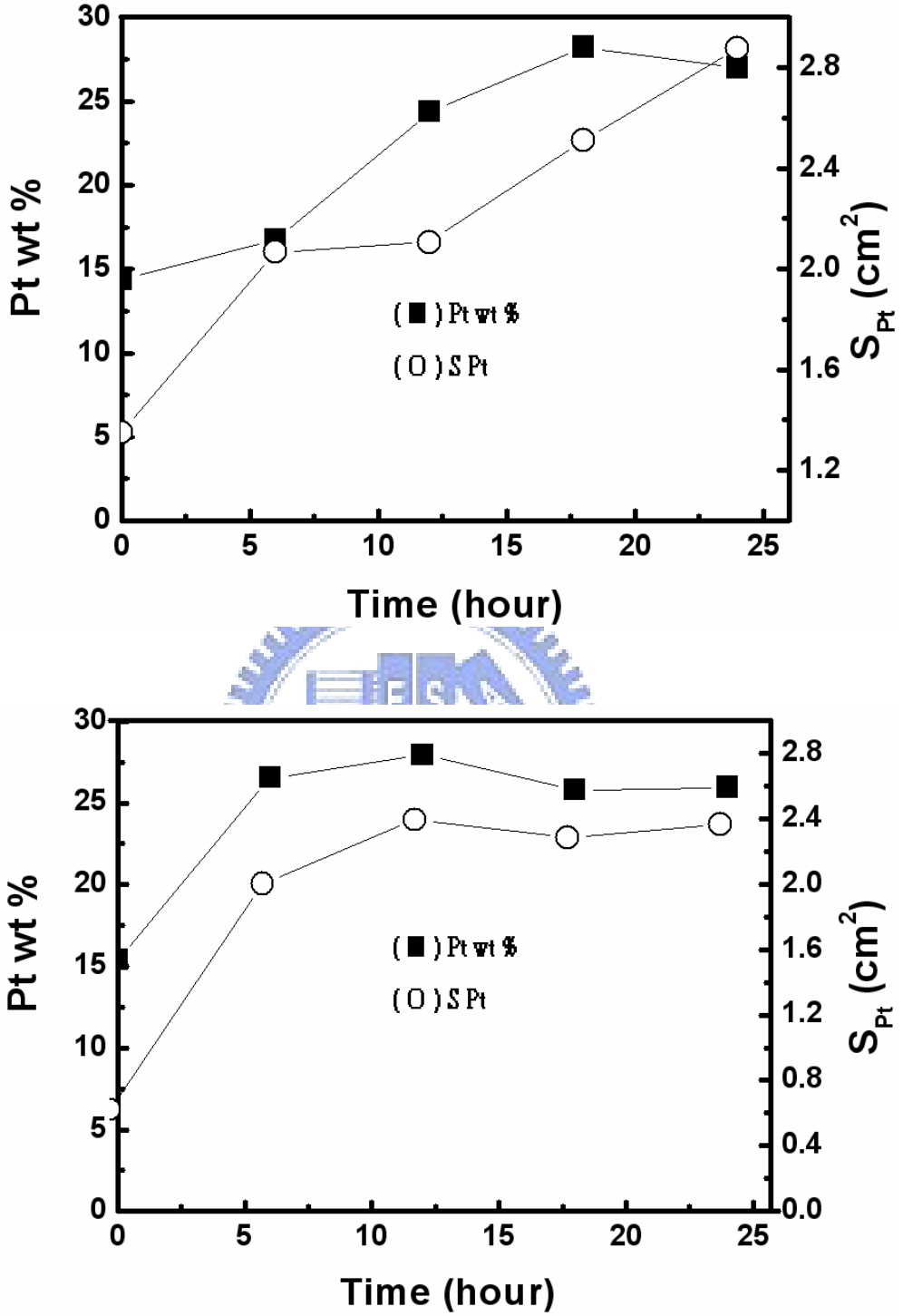

Figure 5.6 Function of the active surface area and Pt wt% as the period time of chemical oxidation (0 hr ~ 24 hours); (a) 2M, and (b) 14M.

5.1.3 Summary

Aligned MWCNTs electrode was used as the target to specify the influence of chemical treatment on attaching functional groups. The length and diameter of the aligned MWNTs are approximately 20 μm and 20 nm, respectively. After the modification with higher concentration of HNO_3 at 90℃, the integrated MWNTs-electrode becomes higher in porosity due to the action of the residues of amorphous carbon, which is shown on the end opening. The results of the FTIR and XPS analysis reveals that the surface of MWNTs behaves in such a way which indicates the existence of tertiary alcohol (-OH) and the carboxylic acids (-COOH). The loading quantity of Pt is highly correlated to the amount of functional groups, which could be attached to the cap, sidewall and particularly the inner part of MWNTs. Eventually a stabilization of loading quantity could be found for 2M and 14M nitric acid, corresponding to the maximum quantity of functional groups with a fraction of nearly ½.

5.2 Electrochemical investigations of carbon nanomaterials

After confirming the optimum parameters of chemical treatment for the maximum quantify of functional groups, we in turn underwent the electrochemical measurements to figure out the characteristics of various carbon nanomaterials (CNMs). In this section, we compared the electrical properties among (1) aligned MWCNTs and coral-like CNTs (2) 2-D and 3-D CNWs in aqueous solution as the electrolyte, and (3) finally the entangled MWCNTs and coral-like materials in GBL ion solution.

5.2.1 Aligned MWCNTs and coral-like CNTs in aqueous solution (H_2SO_4/H_2O)

5.2.1.1 Experimental details

Prior to electrochemical examination, both carbon-based electrodes were subjected to oxidization with 14 M HNO_3 at 90 °C for 6 h and then they were rinsed with deionized water for 20 min. A symmetrical arrangement with an area of 0.5 cm^2 was used to investigate the electrical properties. A Ag/AgCl electrode served as the reference electrode.

Cyclic voltammetry (CV; potential window ranging from 0 to +1 V) and AC impedance measurements (over the range from 10 mHz to 100 MHz) were performed in 1 M H_2SO_4 as the electrolyte using a CHI 6018B Series Instrument. The scan rates for the CV measurements were 10, 50, 100, and 200 mV/s. In addition, constant-current charge/discharge measurements were performed at 1 mA to estimate the capacitances, using the equation

$$C = i/m(dE/dt) \cong it/m\Delta E \tag{5.4}$$

where i is the current density, m is the mass of electrode material, t is the period of time during discharge, and ΔE is the voltage decrease. Finally, both devices were subjected to the charge/discharge process over 1000 cycles to test their reliabilities.

5.2.1.2 Electrochemical measurements

Prior to electrical measurements, we chemically oxidized both electrodes to attach functional groups onto their surfaces and to improve their wettability. Previous studies have revealed [214, 215] that the capacitance can be promoted by the presence of surface functional groups obtained after chemical or plasma treatment.

We performed CV [Figure 5.7(a) and (b)] and constant-current discharge [Figure 5.7(c)] and AC impedance (Figure 5.8) measurements to investigate the electrical properties of both electrodes. In this study, the coral-like CNTs electrode exhibited greater capacitive properties than did the well-aligned CNTs electrode. The CV curves of the two electrodes reveal that they are both traditional electrochemical capacitors, with two humps corresponding to the redox reactions at the interface where the electron transmission proceeds between functional groups and ions. The performance of the CNTs-CNWs electrode—with its rectangular CV trace—appears to be much closer to that of an ideal capacitor; it exhibited its capacitive properties even at a quite high scan rate of 200 mV/s. We used constant-current discharge diagrams to determine that the capacitances of the coral-like CNTs and well-aligned CNTs electrodes were ca. 194 and 104 F/g, respectively. The results are consistent with the CV measurements. We believe that the larger capacitance of the coral-like CNTs electrode arose because of its larger accessible area; i.e., its configuration, akin to that of a porous structure, led to an enhancement of the surface area.

The semicircles in the Nyquist curves [Figures 5.8(a) and 5.8(b)], revealed in the magnified Z′′ vs. Z′ complex-plane plots, represent the Faradic resistance in parallel with a double-layer charging component. The contact resistance of the well-aligned CNTs electrode (1.4 W) was larger than that of the coral-like CNTs electrode. Furthermore, the sloped region in Figure 5.8(b), which is related to the surface of electrode, reveals the distribution resistance of ions in the electrode. We suspect that the inner region of the electrode was rinsed well during the acidic oxidation process, and that the coral-like CNTs provided a better pathway

for ions. Nevertheless, even though it exhibited distribution resistance, the coral-like CNTs electrode possessed a larger capacitance because of the presence of the porous CNW structure, which presumably enhanced the accessible surface area. The fitting diagrams reveal that both electrodes can be categorized as traditional electrochemical capacitors, where the w_1 is referred to as the effect of diffusion control. Finally, the capacitance decay of both electrodes was ca. 9% after 1000 cycles [Figure 5.9]. Thus, the coral-like CNTs electrode exhibits great experimental durability, just like that of the pure CNTs electrode. We suspect that this behavior arose because of the graphitic structures of carbon nanoflakes and nanotubes and the great accessibility of ions in the electrodes.

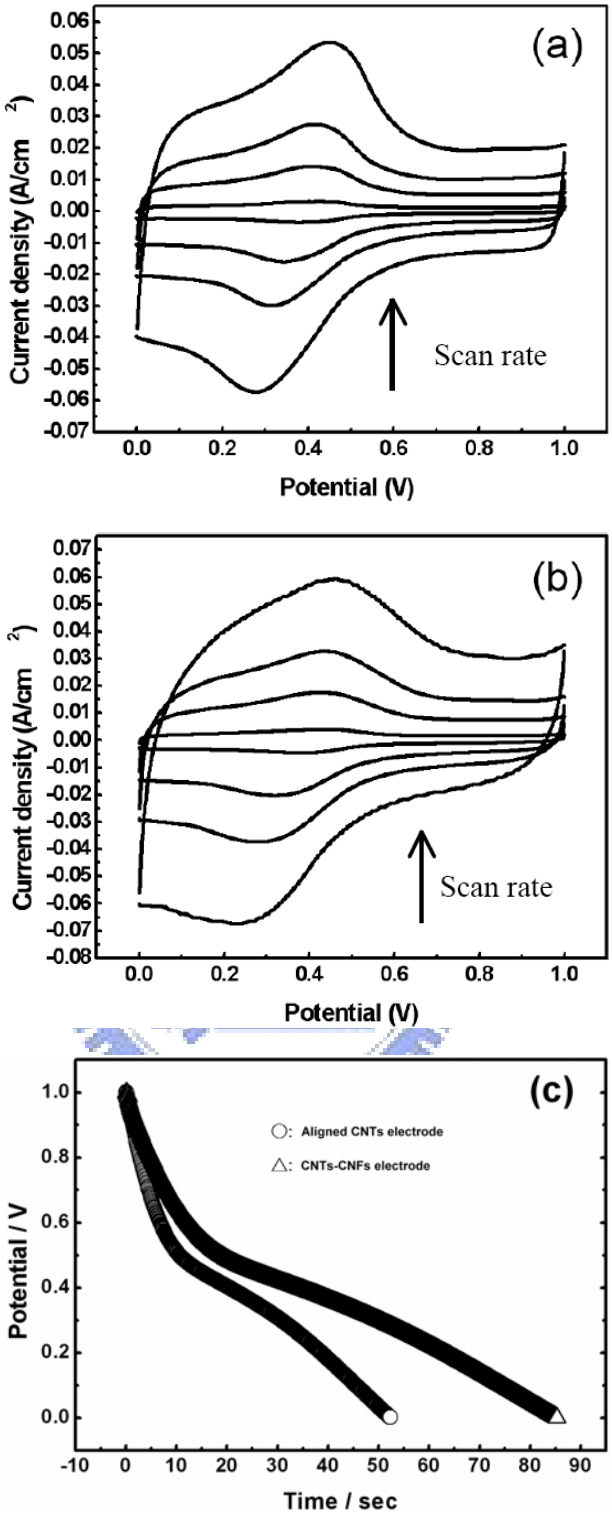

Figure 5.7 Cyclic voltammograms of (a) the well-aligned CNTs electrode and (b) the CNTs-CNWs electrode (electrolyte: 1 M H_2SO_4; scan rates: 10, 50, 100, and 200 mV/s); (c) constant-current discharge diagrams of the well-aligned CNTs and CNTs-CNWs electrodes (constant discharge current: 1 mA).

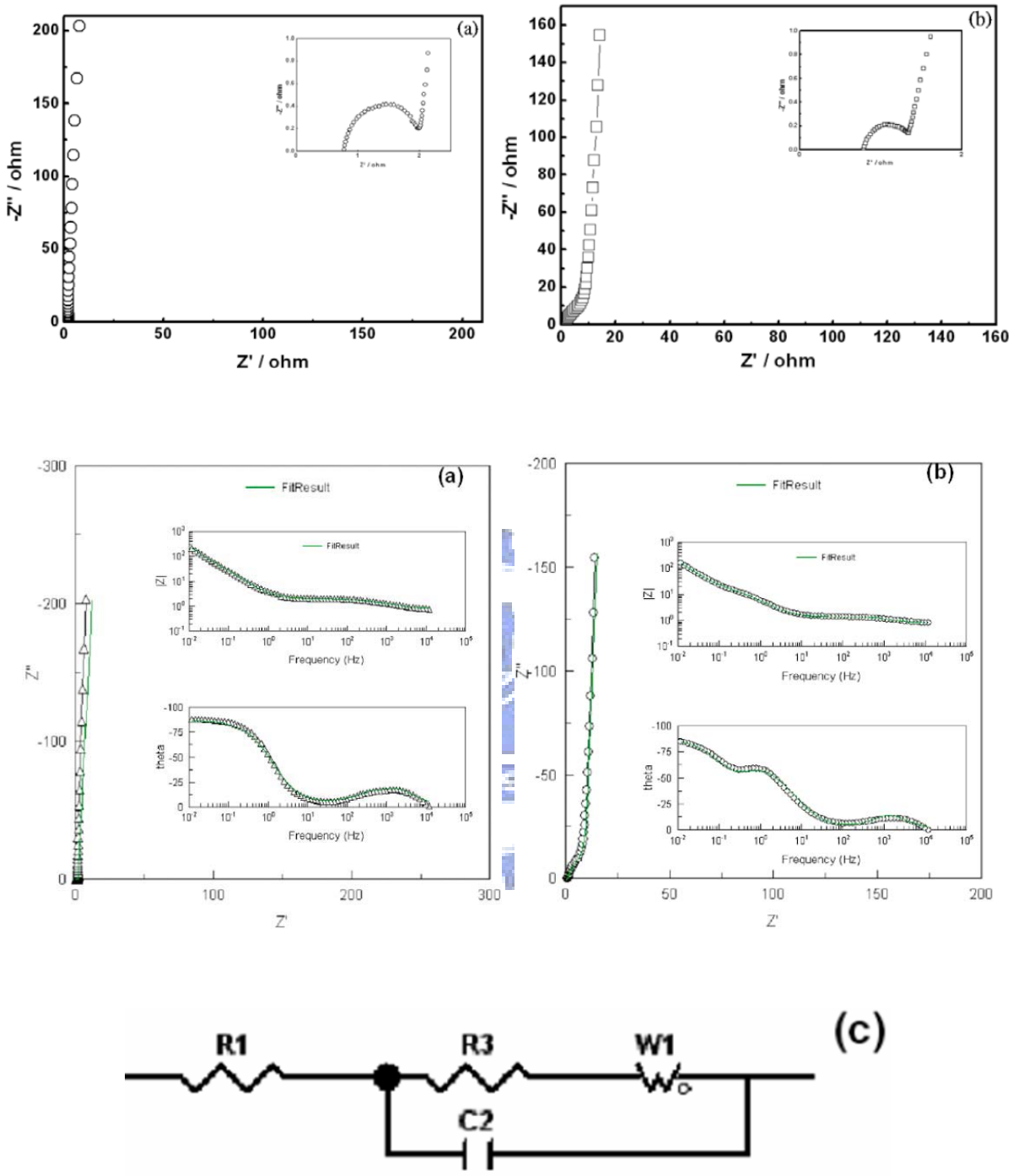

Figure 5.8 AC impedance plots (top) and fitting diagrams (bottom) for the (a) well-aligned CNTs and (b) CNTs-CNWs electrodes; (c) the equivalent circuit.

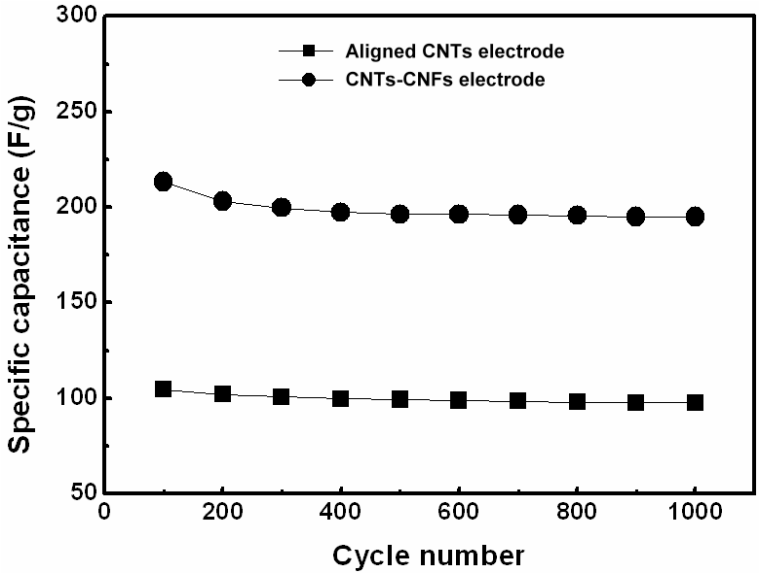

Figure 5.9 Durability tests for the aligned CNTs and CNTs-CNWs electrodes; capacitance decay: ca. 9%.

5.2.2 2-D and 3-D CNWs in aqueous solution (H_2SO_4/H_2O)

5.2.2.1 Experimental details

We took the advantage of the double-layered CNWs, presenting flower-like CNWs, to compare the capacitive properties with the as-grown CNWs sheet. Prior to electrochemical measurements, both electrodes were modified in high concentrated sulfuric acid (14M) at 95°C for 12 hours to make surfaces functionalized for an electrochemical capacitor. CV measurement shows the dependence of current density on potential (0~1 Volt) at different scan rates from 5 to 100 mV/s in 1M H_2SO_4 aqueous as the electrolyte. The specific capacitance was measured as follows:

$$C = i/ms \tag{5.5}$$

where i is the current density, m is the mass of electrode material, and s is the scan rate.

5.2.2.2 Electrochemical measurements

It showed traditional diagrams of the electrochemical capacitor with Faradic reactions, all presenting two humps in Figure 5.10. Specifically, the linear relationship of current densities to increasingly applied scan rates identifies the fact that the two humps are correlated with the redox reactions [Figure 5.10(a)]. Compared to the as-grown aligned CNWs electrode, the capacitance behaviors of the double-layered CNWs performed much greater at different scan rates, depending on the integrated area of CV measurements [Figure 5.10(b)-5.10(d)]. Even though operated at a high scan of 100 mV/s [Figure 5.10(d)], the double-layered electrode also showed the trend to a pseudocapacitor behavior with a nearly rectangular shape. The large slopes ($\triangle I$ / $\triangle$V) demonstrated by the boxes in Figure 5.10(a) indicate that the 3D electrode has faster charging and discharging responses to applied potential. In addition to the apparent redox humps at close to 0.4 V, there was also a reactive signal found at close to 0.1 V, especially visible on the monolayer CNWs electrode. It also related to the reactions in the interface where electron transition were preceded between surface functional groups and the electrolyte ions (H_2SO_4/H_2O). However, it is hard to identify what the functional group is. As reported, most of the functional group attached to the surface was $–COO^-$ with few content of $–O^-$ and the –COO- ion was more reactive than the other one [216]. We suspected that the function participating in the reaction might be of $–O^-$. As for capacitances calculated by equation C_F= I / (V*M), where C_F is Faradic capacitance, I current density, V scan rate, and M mass of the carbon nanomaterials, the double-layer CNWS electrode was more four times larger than the monolayer aligned CNWs, depending on the measurements from CV curves. The capacitance of the flower-like CNWs electrode tremendously increased to be 198.6 F/g, which was comparatively larger than that of oxidized SWNHs electrode. The normal 2D CNWs film in our study presented the capacitance of 48.4 F/g. This enhanced capacitance may be imparted by a high accessibility of solvated ions ($SO_4^{2-}(H_2O)_{12}$) to internal regions through the network of microporous structure. It is noted

that the diameter of $SO_4^{2-}(H2O)_{12}$ determined by computer simulation study is about 0.53 nm [217]. It was concluded that with the addition of flower-like nanowalls on the normal 2D film truly improved the capacitive performance, and indeed gave another route of nanowall-related materials for energy storage applications. There is no doubt that more effort should be made.

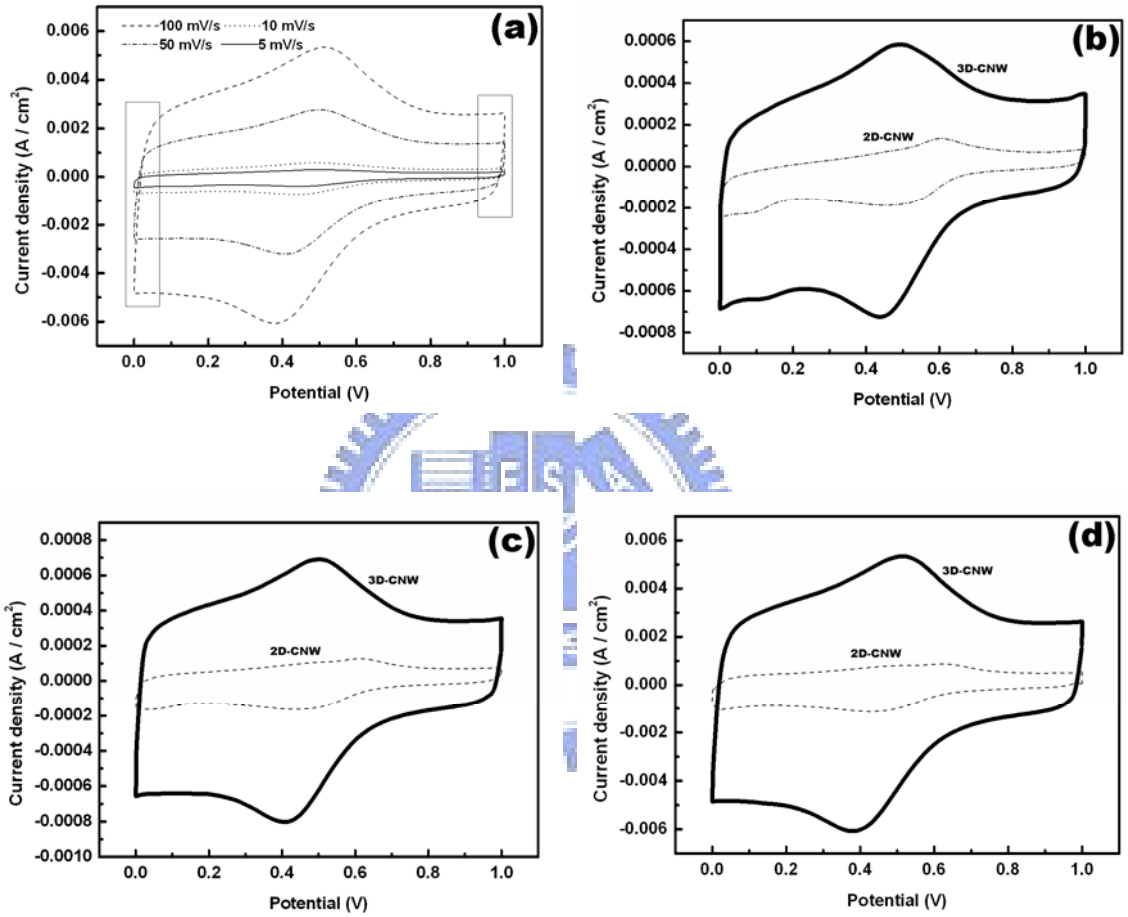

Figure 5.10 Cyclic voltammegrams of (a) the double-layer CNWs electrode performed at different scan rates from 5 to 100 mV/s, and of the monolayer and double-layer CNWs electrodes performed at (b) 10 mV/s, (c) 50 mV/s, and (d) 100 mV/s. 1M H_2SO_4 aqueous was used as the electrolyte.

5.2.3 Entangled MWCNTs and coral-like materials in non-aqueous electrolyte (GBL ion solution)

5.2.3.1 Experimental details

Gamma-butyrolactone (GBL) ion solution, containing tetra-methyl ammonium and phthalates, serves as the electrolyte. Two identical electrodes were assembled face-to-face by a separator. Both sandwich-like devices underwent the measurements of cyclic voltammetry (C-V) (potential window of 0~1.5V) and AC impedance (frequency range of 1~10^5 Hz) at 298 K by the CHI 6018B Series Instrument to characterize electrochemical properties. The cyclic voltammogram was utilized to estimate the specific capacitance as follows:

$$C = i/m(dE/dt) \cong i/m(\Delta E/\Delta t) \tag{5.6}$$

where i is the current density, m the mass of electrode material, and $\Delta E/\Delta t$ the scan rate. Finally, investigation of the durability of both electrodes was carried out over 2000 cycles.

5.2.3.2 Electrochemical measurements

The cyclic voltammograms of pure CNTs and coral-like CNTs are performed in Figure 5.11(a) and 5.11(b), respectively. The potential window was determined by the measurement of Linear Sweep Voltammetry (not shown here), showing a range of 1.5 V with respect to the potential of reference electrode. The potential window was lower than the swing voltage of ca. 1.7 V at which the electrode is sustainable to the limitation with no other impurities in the solution. The plots show no Faradaic responses and are close to a rectangular shape, corresponding to the ideal capacitor [218], in a wide range of scan rates from 0.05 to 1 V/s. Even at a high scan rate of 1 V/s, both electrodes still keep being an ideal double-layer capacitor. This resulted from the good conductivity and stability of the carbon structures, and

great transportation of free ions within the network as well. In addition to a double layer formed on the interface of electrode material, a deviation of slope from a ideal rectangular shape on the anodic semicircle of CV diagram in Figure 5.11(a) represents that there was an leakage of current happened across the double layer which was compacted by the anion in the inner layer. The anion was likely to pass the region when the double layer with a large electric field was established on the surface. However, this situation did not arise on the CNTs-CNWs electrode. We presumably suggest that the existence of porous structure of CNWs and the surface roughness of carbon material restrained the field-related leakage. The great wettability of GBL solvent made the penetration of solution and ions easier toward the interior region of electrode and also solved the problem with inefficient use of inner electrode. The higher current density shown in Figure 5.11(b) referred to a higher capacitance for the CNTs-CNWs electrode than pure CNTs electrode. The capacitance of CNTs-CNWs electrode nearly doubled that of the CNTs electrode to be about 147 F/g, examined at the scan rate of 0.1 V/s. As reported by Keiser et al., such porous structure was more suitable for electrochemical applications from the investigation of corresponding complex-plane impedance plots [219]. This result is highly correlated with the enhancement of surface area and porous structure of the graphitic carbon nanowalls. Furthermore, the distorted graphitic planes of attached carbon nanowall with sp^2 structure become of chemical characteristics differing from the closed carbon shells, which are chemical inert on account of the high in-plane covalent bonds (5 eV/bond). For example, functional groups, such as C=O and C-OH, could be incorporated prevalently into the edge of defective planes. As a result, the intercalation of ions and the adsorption of ions on the edge site are more available to the CNWs. As a whole, the coral-like CNT electrode possessing high energy and power densities are considered to be more suitable for EDLC application.

Nyquist plots of AC impedance measurements are shown in Figure 5.12. Both electrodes depicted the features of a typical double-layer capacitor for porous structure, starting with a

transmission line at higher frequency and exhibiting a virtually vertical line at low frequency. The non-ideality at low frequency is typical and riding on the distribution in microscopic charge transfer rates, adsorption process, or surface roughness or a distribution in macroscopic path lengths. Transmission lines observed at high frequency in both diagrams referred to the distribution resistance that is different from the diffusion control as a limiting factor in the kinetics of the electrode process in plane-type capacitor [220]. That is, the slope region is the consequence of uniform distribution of CNWs porous structure. In addition, lower equivalent series resistance (ESR) arose for the coral-like CNTs electrode than pure CNTs electrode, which was primarily correlated with the external circuit connection and the structure itself. Even though the difference is slight, we suggest that graphitization of the CNT-CNW is better than that of the pure CNT and that the contact degree of the CNTs with exterior porous structure performs well. This is correlated with the existence of oxygen-containing items such as OH in the plasma which is beneficial to diminish amorphous carbons to approach a higher degree of crystallization. For adsorption of items, the porous structure due to the CNWs was more accessible for ions in the electrolyte system. It could be summarized that the common electrode material of pure CNTs for the use of EDLC could be replaced by CNTs-CNWs.

Finally, to understand the durability of both electrodes, cycling test were examined for 2000 cycles at 100 mV/s, as we can see in Figure 5.13. Both electrodes showed great reliability with an acceptable columbic efficiency of 94%, while operated over 2000 cycles. This reveals that the coral-like CNTs electrode could perform as very well as pure CNTs electrode on account of the graphite structure. According to the excellent electrochemical properties, the electrode containing carbon nanotubes decorated by nanowalls could be a promising candidate of electrode materials and provide another route on the application of supercapacitor.

As regarding to the electrochemical measurements, the coral-like CNTs electrode has much larger capacitance than pure CNTs electrode on account of the existence of additional porous structure. The outstanding performance of long cycle life provides the coral-like CNTs material with another route in the applications of electrical storage systems.

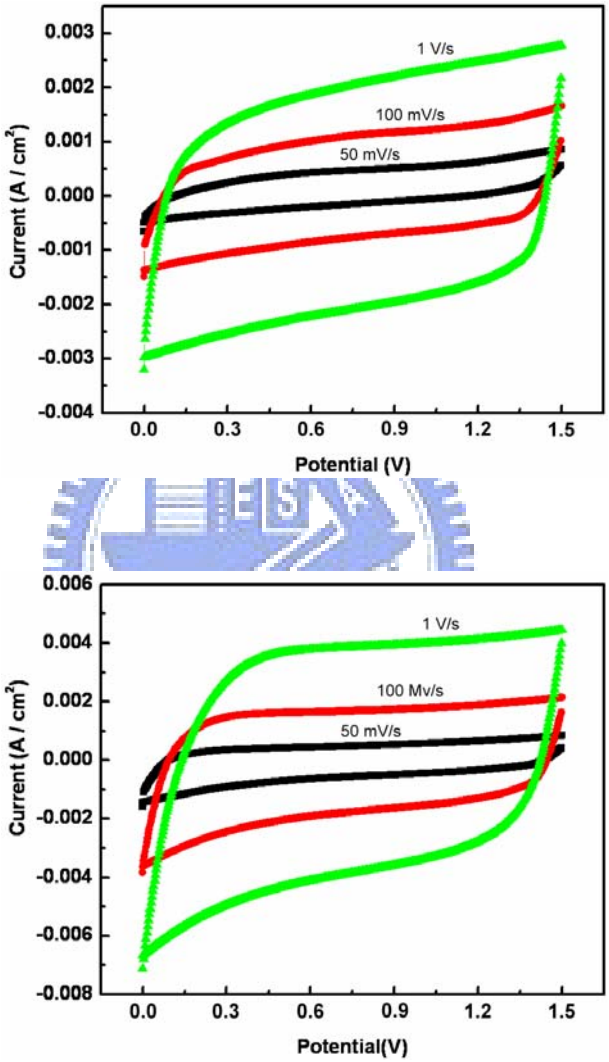

Figure 5.11 Cyclic voltammograms of (a) the pure CNTs electrode and (b) the CNTs-CNWs electrode in GBL ion solution as the electrolyte. The scan rate ranges from 50 mV/s to 1 V/s.

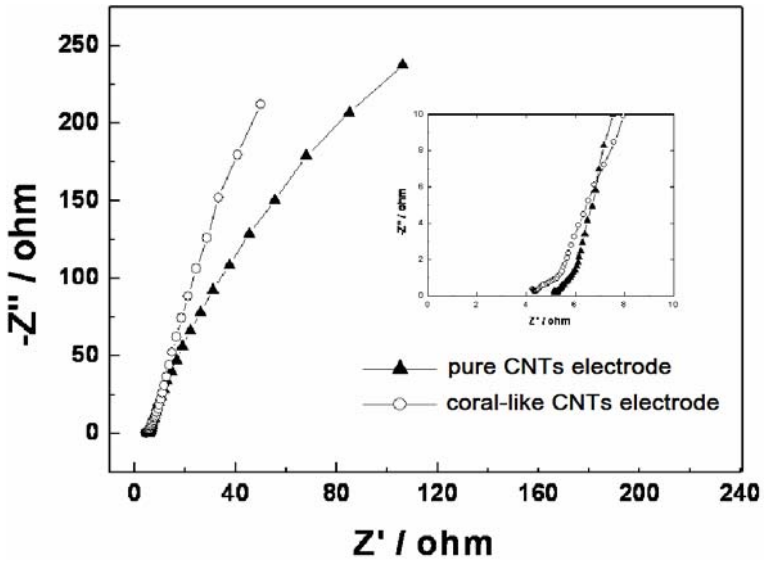

Figure 5.12 Nyquist plots of two electrodes, performed at the frequency ranging from 1 to 10^5 Hz. Pure CNTs electrode was denoted by ▲ and CNTs-CNWs electrode by ○.

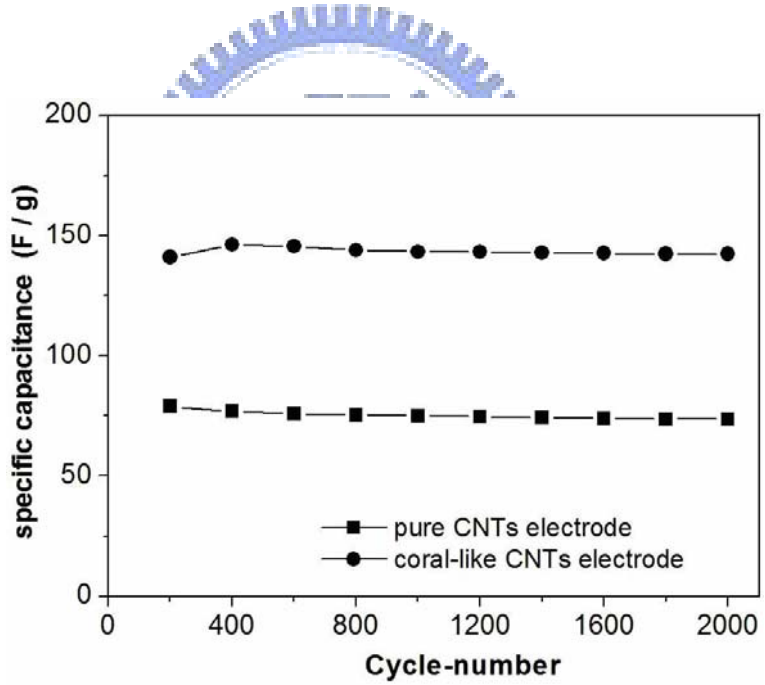

Figure 5.13 Measurements of the durability of two electrodes performed at the scan rate of 100 mV/s. Pure CNTs electrode was denoted by ■ and CNTs-CNWs electrode by ●.

The preceding impedance results and discussion suggest that an equivalent circuit corresponding to the impedance responses of the present system should involve three zones in series: the bulk solution, the contact interface between the carbon fibers as well as that between the carbon cloth and current collector, and the electrolyte/carbon interface in micropores. An equivalent circuit depicting the above description is shown in Figure 5.14, in which the elements involve the bulk solution resistance, R_s, the capacitance and resistance due to the contact interface, C_c and R_c, and a Warburg diffusion element attributable to the ion diffusion in pores, Z_W.

This parameter is an increasing function of the resistance for electrolyte transport in a porous electrode. At sufficiently high frequencies, the overall impedance can be reduced to an equation that corresponds to a locus showing a semicircle that intercepts the real axis at R_s and $R_s + R_c$ in the Nyquist plot.

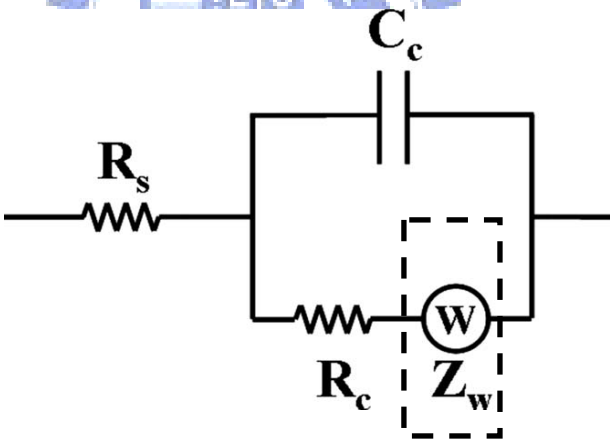

Figure 5.14 Equivalent circuit for the simulation of the impedance spectra of the capacitor cells shown in Figure 5.12.

5.2.4 Summary

We presented for the first time the construction dependence of so-called 3-D CNWs, containing flower-like CNWs aggregations, on specific capacitance and application possibility of the flower-like CNWs to electrode for supercapacitors. Our study clearly revealed that the existence of flower-like CNW aggregation played an important role on improving surface area for the performance of soaring capacitance. We think that the transformation of 2-D to 3-D construction, attributed to the assistance of oxygen functions, open the window of CNW materials to energy storage systems. In addition, the presence of the CNWs in the CNTs-CNWs electrode led to an increase in capacitance, because of the porous structure and the larger accessible area, relative to that of the well-aligned CNTs electrode or entangled CNTs electrode. All kinds of electrode in this study exhibited high reliability, possessing high supercapacitor efficiency over 2000 cycles. We suspect that the unique structures of the carbon nanomaterials electrodes might provide remarkable performance when used in energy storage systems. We also expect that the 3-D construction can be designed by controlling the surface modification to possessing multi-layer stacking type for other applications in the future.

Chapter6 Conclusions

In the first part of the thesis, aligned multi-wall carbon nanotubes can be synthesized on the Fe-coated carbon cloth by bias-assisted MPCVD. Applying an external bias large enough is essential to achieve the vertical growth on the influence of anisotropic deposition of carbon. It is obvious that in comparison, interlaced MWCNTs appear without an external, negative bias applied on the electrode. Besides, the Van der Waals force between MWCNTs is helpful and necessary for gathering MWCNTs to present the dense arrangement. The growth mechanism follows the VLS model. The Raman and X-ray measurements depict that the carbon nanomaterial is of crystalline property, corresponding to the common characteristics of MWCNTs.

We have also used the same deposition facility to synthesize CNTs presenting graphitic nanowalls on carbon cloth and stainless steel substrates. We fabricated CNTs presenting a graphitic petal-like carbon material in one step after introducing H_2-CH_4 and CO_2-CH_4 as reactant gases. The annealing catalyst and the external bias both had significant effects on the formation of coral-like CNTs presenting nanowalls. In our studies, the influence of external bias on the formation of coral-like CNTs was different and depended on the cases. In particular, the CNTs formed in the CO_2-CH_4 could be covered throughout with CNWs owing to the assistance of oxygen-containing items. In addition, the oxygen-containing items also leads the CNWs to be fabricated on the initial CNWs attached to the CNTs. Therefore, it was suggested that the CO_2-CH_4 plasma system is beneficial for the synthesis of carbon nanowalls in a catalyst-free process of synthesis.

2-D and 3-D CNF structures have been fabricated in a CO_2/CH_4 plasma system. Because our fabrication technique is a catalyst-free process, the resulting materials do not require a purification prior to use. The applied microwave power had crucial influence on the

degree of crystallization of the products. Microscopy and micro-Raman spectroscopic measurements revealed that highly ordered graphite structures were readily obtained at low power (200–300 W). The specific surface area of the 3-D structure was almost double that of the 2-D structures because the 3-D structure comprised an aggregate of many flower-like nanowalls and, thereby, possessed a microporous structure. In addition, we think that the transformation of monolayer to double-layer construction attributed to the assistance of oxygen functions, open the window of CNW materials to energy storage systems. We also expect that the construction can be designed by controlling the surface modification to possessing multi-layer stacking type for other applications in the future.

In the second part, we are going to first identify the quantitative limitation of functional groups attached to surface of carbon materials. Aligned MWCNTs electrode was used as the target to specify the influence of chemical treatment on attaching functional groups. After the modification with higher concentration of HNO_3 at 90℃, the integrated MWNTs-electrode becomes higher in porosity due to the action of the residues of amorphous carbon, which is shown on the end opening. The results of the FTIR and XPS analysis reveals that the surface of MWNTs behaves in such a way which indicates the existence of tertiary alcohol (-OH) and the carboxylic acids (-COOH). The loading quantity of Pt is highly correlated to the amount of functional groups, which could be attached to the cap, sidewall and particularly the inner part of MWNTs. Eventually a stabilization of loading quantity could be found for 2M and 14M nitric acid, corresponding to the maximum quantity of functional groups with a fraction of nearly ½.

Then we presented the construction dependence of so-called 3-D CNWs, containing flower-like CNWs aggregations, on specific capacitance and application possibility of the flower-like CNWs to electrode for supercapacitors. Our study clearly revealed that the existence of flower-like CNW aggregation played an important role on improving surface area for the performance of soaring capacitance. The capacitance of the 3-D construction can

be effectively increased to be around 197 F/g. We think that the transformation of 2-D to 3-D construction, attributed to the assistance of oxygen functions, will open the window of CNW materials to energy storage systems. In addition, the presence of the CNWs in the CNTs-CNWs electrode led to an increase in capacitance, because of the porous structure and the larger accessible area, relative to that of the well-aligned CNTs electrode or entangled CNTs electrode. All kinds of electrode in this study exhibited high reliability, possessing high supercapacitor efficiency over 2000 cycles. We suspect that the unique structures of the carbon nanomaterials electrodes might provide remarkable performance when used in energy storage systems. Finally, we also expect that the 3-D construction can be designed by controlling the surface modification to possessing multi-layer stacking type for other applications in the future.

Reference

1. http://www.enterprisemission.com/images_v2/Iapetus5/carbon-allotropes.jpg

2. R. Saito, G. Dresselhaus, M.S. Dresselhaus, Imperical College Press, London (1998)

3. R.E. Smalley. Formation and properties of C60 and the fullerences, National Institute of Standards and Technology, Dec. 6-7, 1990.

4. S. Iijima, Nature 354 (1991) 56

5. S. Iijima, T. Ichihashi, Nature 363 (1993) 603

6. R. Saito, M. Fujita, G. Dresselhaus, M.S. Dresselhaus, Appl. Phys. Lett. 60 (1992) 2204.

7. J.-M. Bonard, H. Kind, T. Stöckli, L.O. Nilsson, Solid State Electronics 45 (2001) 893.

8. E.T. Thostenson, Z. Ren, T.-W. Chou, Composites Science and Technology 61 (2001) 1899.

9. K. Tanaka, K. Okahara, M. Okada, T. Yamab, Chem. Phys. Lett. 191 (1992) 469.

10. D. Bernaerts, M. Op De Beeck, S. Amelinckx, J. Van Landuyt, G. Van Tendeloo, Philos. Mag. A 74 (1996) 723.

11. X.F. Zhang, X.B. Zhang, G. Van Tendeloo, S. Amelinckx, M. Op de Beeck, J. Van Landuyt, J. Cryst. Growth 130 (1993) 3.

12. S. Iijima, T. Ichihashi, Y. Ando, Nature 356 (1992) 776.

13. L. Chico, V.H. Crespi, L.X. Benedict, S.G. Louie, M.L. Cohen, Phys. Rev. Lett. 76 (1996) 971.

14. N. Hamada, S.-I. Sawada, A. Oshiyama, Phys. Rev. Lett. 68 (1992) 1579.

15. X. Blase, L.X. Benedict, E.L. Shirley, S.G. Louie, Phys. Rev. Lett. 72 (1994) 1878.

16. J.W. Mintmire, C.T. White, Carbon 33 (1995) 893.

17. C.L. Kane, E.J. Mele, Phys. Rev. Lett. 78 (1997) 1932.

18. M.S. Dresselhaus, G. Dresselhaus, P.C. Eklund, Academic Press, Boston (1996).

19. P.R. Wallace, Phys. Rev. 71 (1947) 622.

20. J.W.G. Wildöer, L.C. Venema, A.G. Rinzler, R.E. Smalley, C. Dekker, Nature 391 (1998) 59.

21. T.W. Odom, J.L. Huang, P. Kim, C.M. Lieber, Nature 391 (1998) 62.

22. L.C. Venema, J.W.G. Wildöer, C. Dekker, A.G. Rinzler, R.E. Smalley, Appl. Phys. A 66 (1998) S153.

23. T.W. Odom, J.L. Huang, P. Kim, C.M. Lieber, J. Phys. Chem. B 104 (2000) 2794.

24. L.C. Venema, J.W.G. Wildöer, J.W. Janssen, S.J. Tans, H.L.J. Temminck Tuinstra, L.P. Kouwenhoven, C. Dekker, Science 283 (1999) 52.

25. P. Kim, T.W. Odom, J.-L. Huang, C.M. Lieber, Phys. Rev. Lett. 82 (1999) 1225.

26. S.J. Tans, A.R.M. Verschueren, C. Dekker, Nature 393 (1998) 49.

27. R. Martel, T. Schmidt, H.R. Shea, T. Hertel, Ph. Avouris, Appl. Phys. Lett. 73 (1998) 2447.

28. M. Bockrath, D.H. Cobden, P.L. McEuen, N.G. Chopra, A. Zettl, A. Thess, R.E. Smalley, Science 275 (1997) 1922.

29. S.J. Tans, M.H. Devoret, H. Dai, A. Thess, R.E. Smalley, L.J. Geerligs, C. Dekker, Nature 386 (1997) 474.

30. S.J. Tans, M.H. Devoret, R.J.A. Groeneveld, C. Dekker, Nature 394 (1998) 761.

31. M. Bockrath, D.H. Cobden, J. Lu, A.G. Rinzler, R.E. Smalley, L. Balents, P.L. McEuen, Nature 397 (1999) 598.

32. A. Bachtold, C. Strunk, J.-P. Salvetat, J.-M. Bonard, L. Forró, T. Nussbaumer, C. Schönenberger, Nature 397 (1999) 673.

33. H.T. Soh, C.F. Quate, A.F. Morpurgo, C.M. Marcus, J. Kong, H. Dai, Appl. Phys. Lett. 75 (1999) 627.

34. C. Schönenberger, A. Bachtold, C. Strunk, J.-P. Salvetat, L. Forró, Appl. Phys. A 69 (1999) 283.

35. J. Kong, C. Zhou, A. Morpurgo, H.T. Soh, C.F. Quate, C. Marcus, H. Dai, Appl. Phys. A 69 (1999) 305.

36. K. Liu, M. Burghard, S. Roth, P. Bernier, Appl. Phys. Lett. 75 (1999) 2494.

37. P.L. McEuen, M. Bockrath, D.H. Cobden, Y.-G. Yoon, S.G. Louie, Phys. Rev. Lett. 83 (1999) 5098.

38. H. Dai, E.W. Wong, C.M. Lieber, Science 272 (1996) 523.

39. L. Langer, V. Bayot, E. Grivei, J.-P. Issi, J.P. Heremans, C.H. Olk, L. Stockman, C. Van Haesendonck, Y. Bruynseraede, Phys. Rev. Lett. 76 (1996) 479.

40. T.W. Ebbesen, H.J. Lezec, H. Hiura, J.W. Bennett, H.F. Ghaemi, T. Thio, Nature 382 (1996) 54.

41. B.I. Yakobson, C.J. Brabec, J. Bernholc, Phys. Rev. Lett. 76 (1996) 2511.

42. B.I. Yakobson, G. Samsonidze, G.G. Samsonidze, Carbon 38 (2000) 1675.

43. M.M.J. Treacy, T.W. Ebbesen, T. M. Gibson, Nature 381 (1996) 678.

44. E.W. Wong, P.E. Sheehan, C.M. Lieber, Science 277 (1997) 1971.

45. D.A. Walters, L.M. Ericson, M.J. Casavant, J. Liu, D.T. Colbert, K.A. Smith, R.E. Smalley, Appl. Phys. Lett. 74 (1999) 3803.

46. M.-F. Yu, O. Lourie, M.J. Dyer, K. Moloni, T.F. Kelly, R.S. Ruoff, Science 287 (2000) 637.

47. M.-F. Yu, B.S. Files, S. Arepalli, R.S. Ruoff, Appl. Phys. Lett. 84 (2000) 5552.

48. http:// 140.114.18.223/~hcshih/diamond/nanotube.html (2000).

49. T.W. Ebbesen, P.M. Ajayan, Nature 358 (1992) 220.

50. Yihong Wu, Bingjun Yang, Nano Letters 2 (2002) 355.

51. Alexander N. Obraztsov, Alexander P. Volkov, Igor Pavlovsky, Diamond and Related Materials 9 (2000) 1190.

52. C. Bower, W. Zhu, S. Jin, and O. Zhou, Appl. Phys. Lett. 77 (2000) 830.

53. C. Bower, O. Zhou, W. Zhu, D. J. Werder, and S. Jin, Appl. Phys. Lett. 77 (2000) 2767.

54. J. B. O. Caughman, L. R. Baylor, M. A. Gulliorn, V. I. Merkulov, D. H. Lowndes, and L. F. Allard, Appl. Phys. Lett. 83 (2003) 1207.

55. A. G. Rinzler, J. H. Hafner, P. Nikolaev, L. Lou, S. G. Kim, D. Tomanek, P. Nordlander, D. T. Cobert, and R. E. Smalley, Science 269 (1995) 1550

56. A. C. Dillon, K. M. Jones, T. A. Bekkedahl, C. H. Kiang, D. S. Bethune, and M. J. Heben, Nature 386 (1997) 377

57. G. Che, B. B. Lakshmi, E. R. Fisher, and C. R. Martin, Nature 393 (1998) 346

58. W. A. de Heer, A. Chatelain, and D. Ugarrte, Science 270 (1995) 1179.

59. Y. Ando, X. Zhao, and M. Ohkohchi, Carbon 35 (1997) 153.

60. Y.H. Wu, P.W. Qiao, T.C. Chong, and Z.X. Shen, Adv. Mater. 14 (2002) 64.

61. S. Kurita, A. Yoshimura, H. Kawamoto, T. Uchida, K. Kojima, and M. Tachibana, J. Appl. Phys. 97 (2005) 104320

62. B. L. French, J. J. Wang, M. Y. Zhu, and B. C. Holloway, J. Appl. Phys. 97 (2005) 114317.

63. X. Zhao, R. A. Outlaw, J. J. Wang, M. Y. Zhu, G. D. Smith, and B. C. Holloway, J. Chem. Phys. 124 (2006) 194704.

64. Y. Ando, X. Zhao, M. Ohkohchi, Carbon 35 (1997) 153.

65. Y. Wu, B. Yang, B. Zong, Z. Shen, Y. Feng, J. Mater. Chem. 14 (2004) 496.

66. P.M. Ajayan, O.Z. Zhou, Carbon Nanotubes 80 (2001) 391

67. R.H. Baughman, A.A. Zakhidov, W.A. de Heer, Science 297 (2002) 787

68. D. Rotman, Nature & Techniek 70 (2002) 30

69. T.W. Ebbesen, P.M. Ajayan, Nature 358 (1992) 220.

70. S. Iijima, T. Ichihashi, Nature 363 (1993) 603.

71. D.S. Bethune, C.H. Klang, M.S. de Vries, G. Gorman, R. Savoy, J. Vazquez, R. Beyers, Nature 363 (1993) 605.

72. J. Abrahamson, P.G. Wiles, B.L. Rhoades, Carbon 37 (1999) 1873.

73. P.A. Thrower, Carbon 37 (1999) 1677.

74. X.K. Wang, X.W. Lin, V.P. Dravid, J.B. Ketterson, R.P.H. Chang, Appl. Phys. Lett. 66 (1995) 2430

75. P.J.F. Harris, "Carbon nanotubes and related structure", Cambridge university press (1999).

76. T.W. Ebbesen, H. Hiura, J. Fujita, Y. Ochiai, S. Matsui, K. Tanigaki, Chem. Phys. Lett. 209 (1993) 83.

77. G.H. Taylor, J.D. Fitz Gerald, L. Pang, M.A. Wilson, J. Cryst. Growth 135 (1994) 157.

78. D.T. Colbert, J. Zhang, S.M. McClure, P. Nikolaev, Z. Chen, J.H. Hafner, D.W. Owens, P.G. Kotula, C.B. Cater, J.H. Weaver, A.G. Rinzler, R.E. Smalley, Science 266 (1994) 1218.

79. W.K. Maser, J.M. Lambert, P.M. Ajayan, O. Stephan, P. Bernier, Synthetic Metals 77 (1996) 243.

80. C. Journet, P. Bernier, Appl. Phys. A 67 (1998) 1.

81. H.W. Kroto, J.R. Heath, S.C. O'Brien, R.F. Curl, R.E. Smalley, Nature 318 (1985) 162.

82. T. Guo, P. Nikolaev, A.G. Rinzler, D. Tománek, D.T. Colbert, R.E. Smalley, J. Phys. Chem. 99 (1995) 10694.

83. A. Thess, R. Lee, P. Nikolaev, H. Dai, P. Petit, J. Robert, C. Xu, Y.H. Lee, S.G. Kim, A.G. Rinzler, D.T. Colbert, G.E. Scuseria, D. Tománek, J.E. Fischer, R.E. Smalley, Science 273 (1996) 483.

84. A.G. Rinzler, J. Liu, H. Dai, P. Nikolaev, C.B. Huffman, F.J. Rodriguez-Macias, P.J. Boul, A.H. Lu, D. Heymann, D.T. Colbert, R.S. Lee, J.E. Fischer, A.M. Rao, P.C. Eklund, R.E. Smalley, Appl. Phys. A 67 (1998) 29.

85. B.I. Yakobson, R.E. Smalley, Am. Sci. 85 (1997) 324.

86. P.L. Walker Jr, J.F. Rakszawski, G.R. Imperial, J. Phys. Chem. 63 (1959) 133.

87. M.S. Kim, N. M. Rodriguez, R.T.K. Baker, J. Catal. 131 (1991) 60.

88. M. José-Yacamán, M. Miki-Yoshida, L. Rendón, J.G. Santiesteban, Appl. Phys. Lett. 62 (1993) 657.

89. V. Ivanov, J.B. Nagy, P. Lambin, A. Lucas, X.B. Zhang, X.F. Zhang, D. Bernaerts, G. Van Tendeloo, S. Amelinckx, J. Van Landuyt, Chem. Phys. Lett. 223 (1994) 329.

90. K. Hernadi, A. Fonseca, J.B. Nagy, D. Bernaerts, J. Riga, A. Lucas, Synthetic Metals 77 (1996) 31.

91. A. Fonseca, K. Hernadi, P. Piedigrosso, J.-F. Colomer, K. Mukhopadhyay, R. Doome, S. Lazarescu, L.P. Biro, Ph. Lambin, P.A. Thiry, D. Bernaerts, J.B. Nagy, Appl. Phys. A 67 (1998) 11.

92. P. Nikolaev, M.J. Bronikowski, R.K. Bradley, F. Rohmund, D.T. Colbert, K.A. Smith, R.E. Smalley, Chem. Phys. Lett. 313 (1999) 91.

93. J. Kong, A.M. Cassell, H. Dai, Chem. Phys. Lett. 292 (1998) 567.

94. M. Ge, K. Sattler, Appl. Phys. Lett. 64 (1994) 710.

95. G. Che, B.B. Lakshmi, C.R. Martin, E.R. Fisher, R.S. Rouff, Chem. Mater. 10 (1998) 260

96. S. Seraphin, J. Electrochem. Soc. 142 (1995) 290.

97. W.Z. Li, S.S. Xie, L.X. Qian, B.H. Chang, B.S. Zou, W.Y. Zhou, R.A. Zhao, G. Wang, Science 274 (1996) 1701.

98. Z.W. Pan, S.S. Xie, B.H. Chang, C.Y. Wang, L. Lu, W. Liu, W.Y. Zhou, W.Z. Li, L.X. Qian, Nature 394 (1998) 631.

99. M. Terrones, N. Grobert, J. Olivares, J.P. Zhang, H. Terrones, K. Kordatos, W.K. Hsu, J.P. Hare, P.D. Townsend, K. Prassides, A.K. Cheetham, H.W. Kroto, D.R.M. Walton, Nature 388 (1997) 52.

100. O.M. Küttel, O. Groening, C. Emmenegger, L. Schlapbach, Appl. Phys. Lett. 73 (1998) 2113.

101. Z.F. Ren, Z.P. Huang, J.W. Xu, J.H. Wang, P. Bush, M.P. Siegal, P.N. Provencio, Science 282 (1998) 1105.

102. S. Fan, M.G. Chapline, N.R. Franklin, T.W. Tombler, A.M. Cassell, H. Dai, Science 283 (1999) 512.

103. C.J. Lee, D.W. Kim, T.J. Lee, Y.C. Choi, Y.S. Park, Y.H. Lee, W.B. Choi, N.S. Lee, G.-S. Park, J.M. Kim, Chem. Phys. Lett. 312 (1999) 461.

104. H. Araki, H. Kajii, K. Yoshino, Jpn. J. Appl. Phys. 38 (1999) L1351.

105. H. Kind, J.-M. Bonard, C. Emmenegger, L.-O. Nilsson, K. Hernadi, E. Maillard-Schaller, L. Schlapbach, L. Forró , K. Kern, Adv. Mater. 11 (1999) 1285.

106. Y.C. Choi, D.J. Bae, Y.H. Lee, B.S. Lee, I.T. Han, W.B. Choi, N.S. Lee, J.M. Kim, Synthetic Metals 108 (2000) 159.

107. Y. Chen, D.T. Shaw, L. Guo, Appl. Phys. Lett. 76 (2000) 2469.

108. H. Murakami, M. Hirakawa, C. Tanaka, H. Yamakawa, Appl. Phys. Lett. 76 (2000) 1776.

109. Z. P. Huang, J. W. Xu, Z. F. Ren, J. H. Wang, M. P. Siegal, P. N. Provencio, Appl. Phys. Lett. 73 (1998) 3845.

110. M. Okai, T. Muneyoshi, T. Yaguchi, S. Sasaki, Appl. Phys. Lett. 77 (2000) 3468.

111. C. Bower, W. Zhu, S. Jin, and O. Zhou, Appl. Phys. Lett. 77 (2000) 830.

112. Y.C. Choi, Y.M. Shin, Y.H. Lee, B.S. Lee, G.S. Park, W.B. Choi, N.S. Lee, J.M. Kim, Appl. Phys. Lett. 76 (2000) 2367.

113. A. Gorbunov, O. Jost, W. Pompe and A. Graff, Carbon 40 (2002) 113.

114. R. S. Wagner and W. C. Ellis, Appl. Phys. Lett. 4 (1964) 89.

115. G. G. Tibbetts, J. Cryst. Growth 66 (1984) 632.

116. Y. Saito, T. Yoshikawa, M. Inagaki, M. Tomita and T. Hayashi, Chem. Phys. Lett. 204 (1993) 277.

117. Y. Saito, Carbon 33 (1995) 979.

118. T. J. Trentler, K. M. Hickman, S. C. Goel, A. M. Viano, P. C.Gibbons and W. E. Buhro, Science 270 (1995) 1791.

119. T. J. Trentler, K. M. Hickman, S. C. Goel, A. M. Viano, P. C.Gibbons, W. E. Buhro, M. Y. Chiang and A. M. Beatty, J. Am. Chem. Soc. 119 (1997) 2172.

120. John R. Miller, Patrice Simon The Electrochemical Society Interface, Spring 2008

121. B. E. Conway, in "Electrochemical Supercapacitors: Scientific Fundamentals and Technological Applications," Kluwer Academic/Plenum Publishers, New York, (1999).

122. J. Chmiola, G. Yushin, Y. Gogotsi, C. Portet, P. Simon, and P. L. Taberna, Science 313 (2006) 1760.

123. R. De Levie, Electrochim. Acta 8 (1963) 751.

124. J. R. Miller, Proceedings of the Second International Symposium on EDLC and Similar Energy Storage Sources, S. P. Wolsky and N. Marincic, Editors, Florida Educational Seminars, Boca Raton (1992).

125. J. R. Miller, Proceedings of the 8th International Symposium on EDLC and Similar Energy Storage Sources, S. P. Wolsky and N. Marincic, Editors, Florida Educational Seminars, Boca Raton (1998).

126. P. L. Taberna, P. Simon, and J. F. Fauvarque, J. Electrochem. Soc. 150, A292 (2003).

127. H.E. Becker, U.S. patent 2,800,616 (to General Electric Co.) (1957)

128. Z. Samec, J. Electroanal. Chem. 103 (1979) 1

129. R. Andrews, D. Jacques. D. Qian, E. C. Dickey, Carbon 39 (2001) 1681.

130. P. X. Hou, S. Bai, Q. H. Yang, C. Lin, H. M. Cheng, Carbon 40 (2002) 81.

131. M. Yumura, S. Ohshima, K. Uchida, Y. Tasaka, Y. Kuriki, F. Ikazaki, Y. Saito, S. Uemura, Diamond and Relat. Mater. 8 (1999) 785.

132. Y. Saito, K. Hamaguchi, K. Hata, K. Tohji, A. Kasuya, Y. Nishina, K. Uchida, Y. Tasaka, F. Ikazaki, M. Yumura, Ultramicroscopy 73 (1998) 1.

133. Y. Ando, X. Zhao, H. Kataura, Y. Achiba, K. Kaneto, M. Tsuruta, S. Uemura, S. Iijima, Diamond and Relat. Mater. 9 (2000) 847.

134. Y. S. Park, Y. C. Choi, K. S. Kim, D. C. Chung, D. J. Bae, K. H. An, S. C. Lim, X. Y. Zhu, Y. H. Lee, Carbon 39 (2001) 655.

135. S.C. Tsang, P.J.F. Harris, M.L.H. Green, Nature 362(1993) 520.

136. T. Y .Ebbesen, P. M. Ajaya, F .H .Liou, H. Hiura, K. Tangaki, Nature 367(1997) 519.

137. K. Tohji, H. Takahashi, Y. Shinoda, N. Shimizu, B. Jeyadevan, I. Matsuoka, Y. Saito, A.Kasuya, S. Ito, Y. Nishina, J. Phys. Chem. B 101 (1997) 1974.

138. B. Liu, T. Wagberg, E. Olssen, R. Yang, H. Li, S. Zhang, H. Yang, G. Zou, B. Sundqvist, Chem. Phys. Lett. 321 (2000)365.

139. K.B. Shelimov, R. O. Esenaliev, A. G. Rinzler, C. B. Huffman, R. E. Smalley, Chem. Phys. Lett. 282 (1998) 429.

140. J. M. Moon, K. H. An, Y. H. Lee, Y. S. Park, D. J. Bae, G. S. Park, J. Phys. Chem. B105 (2001) 5677.

141. M. Zhang, M. Yudasaka, A. Koshio, S. Iijima, Chem. Phys, Lett. 349 (2001) 25.

142. D. Chattopadhyay, I. Galeska, F. Papadimitrakopoulos, Carbon 40 (2002) 985.

143. X. H. Chen, C. S. Chen, Q. Chen, F. Q. Cheng, G. Zhang, Z. Z. Chen, Materials Lett. 57 (2002) 734.

144. H. Kajiura, S. Tsutsui, H. Huang, Y. Murakami, Chem. Phys, Lett. 364 (2002) 586.

145. S. Bandow, A. M. Rao, K. A. Williams, A. Thess, R. E. Smalley, P. C. Eklund, J. Phys. Chem. B 101 (1997) 8839.

146. Y. Ando, X. Zhao, S. Inoue, S. Iijima, Journal of Crystal Growth 237-239 (2002) 1926.

147. I. W. Chiang, B. E. Brinson, A. Y. Huang, P. A. Willis, M. J. Bronikowski, J. L. Margrave, R. E. Smalley, R. H. Hauge, J. Phys. Chem. B 105 (2001) 8297.

148. D.I. Boos, U.S. Patent 3 536 963 (to Standard Oil, SOHIO) (1970).

149. T.C. Murphy, R.B. Wright, R.A. Sutula, in: F.M. Delnick, D. Ingersoll, X. Andrieu, K. Naoi (Eds.), Electrochemical Capacitors II, Proceedings, vols. 96–25, The Electrochemical Society, Pennington, NJ, (1997) 258.

150. S. Sarangapani, B.V. Tilak, C.P. Chen, J. Electrochem. Soc. 143 (1996) 3791.

151. M. Sullivan, R. Ko¨ tz, O. Haas, in: F.M. Delnick, M. Tomkiewicz (Eds.), Electrochemical Capacitors, Proceedings, vols. 95–29, The Electrochemical Society, Pennington, NJ, 1996, 198–209.

152. M.G. Sullivan, M. Ba¨rtsch, R. Ko¨ tz, O. Haas, in: F.M. Delnick, D. Ingersoll, X. Andrieu, K. Naoi (Eds.), Electrochemical Capacitors II, Proceedings Volume, vols. 96–25, The Electrochemical Society, Pennington, NJ, 1997, pp. 192–201.

153. M. Nakamura, M. Nakanishi, K. Yamamoto, J. Power Sources 60 (1996) 225.

154. A.G. Pandolfo, A.M. Vasallo, G.L. Paul, Proceedings of The 7th International Seminar on Double Layer Capacitors and Similar Energy Storage Devices, Florida Educational Seminar, December 1997.

155. S. Ardizzone, G. Fregonara, S. Trasatti, Electrochim. Acta 35 (1990) 263.

156. R. Ko¨ tz, S. Stucki, Electrochim. Acta 31 (1986) 1311.

157. J.P. Zheng, P.J. Cygan, T.R. Jow, J. Electrochem. Soc. 142 (1995) 2699.

158. S. Trasatti, P. Kurzweil, Platinum Met. Rev. 38 (1994) 46.

159. T.J. Guther, R. Oesten, J. Garche, in: F.M. Delnick, D. Ingersoll, X. Andrieu, K. Naoi (Eds.), Electrochemical Capacitors II, Proceedings, vols. 96–25, The Electrochemical Society, Pennington, NJ, 1997, p. 16.

160. T.C. Liu, W.G. Pell, B.E. Conway, S.L. Roberson, J. Electrochem. Soc. 145 (1998) 1882.

161. X. Ren, S. Gottesfeld, J.P. Ferraris, in: F.M. Delnick, M. Tomkiewicz (Eds.), Electrochemical Capacitors, Proceedings, vols. 95–29, The Electrochemical Society, Pennington, NJ, 1996, p. 138.

162. C. Arbizzani, M. Mastragostino, L. Meneghello, Electrochim. Acta 41 (1996) 21.

163. K. Naoi, Extended Abstracts, 49th Annual Meeting of the International Society of Electrochemistry, Kitakyushu, Japan, September, pp. 647, 1998.

164. A. Yoshida, K. Nishida, S. Nonaka, S. Nomoto, M. Ikeda, S. Ikuta, Japanese Patent 9-266143, (to Matsushita Electric), 1997.

165. M. Ue, K. Ida, S. Mori, J. Electrochem. Soc. 141 (1994) 2989.

166. Y. Kibi, T. Saito, M. Kurata, J. Tabuchi, A. Ochi, J. Power Sources 60 (1996) 219.

167. R. Ko¨ tz, M. Ba¨rtsch, A. Braun, O. Haas, Proceedings of The 7th International Seminar on Double Layer Capacitors and Similar Energy Storage Devices, Florida Educational Seminar, December 1997.

168. J.P. Zheng, T.R. Jow, J. Electrochem. Soc. 144 (1997) 2417.

169. B.E. Conway, W.G. Pell, Proceedings of the 8th International Seminar on Double Layer Capacitors and Similar Energy Storage Devices, Florida Educational Seminar, December, 1998.

170. R. De Levie, in: P. Delahay (ed.), Advances in Electrochemistry and Electrochemical Engineering, vol. 6, 1967, pp. 329, Interscience Publishers, New York.

171. R.E. DeLaRue, C.W. Tobias, J. Electrochem. Soc. 106 (1959) 827.

172. T. Hertel, R. E. Walkup, P. Avouris, Phys. Rev. B 58 (1998) 13870

173. B. Chapman, Glow Discharge Process, Wiley, New York, 1980

174. C.C. Chen, C.F. Chen, I.H. Lee, C. L. Lin, Diamond and related materials 14 (2005) 1897

175. S. Trasobares, C. P. Ewels, J. Birrell, O. Stephan, B. Q. Wei, J. A. Carlisle, D. Miller, P. Keblinski, P. M. Ajayan, Adv. Mater. 16 (2004) 610

176. N.G. Shang, C.P. Li, W.K. Wong, C.S. Lee, I. Bello, S.T. Lee, Appl. Phys. Lett. 81 (2002) 5024

177. S. Trasobares, C. P. Ewels, J. Birrell, O. Stephan, B. Q. Wei, J. A. Carlisle, D. Miller, P. Keblinski, and P. M. Ajayan, Adv. Mater. 16 (2004) 610

178. S. B. Sinnott, R. Andrews, D. Quian, A. M. Rao, Z. Mao, E. C. Dickey, F. Derbyshire, Chem. Phys. Lett. 315 (1999) 25

179. N. M. Rodriguez, A. Chambers, R. T. K. Baker, Langmuir 11 (1995) 3862

180. M. Yudasaka, R. Kikuchi, Y. Ohki, E. Ota, S. Yoshimura, Appl. Phys. Lett. 70 (1997) 1817

181. S. K. Srivastava, A. K. Shukla, V. D. Vankar, V. Kumar, Thin Solid Films 492 (2005) 124

182. M. Chen, C. M. Chen, L. K. Wu, J. Mater. Sci. 37 (2002) 3561

183. Chatei, M. Belmahi, M. B. Assouar, L. Le Brizoual, P. Bourson, J. Bougdira, Diamond Relat. Mater. 15 (2006) 1041

184. T. Kawai, Y. Miyamoto, O. Sugino, Y. Koga, Phys. Rev. B 66 (2002) 033404

185. F. Tuinstra and J. L. Koenig, J. Chem. Phys. 53 (1970) 1126

186. R. J. Nemanich and S. A. Solin, Phys. Rev. B 20 (1979) 392

187. R. Al-Jishi and G. Dresselhaus, Phys. Rev. B 26 (1982) 4514

188. P. Lespade, R. Al-Jishi, and M. S. Dresselhaus, Carbon 20 (1982) 427

189. R. Vidano and D. B. Fischbach, J. Am. Ceram. Soc. 61 (1978) 13

190. A. Cuesta, P. Dhamelincourt, J. Laureyns, A. Martinez-Alonso, and J. M. D. Tascon, Carbon 32 (1994) 1523

191. G.H. Chen, W.G. Weng, D.J. Wu, C.L. Wu, J.R. Lu, P.P. Wang, X.F. Chen, Carbon 42 (2004) 753

192. C.R. Lin, C.H. Su, C.Y. Chang, C.H. Hung, Y.F. Huang, Surf. Coat. Technol. 200 (2006) 3190

193. A.C. Ferrari, J. Robertson, Phys. Rev. B 61 (2000) 14095

194. Z. L. Wang, Z.C. Kang, Carbon 35 (1997) 419

195. Alfred T.H. Chuang, J. Robertson, Bojan O. Boskovic. Krzysztof K.K. Koziol, Appl. Phys. Lett. 90 (2007) 123107

196. E. Auer, A. Freund, J. Pietsch, T. Tacke, Applied Catalysis A: General 173 (1998) 259

197. K. Babel, K. Jurewicz, Journal of Physics and Chemistry of Solids 65 (2004) 275

198. C.M. Yang, Y.J. Kim, M. Endo, H. Kanoh, M. Yudasaka, S. Iijima, K. Kaneko, J. AM. Chem. Soc. 129 (2007) 20

199. M.A. Ellott, P.W. May, J. Petherbridge, S.M. Leeds, M.N.R Ashfold, W.N. Wang, Diamond Relat. Mater. 9 (2000) 311

200. E. Frackowiak, S. Delpeux, K. Jurewicz, K. Szostak, D. Cazorla-Amoro, F. Beguin, Chem. Phys. Lett. 361 (2002) 35

201. C.S. Li, D.Z. Wang, T.X. Liang, X.F. Wang, J. Liang, Mater. Lett. 58 (2004) 3774

202. C. Li, D. Wang, T. Liang, X. Wang, J. Wu, X. Hu, J. Liang, Powder Technol. 142 (2004) 175

203. M. Hughes, M.S.P. Shaffer, A.C. Renouf, C. Singh, G.Z. Chen, D.J. Fray, A.H. Windle, Adv. Mater. 14 (2002) 382

204. M. Hughes, G.Z. Chen, M.S.P. Shaffer, D.J. Fray, A.H. Windle, Chem. Mater. 14 (2002) 1610

205. Y.K. Zhou, B.L. He, W.J. Zhou, J. Huang, X.H. Li, B. Wu, H.L. Li, Electrochim. Acta 49 (2004) 257

206. Y.K. Zhou, B.L. He, F.B. Zhang, H.L. Li, J. Solid State Electrochem. 8 (2004) 482

207. X. Qin, S. Durbach, G.T. Wu, Carbon 42 (2004) 451

208. J.H. Park, J.M. Ko, O.O. Park, J. Electrochem. Soc. 150 (2003) A864

209. J.S. Ye, X. Liu, H.F. Cui, W.-D. Zhang, F.-S. Sheu, T.M. Lim, Electrochem. Commun. 7 (2005) 249

210. K.C. Park, T. Hayashi, H. Tomiyasu, M. Enbo, M.S. Dresselhaus, J. Mater. Chem. 15 (2005) 407

211. T.I.T. Okpalugo, P.Papakonstantinou, H.Murphy, J.McLaughlin, N.M.D. Brown and T.McNally, Fullerenes, Nanotubes, and Carbon Nanostructures 13 (2005) 477

212. T. Teranishi, M. Hosoe, T. Tanaka, and M.Miyake, J. Phys. Chem. B 103 (1999) 3818

213. C.M. Chen, M. Chen, F.C. Leu, S.Y. Hsu, S.C. Wang, S.C. Shi, C.F. Chen, Diamond and Related Materials 13 (2004) 1182

214. S. M. Lipka, IEEE AES Systems Magazine, July 1997

215. T. Momma, X. Liu, T. Osaka, Y. Ushio, and Y. Sawada, J. Power Source 60, 249 (1996)

216. Z. Wu, Charles U. Pittman, Carbon 33 (1995) 597

217. M. Endo, T. Maeda, T. Takeda, Y.J. Kim, K. Koshiba, H. Hara, M.S. Dresselhaus, J. Electrochem. Soc. 148 (2001) A910

218. A´ lvarez S., Blanco-Lo´pez M.C., Miranda-Ordieres A.J., Fuertes A.B. and Centeno T.A., Carbon 43 (2005) 866

219. Keiser H., Beccu K.D. and Gutjahr M.A., Electrochim. Acta 12 (1976) 539

220. B.E. Conway, Electrochim. Acta, 138 (1991) 1539